Delft University of Technology

Spheres vs. rods in fluidized beds
Numerical and experimental investigations

Mema, I.

DOI
10.4233/uuid:229ada6c-6316-4971-814b-8ed0c91c715e

Publication date
2020

Document Version
Final published version

Citation (APA)
Mema, I. (2020). *Spheres vs. rods in fluidized beds: Numerical and experimental investigations*. [Dissertation (TU Delft), Delft University of Technology]. https://doi.org/10.4233/uuid:229ada6c-6316-4971-814b-8ed0c91c715e

Important note
To cite this publication, please use the final published version (if applicable).
Please check the document version above.

Copyright
Other than for strictly personal use, it is not permitted to download, forward or distribute the text or part of it, without the consent of the author(s) and/or copyright holder(s), unless the work is under an open content license such as Creative Commons.

Takedown policy
Please contact us and provide details if you believe this document breaches copyrights.
We will remove access to the work immediately and investigate your claim.

This work is downloaded from Delft University of Technology.
For technical reasons the number of authors shown on this cover page is limited to a maximum of 10.

SPHERES VS. RODS IN FLUIDIZED BEDS

NUMERICAL AND EXPERIMENTAL INVESTIGATIONS

SPHERES VS. RODS IN FLUIDIZED BEDS

NUMERICAL AND EXPERIMENTAL INVESTIGATIONS

Proefschrift

ter verkrijging van de graad van doctor
aan de Technische Universiteit Delft,
op gezag van de Rector Magnificus prof. ir. T.H.J.J. van der Hagen,
voorzitter van het College voor Promoties,
in het openbaar te verdedigen op
Donderdag 3 December 2020 om 10:00 uur

door

Ivan MEMA

Master of Chemical Engineering,
Faculty of Technology and Metallurgy, University of Belgrade, Serbia,
geboren te Vršac, Serbia.

Dit proefschrift is goedgekeurd door de

promotor: prof. dr. ir. J. T. Padding
2^e promotor: prof. dr. ir. W. de Jong

Samenstelling promotiecommissie:

Rector Magnificus,	voorzitter
Prof. dr. ir. J. T. Padding,	Delft University of Technology
Prof. dr. ir. W. de Jong,	Delft University of Technology
Onafhankelijke leden:	
Prof. dr. S. Pirker,	Johannes Kepler University Linz
Prof. dr. ir. N.G. Deen,	Eindhoven University of Technology
Prof. dr. A.R. Thornton,	University of Twente
Prof. dr. ir. C. Poelma	Delft University of Technology

Keywords: Fluidized bed, Non-spherical particles, CFD-DEM, MPT, XRT, Hydrodynamic forces

Printed by:

Front & Back:

Copyright © 2020 by I. Mema

ISBN 000-00-0000-000-0

An electronic version of this dissertation is available at
http://repository.tudelft.nl/.

SUMMARY

For the past century, fluidized beds have been standard equipment in many branches of industry. In most applications they are used to manipulate granular and powder-like materials, whose particles can roughly be approximated as spheres. Therefore, numerical models and investigations have focused mainly on fluidized beds with spherical particles. Recent decades witnessed an increase in the use of fluidized beds in biomass processing. Unlike other materials typically used in fluidized beds, biomass is characterized by relatively large and elongated particles. For the sake of simplicity, numerical models for simulating fluidization of elongated particles have so far neglected a lot of specifics that can occur during this process and even applied the same models and conclusions that were developed for fluidization of spherical particles.

The goal of this thesis is to define what is necessary for performing physically correct Computational Fluid Dynamics - Discrete Element Model (CFD-DEM) simulations of elongated particles fluidization. This thesis emphasizes the difference in fluidization between spherical and elongated particles and looks into ways to include specific particle and fluid interactions related to elongated particles into numerical (CFD-DEM) model. Results from CFD-DEM simulations were validated using two experimental techniques, magnetic particle tracking (MPT) and X-ray tomography (XRT). This thesis is part of larger project of multi-scale modeling of fluidized beds with elongated particles and is focusing on the middle scale, bridging fully resolved, direct numerical simulations (DNS) with large scale, two fluid model (TFM) or multi-phase - particle in cell (MP-PIC) models, capable of simulating industrial sized fluidized beds.

This thesis first looks in to the effect of including shape induced lift force and hydrodynamic torque, which were so far neglected in CFD-DEM simulations of elongated particles. It is shown that including lift force and hydrodynamic torque leads to considerable changes in the particle vertical velocity and particle preferred orientation in the fluidized bed. Looking into the mixing characteristics, as one of the most important parameters of fluidized beds, also considerable differences were found. Further differences in fluidization behaviour of spherical and elongated particles, as well as the effect of increasing particle aspect ratio, were shown experimentally, using MPT. Clear differences between spherical and elongated particles were found concerning the particle velocity and rotational velocity distributions. The effect of increasing particle aspect ratio and gas inlet velocity on fluidization of elongated particles was shown. Using XRT, the difference in bubbling and slugging fluidization between spherical and elongated particles was shown. In the end, the effect of newly developed multi-particle correlations for hydrodynamic forces and torque was tested, and it is concluded that they can improve the accuracy of simulations of dense fluidized beds containing elongated particles.

The findings of this thesis clearly show that the models and assumptions developed for fluidization of spherical particles cannot simply be transferred to the fluidization of elongated particles. The results presented here give a new insight in the fluidization of elongated particles. They are also valuable for validation and development of larger scale models capable of simulating industrial size fluidized bed with elongated particles.

SAMENVATTING

In de laatste honderd jaar zijn gefluïdiseerde bedden (wervelbedden) de standaard apparatuur in veel taken van industrie. In de meeste toepassingen worden ze gebruikt om granulaire en poederachtige materialen te bewerken, waar de deeltjes als min of meer rond benaderd mogen worden. Numerieke modellen en onderzoeken hebben zich daarom vooral gericht op gefluïdiseerde bedden met ronde deeltjes. In de laatste tientallen jaren worden gefluïdiseerde bedden steeds meer toegepast in het verwerken van biomassa. In tegenstelling tot andere materialen die typisch in gefluïdiseerde bedden worden verwerkt, wordt biomassa gekarakteriseerd door relatief grote en uitgerekte deeltjes. Voor de eenvoud hebben numerieke modellen voor de simulatie van fluïdisatie van uitgerekte deeltjes tot nu toe veel specifieke interacties genegeerd die kunnen optreden in dit proces, en zelfs dezelfde modellen en conclusies gebruikt als die waren ontwikkeld voor fluïdisatie van ronde deeltjes.

Het doel van dit proefschrift is te definiëren wat nodig is om fysisch correcte Computational Fluid Dynamics - Discrete Element Model (CFD-DEM) uit te voeren voor de fluïdisatie van uitgerekte deeltjes. Dit proefschrift legt de nadruk op het verschil in fluïdisatie tussen bolvormige en uitgerekte deeltjes, en bekijkt manieren om specifieke interacties in te bouwen tussen de deeltjes en het gas, gerelateerd aan hun uitgerekte vorm, in numerieke (CFD-DEM) modellen. Resultaten van CFD-DEM simulaties zijn gevalideerd met behulp van twee experimentele technieken, magnetic particle tracking (MPT) en X-ray tomography (XRT). Dit proefschrift is onderdeel van een groter project op het gebied van multi-scale modeling van gefluïdiseerde bedden met uitgerekte deeltjes en richt zich op de middelste schaal, welke een brug bouwt tussen direct numerical simulations (DNS) en grote schaal two fluid model (TFM) of multi-phase-particle in cell (MP-PIC) modellen, die in staat zijn industriële schaal gefluïdiseerde bedden te simuleren.

Dit proefschrift bekijkt eerst het effect van het meenemen van vorm-gerelateerde lift krachten en hydrodynamisch draaimoment, welke tot nu toe genegeerd zijn in CFD-DEM simulaties van uitgerekte deeltjes. Er wordt aangetoond dat het meenemen van lift en draaimoment tot behoorlijke veranderingen leidt in de deeltjes verticale snelheid en de voornaamste oriëntatie van de deeltjes in het gefluïdiseerde bed. Als we naar het menggedrag kijken, als een van de voornaamste parameters van gefluïdiseerde bedden, zien we ook behoorlijke verschillen. Nog meer verschillen in fluïdisatiegedrag tussen bolvormige en uitgerekte deeltjes, alsook het effect van aspect ratio, zijn aangetoond middels MPT experimenten. Duidelijke verschillen tussen bollen en uitgerekte deeltjes zijn gevonden voor de deeltjes snelheid en rotatiesnelheid distributies. Het effect van toenemende deeltjes aspect ratio en gas inlaat snelheid op de fluïdisatie van uitgerekte deeltjes is aangetoond. Met behulp van XRT is het verschil tussen bubbelend en slakvormende fluïdisatie aangetoond. Tegen het eind is het effect van een nieuw ontwikkelde meer-deeltjes correlatie voor hydrodynamische krachten en draaimomenten uitgetest, en is geconcludeerd dat deze de nauwkeurigheid van simulaties van dichte

gefluïdiseerde bedden met uitgerekte deeltjes kan verhogen.

De resultaten van dit proefschrift laten duidelijk zien dat de modellen en aannames ontwikkeld voor fluïdisatie van ronde deeltjes niet simpelweg overgebracht kunnen worden naar fluïdisatie van uitgerekte deeltjes. De resultaten geven nieuw inzicht in de fluïdisatie van uitgerekte deeltjes. Ze zijn ook waardevol voor validatie en ontwikkeling van grotere schaal modellen die industriële schaal gefluïdiseerde bedden kunnen simuleren met uitgerekte deeltjes.

CONTENTS

Summary v

Samenvatting vii

List of Figures xiii

List of Tables xix

1 Introduction 1
- 1.1 Fluidization 2
- 1.2 Specifics of elongated particles 3
- 1.3 Scope of thesis 4
- 1.4 Outline of thesis 4

2 Effect of lift force and hydrodynamic torque 7
- 2.1 Introduction 8
- 2.2 Numerical approach 9
  - 2.2.1 Discrete Element Method (DEM) 9
  - 2.2.2 Computational Fluid Dynamics (CFD) 12
- 2.3 Simulation Parameters and Void Fraction Calculation 17
- 2.4 Results 18
  - 2.4.1 Particle dynamics 18
  - 2.4.2 Particle velocity along z-axis 19
  - 2.4.3 Particle Orientation 22
  - 2.4.4 Angular Momentum 25
- 2.5 Discussion and Conclusion 29

3 Spherical versus elongated particles - magnetic particle tracking 35
- 3.1 Introduction 36
- 3.2 Magnetic Particle Tracking (MPT) 37
- 3.3 Experimental setup 37
- 3.4 Results 39
  - 3.4.1 Minimum fluidization velocity 41
  - 3.4.2 Particle velocity 41
  - 3.4.3 Particle rotational velocity 46
  - 3.4.4 Particle orientation 46
- 3.5 Discussion and conclusion 52

4 Spherical versus elongated particles - X-ray tomography 55
4.1 Introduction . . . 56
4.2 Experimental setup and methods . . . 57
4.2.1 Fluidized bed and particles . . . 57
4.2.2 Calibration and phantom reconstruction . . . 58
4.3 Results . . . 59
4.3.1 Average bubble diameter. . . . 60
4.3.2 Bubble rise velocity . . . 62
4.3.3 Waiting time distribution . . . 62
4.3.4 Slug Frequency. . . . 65
4.4 Discussion . . . 66
4.5 Conclusion . . . 69

5 Multi-particle correlations in CFD-DEM of fluidized elongated particles 71
5.1 Introduction . . . 72
5.2 Numerical model . . . 73
5.3 Simulation Parameters . . . 77
5.4 Results . . . 77
5.4.1 Particle orientation . . . 79
5.4.2 Effect of lift force and hydrodynamic torque on particle orientation . . . 83
5.4.3 Particle velocity along z-axis . . . 85
5.5 Conclusion . . . 86

6 Spherical versus elongated particles - mixing in a gas fluidized bed 89
6.1 Introduction . . . 90
6.2 Numerical model . . . 91
6.2.1 Hydrodynamic forces . . . 91
6.3 Simulation Parameters . . . 95
6.4 Mixing entropy . . . 97
6.5 Results . . . 98
6.5.1 Particle mixing . . . 98
6.5.2 Effect of hydrodynamic lift force and torque on mixing characteristics of elongated particles . . . 104
6.6 Conclusion . . . 104

7 Conclusion 107
7.1 Recommendations for future work . . . 109

A Lift and Torque Coefficients 111

B Slugging of spherical particles - audio signal analysis 115
B.1 Audio signal analysis . . . 115
B.1.1 Introduction and method explanation . . . 115
B.1.2 Results . . . 116
B.1.3 Conclusion. . . . 117
References . . . 118

Acknowledgements **129**
Curriculum Vitæ **131**
List of Publications **133**

List of Figures

1.1 Typical example of biomass materials, form wood chips, wood pellets to straw-like material. 2

1.2 Typical example of particle collisions for (a) spherical and (b) spherocylindrical particles. 3

2.1 A schematic of a sample contact between two spherocylinders with each having a shaft length L and characteristic radius R. The inset image shows details of the normal and tangential unit vectors at the contact. 11

2.2 Lift vector orientation based on the relative velocity of the fluid with respect to the particle $\mathbf{v}'_{fi} = \mathbf{v}_f - \mathbf{v}_i$ and particle orientation vector $\mathbf{u}_i$. The angle of incidence of the fluid flow α is also indicated on the figure. 15

2.3 A spherocylinder subject to torque. The difference between the centre of pressure $\mathbf{x}_{cp}$ and the centre of mass $\mathbf{x}_{cm}$ leads to the development of a hydrodynamic torque $\mathbf{T}_{i,f}$. $\Delta\mathbf{x}$ is the distance between $\mathbf{x}_{cp}$ and $\mathbf{x}_{cm}$. 16

2.4 Visualisation of a typical fluidisation cycle lasting approximately 1.2 seconds. (a) Drag only. (b) $\mathrm{All}_{\mathrm{Sanj}}$. Five characteristic snapshots are shown and labelled as follows: (1) Start of bed expansion; (2) Mid-way of bed expansion; (3) Maximum bed expansion; (4) Start of release; (5) End of release. These system snapshots were visualised using OVITO [1]). 20

2.5 Variation in the particle occupancy $\langle n_p \rangle$ with reactor height. The red dashed lines indicate the positions along the z-axis used for the calculation of v_z profiles in section 2.4.2. 21

2.6 (a) Snapshot of the fluidized bed reactor with fluid velocity $1.7U_{mf}$ where the particles hydrodynamic force case is “Drag only”. (b) Analysis positions in the bed reactor along the z-direction. These system snapshots were visualised using OVITO [1]). 21

2.7 Comparison of the temporally-averaged v_z along the x-axis for the positions defined in Figure 2.6(b) in a fluidized bed reactor for different hydrodynamic conditions: Drag only, lift force described by Zastawny (L_{Zast}), lift force described by Sanjeevi (L_{Sanj}), HD Torque described by Zastawny (T_{Zast}) and by Sanjeevi (T_{Sanj}). In these plots x is the position normalised by the length of reactor along the x-axis (0.15 m). Cases with lift force are presented red dashed lines (- - - -), cases with torque with the green dotted line (.....) and cases with all forces included with the blue dash-dot lines. (-·-·-). The filled triangles represents cases of Zastawny *et al.* [2] and the filled circles are cases using the correlations of Sanjeevi *et al.* [3]. 23

2.8 Preferred particle orientation. Variation of $f_p(u_z)$ for differing hydrodynamic force conditions. 24

2.9 Preferred orientation of particles in the grid cells of the reactor for different cases of hydrodynamic force, with drag only and cases with lift force. (a) Drag only. (b) L_{Zast}. (c) L_{Sanj}. Here the colour scheme is: blue squares (🟦) are x-aligned, green squares (🟩) are y-aligned, red squares (🟥) are z-aligned and cyan squares (🟦) are randomly orientated. White space represents empty cells. The dimensions of the reactors on the xz-plane are $L_x \times H_z = 0.15\,\mathrm{m} \times 0.99\,\mathrm{m}$. In this plot, the dimensions are normalised by the grid cell size thus leading to $n_x^g = L_x/c_x = 10$ and $n_z^g = H_z/c_z = 66$. . . 26

2.10 Preferred orientation of particles in the grid cells of the reactor for different cases of hydrodynamic force, with drag only and cases with hydrodynamic torque. (a) Drag only. (b) T_{Zast}. (c) T_{Sanj}. Details of the colour scheme are provided in the caption of Fig. 2.9. 27

2.11 Preferred orientation of particles in the grid cells of the reactor for different cases of hydrodynamic force, with drag only and cases with all forces included. (a) Drag only. (b) All_{Zast}. (c) All_{Sanj}. Details of the colour scheme are provided in the caption of Fig. 2.9. 28

2.12 Angular momentum in x-z plane, temporally-averaged and averaged through y-direction for cases with (a) drag only and (b, c) drag and lift 29

2.13 Angular momentum in x-z plane, temporally-averaged and averaged through y-direction for cases with (a) drag only and (b, c) drag and torque. 30

2.14 Angular momentum in x-z plane, temporally-averaged and averaged through y-direction for cases with (a) drag only and (b, c) all hydrodynamic forces included. 31

3.1 (a) Full experimental setup, (b) close-up of the column with sensor array. 1-Fluidized bed, 2-Sensor array, 3-Helmholtz coil, 4-Humidifier. 38

3.2 3D printed alumide particles of aspect ratio AR-1, AR-4 and AR-6. 39

3.3 Pressure drop measurements and minimum fluidization velocity determination for AR-1, AR-4 and AR-6 particles. The dashed red line represents the determined minimum fluidization velocity, the dotted lines indicates the used fluidization velocities: green $1.4\mathrm{U_{mf}}$, purple $1.6\mathrm{U_{mf}}$, blue $1.8\mathrm{U_{mf}}$ and cyan $2\mathrm{U_{mf}}$. 42

3.4 Velocity distributions for AR-1 particles in the X-Z plane for different gas inlet velocities. Positions are indicated in cm. Red and purple arrows indicate the directions of the main vortices. 43

3.5 Velocity distributions for the AR-4 particles in X-Z plane for different gas inlet velocities. Positions are indicated in cm. Red and purple arrows indicate the directions of the main vortices. 44

3.6 Velocity distributions for AR-6 particles in the X-Z plane for different gas inlet velocities. Positions are indicated in cm. Red and purple arrows indicate the directions of the main vortices. 45

3.7 Rotational velocity [rot/s] distributions, for rotations around axes perpendicular to the long axis of the particle, in the x-z plane for AR-4 particles. 47

3.8 Rotational velocity [rot/s] distributions, for rotations around axes perpendicular to the long axis of the particle, in the x-z plane for AR-6 particles. 47
3.9 Rotational velocity [rot/s] distributions in the x-z plane for AR-1 particles. 48
3.10 Effect of gas velocity on the time-averaged fraction (f_p) of particle orientation in the z-direction (u_z) of AR-4 and AR-6 particles. 49
3.11 Comparison of time-averaged particle orientation in the z-direction for AR-4 and AR-6 particles. 49
3.12 Distribution of the predominant orientation of AR-4 particles in the x-z plane. Here the colour scheme is: blue squares (🟦) are x-aligned, green squares (🟩) are y-aligned, red squares (🟥) are z-aligned, and cyan squares (🟦) are randomly oriented. White space represents empty cells. Schematic representation of color scheme is shown in Figure 3.13 51
3.13 AR-6 particle prefered orientation in x-z plane. Here the colour scheme is: blue squares (🟦) are x-aligned, green squares (🟩) are y-aligned, red squares (🟥) are z-aligned and cyan squares (🟦) are randomly orientated. White space represents empty cells. 52

4.1 (a) View of the fluidized bed column between the source and the detector plate, 1-X-ray source tube, 2-Detector plate, 3-Fluidized bed column. (b) Schematic of X-ray setup (top view). 58
4.2 Reconstructions of different combinations of phantoms in beds of AR-1 and AR-4 particles. 59
4.3 Bubble visualizations for at bed height of 240mm and $\mathrm{U}-\mathrm{U}_{\mathrm{mf}} = 0.65\,\mathrm{m/s}$ for (a) AR-1 and (b) AR-4 particles. 60
4.4 Average bubble diameter for AR-1 and AR-4 particles on different excess gas velocities. Error bars indicate standard deviation of bubble diameters. The dots indicate indicate the average bubble size predicted by Aug et al. [4] for spherical (AR-1) particles in a high aspect ratio bed. 61
4.5 Average number of bubbles present in the horizontal cross-sections at low (*) and high (x) positions in the bed, for AR-1 (- - -) and AR-4 (—) particles, as a function of excess gas velocity. 62
4.6 Bubble size distribution for AR-1 and AR-4 particles on different excess gas velocities and low and high positions in the bed. 63
4.7 Bubble velocities for AR-1 and AR-4 particles on different gas excess velocities as a function of bed height. 63
4.8 Signal intensity before and after applying threshold for (a) AR-1 and (b) AR-4 particles at $\mathrm{h}_{\mathrm{hig}}$ and $\mathrm{U}-\mathrm{U}_{\mathrm{mf}} = 0.65\,\mathrm{m/s}$ 64
4.9 Waiting time distribution for AR-1 particles at the higher bed height $\mathrm{h}_{\mathrm{hig}}$ and excess gas velocities $\mathrm{U}-\mathrm{U}_{\mathrm{mf}}$ of: (a) 0.4, (b) 0.65, (c) 0.9, (d) 1.15 and (e) 1.4 m/s. 65
4.10 Waiting time distribution for AR-4 particles at the higher bed height $\mathrm{h}_{\mathrm{hig}}$ and excess gas velocities $\mathrm{U}-\mathrm{U}_{\mathrm{mf}}$ of: (a) 0.65, (b) 0.9 and (c) 1.15 m/s. . . . 66

4.11 Power spectra for appearance of slug for the AR-1 particles at the higher bed height h_{hig} and excess gas velocities $\mathrm{U}-\mathrm{U}_{\mathrm{mf}}$ of: (a) 0.4, (b) 0.65, (c) 0.9, (d) 1.15 and (e) 1.4 m/s. 67
4.12 Power spectra for the AR-4 particles at the higher bed height h_{hig} and excess gas velocities $\mathrm{U}-\mathrm{U}_{\mathrm{mf}}$ of: (a) 0.65, (b) 0.9 and (c) 1.15 m/s. 67

5.1 Probability distribution function for the particle orientation at (a) $1.6\mathrm{U}_{\mathrm{mf}}$ and (b) $2\mathrm{U}_{\mathrm{mf}}$. Simulations with single (SP) and multi (MP) particle correlations are compared with MPT experiments. 80
5.2 Preferred orientation of particles in the grid cells of the reactor for (a) single-particle (b) multi-particle correlations and (c) experimental results at $1.6\mathrm{U}_{\mathrm{mf}}$. Here the colour scheme is: blue squares (🟦) are x-aligned, green squares (🟩) are y-aligned, red squares (🟥) are z-aligned and cyan squares (🟦) are randomly orientated. White space represents empty cells. 81
5.3 Preferred orientation of particles in the grid cells of the reactor for (a) single-particle (b) multi-particle correlations and (c) experimental results at $2\mathrm{U}_{\mathrm{mf}}$. Here the colour scheme is: blue squares (🟦) are x-aligned, green squares (🟩) are y-aligned, red squares (🟥) are z-aligned and cyan squares (🟦) are randomly orientated. White space represents empty cells. 82
5.4 Average cell occupancy along the height in z-direction. The dashed red lines indicate the positions along the z-axis used for the sampling of v_z profiles in section 5.4.3. 83
5.5 Preferred particle orientation at (a) $1.6\mathrm{U}_{\mathrm{mf}}$ and (b) $2\mathrm{U}_{\mathrm{mf}}$. Variation of $f_p(|u_z|)$ for simulations with differing hydrodynamic force conditions and from experimental results. 84
5.6 Preferred orientation of particles in the grid cells of the reactor for case with (a) drag force only (b) drag and lift force (c) drag and lift force and hydrodynamic torque, and (d) MPT experiments, at $1.6\mathrm{U}_{\mathrm{mf}}$. Here the colour scheme is: blue squares (🟦) are x-aligned, green squares (🟩) are y-aligned, red squares (🟥) are z-aligned and cyan squares (🟦) are randomly orientated. White space represents empty cells. 85
5.7 Preferred orientation of particles in the grid cells of the reactor for case with (a) drag force only (b) drag and lift force (c) drag and lift force and hydrodynamic torque, and (d) MPT experiments, at $2\mathrm{U}_{\mathrm{mf}}$. Here the colour scheme is: blue squares (🟦) are x-aligned, green squares (🟩) are y-aligned, red squares (🟥) are z-aligned and cyan squares (🟦) are randomly orientated. White space represents empty cells. 86
5.8 Comparison of the temporally-averaged vertical solids velocity v_z along the x-axis at two bed heights and at (a) $1.6\mathrm{U}_{\mathrm{mf}}$ and (b) $2\mathrm{U}_{\mathrm{mf}}$. 87

6.1 Initial beds for (a) AR-1 and (b) AR-4 particles. 96
6.2 Mixing entropy as function of time for (a) AR-1 and (b) AR-4 particles. . . 99
6.3 Comparison of mixing entropy as function of time for AR-1 and AR-1 particles at $1.6\mathrm{U}_{\mathrm{mf}}$, $1.7\mathrm{U}_{\mathrm{mf}}$ and $2.9\mathrm{U}_{\mathrm{mf}}$. 100
6.4 Mixing time as function of inlet gas velocity for AR-1 and AR-4 particles. . 100

6.5 Visualization of fluidization at different time instants for (a) AR-4 and (b) AR-1 particles at 1.6U_{mf}. 101
6.6 Visualization of fluidization at different time instants for (a) AR-4 and (b) AR-1 particles 2.9U_{mf}. 102
6.7 Histogram of void fractions for cells below z = 0.3 m (total of 2000 cells) for AR-1 and AR-4 (MP) particles at (a) 1.6U_{mf}, (b) 2U_{mf}, (c) 2.3U_{mf} and (d) 2.9U_{mf}. 103
6.8 Snapshots of bubble formations for (a) AR-1 and (b) AR-4 (MP) particles at 1.7U_{mf} in the middle intersection of the bed (0.07 m ≤ y ≤ 0.08 m). 103
6.9 Effects of considering hydrodynamic lift and torque on (a) mixing entropy and (b) mixing time for AR-4 particles 105

B.1 Example of analyzing audio signal for AR-1 particles at $U - U_{mf} = 0.65$; (a) Original audio signal, (b) Intensity of original signal, (c) Intensity after applying low pass filter, (d) Filtered signal after applying threshold. 116
B.2 Waiting time distributions for AR-1 particles at excess gas velocities $U - U_{mf}$ of: (a) 0.4, (b) 0.65, (c) 0.9, (d) 1.15 and (e) 1.4 m/s. 117

LIST OF TABLES

2.1 Table of the lift and torque correlation functions from [3] and [2] used in this study. The fitting coefficients are provided in the Appendix A. 13
2.2 Relevant parameters for the CFD-DEM algorithm. 17
2.3 Hydrodynamic force cases explored in this study. 19

3.1 Dimensions and properties of the experimental setup. 39
3.2 Particle properties. 40

4.1 Particle properties. 58

5.1 Coefficients for drag force calculation as proposed by Sanjeevi et al. [3],[5]. 75
5.2 Coefficients for the lift and torque correlations with the functional form of Zastawney *et al.* [2] fitted for spherocylinder particles with aspect ratio of 4 using in-house DNS simulations [3]. 76
5.3 Coefficients for torque calculation (Eq. 5.22) as proposed by Sanjeevi et al. [5] 77
5.4 Relevant parameters for the CFD-DEM algorithm. 78
5.5 Particle properties. 78
5.6 Correlations applied for single particle (SP) correlations and multi-particle (MP) correlations. 79

6.1 Correlations for hydrodynamic forces applied in this study. 91
6.2 Coefficients for drag force calculation as proposed by Sanjeevi et al. [3],[5]. 93
6.3 Coefficients for torque calculation (Eq. 6.25) as proposed by Sanjeevi et al. [5] 95
6.4 Relevant parameters for the CFD-DEM algorithm. 96
6.5 Particle properties. 97

A.1 Coefficients for the lift and torque correlations of Zastawny *et al.* [2] fitted for spherocylinder particles with aspect ratio of 4 using in-house DNS simulations. 112
A.2 Coefficients for the lift and torque correlations of Sanjeevi *et al.* [3] for a spherocylinder particle with aspect ratio of 4. 113

1

INTRODUCTION

1.1. FLUIDIZATION

When discussing chemical reactions and chemical engineering one usually imagines two liquids mixing and reacting in a test tube or large industrial reactors. However, in industry it is often necessary to manipulate large amounts of powders or granular materials. The most effective way to do so proved to be fluidization. This phenomenon occurs if a fluid passes upwards, through a layer of powder or granular particles at high enough flow rate [6]. Under these conditions the bed expands and the whole mass of particles starts to behave and shows properties that look very much like a boiling liquid. Fluidized conditions are ideal for manipulating large amounts of granular material, with large flexibility in operating conditions. This process offers high contact between fluid phase and solid particles, rapid mixing of solid particles, and a high heat transfer rate between the fluid phase and solids with the ability to maintain a uniform temperature. The equipment in which such processes occur are called fluidized beds and due to their advantages they have become irreplaceable in industry. Typical processes in which fluidized beds are the central equipment are: coal gasification, gasoline production from other petroleum fractions and natural or synthesis gases, different synthesis reactions, coating and drying of solids, water treatment and metallurgical processes and heat exchange.

In recent decades, with the increase of need to diversify our energy sources with more sustainable and renewable ones, fluidized beds have become promising equipment, specifically in dealing with biomass energy sources. An important property that distinguishes the use of fluidized beds in this kind of process from well established ones is that the particles are considerably larger and characterized by an elongated shape. Some typical examples of biomass particles can be seen in Fig. 1.1. As almost all understanding of fluidized bed operations comes from processes in which particles are mostly powder like and approximately spherical, the question arises if this understanding can simply be translated to fluidized beds with large and elongated particles.

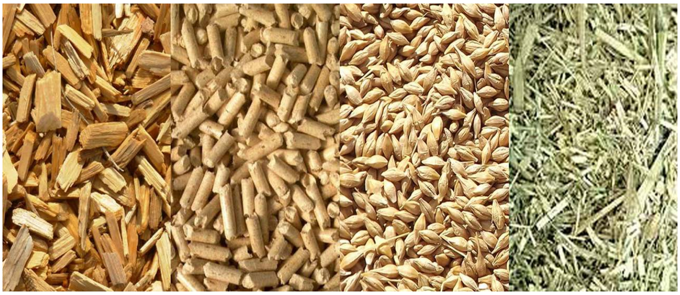

Figure 1.1: Typical example of biomass materials, form wood chips, wood pellets to straw-like material.

The design and optimization of fluidized bed reactors relies on numerical models that are successful in predicting the behavior of fluidized beds with spherical particles and can do so even on industrial scales, with millions of particles. In case of fluidized beds containing elongated particles usage of these models, approximating the elongated particle shape as spherical, is questionable. It is clear that elongated particles will have much more complex particle-particle interactions as well as more complex and even additional hydrodynamic forces (see chapter 2). However, the effect and importance of these differences on larger scale, in dense fluidizing conditions, is still not well understood. Note that in many applications the elongated biomass particles are mixed with more-or-less spherical particles. For example, biomass gasification is often taking place in a bed containing sandlike particles. This is not only done to improve the heat management, but also to prevent fluidization problems occurring at high biomass fractions.

From the introduction of fluidized beds in industrial processes, in the first half of the 20th century, its path to commercial success was difficult and followed by a number of failures. The root cause for these difficulties came from a lack of understanding of the fundamental processes that occur inside of the fluidized bed reactor. In order to avoid similar difficulties in the development and optimization of fluidized beds with elongated particles it is necessary to fully understand their behavior during the fluidization process. The first step in doing so is defining their specifics and identifying the main difficulties in correct prediction of their behavior.

1.2. SPECIFICS OF ELONGATED PARTICLES

When comparing the fluidization behavior of elongated particles to spherical ones, the most obvious difference comes from the particle-particle interactions. In case of spherical particles, all particle collisions are symmetric, unlike for elongated particles where the majority of collisions are asymmetric, as can be seen in Figure 1.2. Resolving collisions between elongated particles is obviously more complex due to the different orientations that particles can assume and due to the relatively larger torque (compared to volume-equivalent spheres) that is generated during collisions. The problem of resolving particle-particle interactions in Computational Fluid Dynamics - Discrete Element Model (CFD-DEM) simulations of elongated particles was addressed by Mahajan et al. (2018) [7]. This thesis will mainly focus on the effect of fluid-particle interactions.

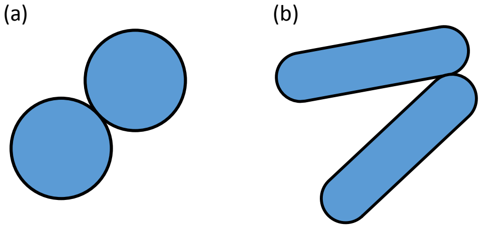

Figure 1.2: Typical example of particle collisions for (a) spherical and (b) spherocylindrical particles.

The force that the fluid exerts on the particles is the main driver of fluidization. Therefore properly resolving fluid-particle interactions is of utmost importance for successful simulations of elongated particles fluidization. Properly estimating the hydrodynamic forces that act on elongated particles is challenging as they depend on particle orientation to the mean fluid flow. When an elongated particles is inclined under some angle to the fluid flow, next to a drag force, the fluid will also exert a shape induced lift force and hydrodynamic torque on the particle. These phenomena have until recently been neglected in all simulations of elongated particles, on the one hand because they were considered to be negligible compared to the drag force and on the other hand because there were no correlations that could take them in to account in CFD-DEM simulations.

Moreover, during fluidization, particles most of the time find themselves in dense fluidizing conditions where crowding effects, caused by surrounding particles, have an effect on the hydrodynamic forces and torque that the particles experience. For spherical particles there are a number of correlations that take this crowding effect into account. However, for elongated particles this is not the case. The first correlations for hydrodynamic forces and torque on elongated particles in a crowded environment were developed quite recently by Sanjeevi et al. (2020) [5]. Because so far these correlations have not yet been applied in CFD-DEM simulations, their exact effect and importance is still not known. In order to properly simulate fluidization of elongated particles all these issues need to be addressed.

1.3. SCOPE OF THESIS

The goal of this thesis is to deepen the understanding of fluidization of elongated particles. Because the parameter space is already very large, to keep the amount of work manageable, we will limit ourselves to systems containing all the same (monodisperse) elongated particles, in most cases of aspect ratio 4. This will serve as a basis of future work focusing also on mixtures of particles of different shape. To reach our goal, we will use both CFD-DEM simulations (Chapters 2, 5 and 6) and different 3D experimental techniques (Chapters 3 and 4). Specifically, in this thesis we will try to answer the following questions:

1. What is the effect and importance of shape induced lift force and hydrodynamic torque on the fluidization behavior of elongated particles?
2. What is the effect and importance of using multi-particle correlations for hydrodynamic forces?
3. What are the essential differences in fluidization behavior between spherical and elongated particles?

1.4. OUTLINE OF THESIS

This thesis is arranged in seven chapters outlined below:

Chapter 2, "Effect of lift force and hydrodynamic torque on fluidization of non-spherical particles" where we compare results from CFD-DEM simulations of elongated particles of aspect ratio 4 with different hydrodynamic forces and torque considered. In this chapter we show the effects of considering shape induced lift force and hydrodynamic torque on fludization behavior of elongated particles.

Chapter 3, "Fluidization of spherical versus elongated particles - experimental investigation using Magnetic Particle Tracking" where we use a non-invasive 3D experimental technique (magnetic particle tracking - MPT) to compare fluidization behavior of spherical to elongated particles. We looked into fluidization of elongated particles of aspect ratio 4 and 6 at different inlet gas velocities.

Chapter 4, "Fluidization of spherical versus elongated particles - experimental investigation using X-ray tomography" where we use X-ray computer tomography to look into bubble or slugging properties for spherical and elongated particles of aspect ratio 4. Our findings about slugging frequencies, obtained using X-ray tomography, are supported by a cheap and simple sound signal analysis shown in Appendix B.

Chapter 5, "Fluidization of elongated particles - effect of multi-particle correlations (drag, lift and torque) in CFD-DEM simulations" where we apply multi-particle correlations for hydrodynamic forces and torque in CFD-DEM simulations and compare them with simulations using previously known single particle correlations. The multi-particle correlations are validated by comparing with the results obtained from MPT experiments from Chapter 3.

Chapter 6, "Spherical versus elongated particles - numerical investigation of mixing characteristics in a gas fluidized bed" where we use CFD-DEM simulations to compare vertical mixing characteristics between spherical and elongated particles of aspect ratio 4.

Chapter 7, "Conclusion" where we summarize the main conclusions and give recommendations for future work.

2

EFFECT OF LIFT FORCE AND HYDRODYNAMIC TORQUE ON FLUIDIZATION OF NON-SPHERICAL PARTICLES

The aim of many industrial processes is to manipulate solid particle aggregates within gas suspensions. Prime examples of such processes include fluidised bed reactors, cyclone separators and dust collectors. In recent years, fluidised bed reactors have been used in gasification of biomass particles. When fluidised, these particles are subject to various hydrodynamic forces such as drag, lift and torque due to interactions with the fluid. Computational approaches, which can be used to replicate laboratory and industrial scale processes, offer a crucial method for the study of reactor design and for the formulation of optimal operating procedures. Until now, many computer models have assumed particles to be spherical whereas in reality biomass feedstocks typically consist of non-spherical particles. While lift and torque are of minimal importance for spherical particles, non-spherical particles experience varying lift force and torque conditions, depending on particle orientation relative to the direction of the fluid velocity. In this study, we present a numerical investigation on the effect of different lift force and torque correlations on fluidised spherocylindrical particles. We find that lift force has a significant influence on particle velocities parallel to the direction of gravity. On the other hand, particle orientation is dependent on hydrodynamic torque. Results from this numerical study provide new insight with regards to the dynamics of non-spherical particles that can be of paramount importance for industrial processes involving non-spherical particles.

Part of this chapter has been published in Chemical Engineering Science **195**, 642–656 (2019) [8].

2.1. INTRODUCTION

MANY industrial processes such as fluidised bed reactors, cyclone separators, dust collectors and pulverised-coal combustors involve the processing of dense gas-solid flows. These devices are categorised as gas-solid contactors, of which the fluidised bed reactor is a proto-typical example [7, 9–11]. Due to their favourable mass and heat transfer characteristics, gas-fluidised beds are utilised in a number of industries such as the chemical [12, 13], petrochemical [14, 15] and energy industries [16, 17].In addition, fluidised bed reactors are used in large-scale operations involving the granulation, drying and synthesis of fuels, base chemicals and polymers [11]. In recent years there has been increased application of fluidised beds in biomass gasification [18–21] using a variety of raw materials such as rice husks [22], cooking oil [17] and willow [23]. Hence, the prediction of the response of dense gas-solid flows in fluidised reactors via computational investigation is highly important for both reactor design and the determination of optimal operating conditions for a variety of important applications. However, simulations of dense gas-solid flows generally represent the solid phase as perfect spherical entities whereas, in reality, the solid biomass phase is composed of discrete particles of varying non-spherical geometries [7, 24–27].

Describing non-spherical particles in simulations can give rise to a variety of issues. While spheres can be described by a single parameter, i.e. diameter, non-spherical particles require more parameters. Even regular non-spherical shapes, such as ellipsoids or spherocylindrical particles, require at least two parameters to account for their geometry. For highly irregular particle shapes, the computational demands with regards to the detection of particle-particle interactions, and the calculation of resulting contact forces, drastically increase. An additional concern is the determination of the hydrodynamic forces and torques acting on particles due to the fluid flow. For non-spherical particles, the hydrodynamic forces, such as drag, transverse lift and pitching torque, can vary appreciably with particle orientation, and thus crucially dictate the translational motion of particles. Pitching torque is generated when the centre of pressure associated with the total aerodynamic force does not act through the centre of mass of a specific particle. Drag force, lift force and pitching torque can be characterised by dimensionless coefficients that depend on particle velocity and orientation relative to the flow as well as the Reynolds number (Re). A number of drag force coefficients for non-spherical particles are available in the literature [3, 28–32] while, recently, lift coefficient correlations [2, 3, 33–35] and torque coefficient correlations [2, 3] have also been defined for non-spherical particles.

For a dilute particle suspension and depending on the Reynolds number, the lift force can be more than half the drag force for non-spherical particles in a gas flow [36]. As a result, lift can significantly influence the trajectory of non-spherical particles [3, 32, 33]. However, it is not clear how lift force will affect non-spherical particles in dense systems such as those encountered in dense gas-fluidised systems. Similarly, the effect and importance of pitching torque on non-spherical particles under fluidised conditions is also poorly understood. In this chapter, we present a preliminary investigation on the effect of varying lift and torque conditions on non-spherical particles, specifically spherocylindrical particles, in a laboratory scale gas-fluidised bed reactor. We will employ a series of lift and torque correlations that have been derived for single isolated particles [2, 3, 32] as an initial approximation of the lift and torque experienced by spherocylindrical particles during fluidization. We present results on the relevance of varying lift and pitching torque conditions for sphercylindrical particles by studying particle dynamics, velocity profiles, particle orientations, and angular momentum in a reactor.

This chapter is arranged as follows. We will first outline the CFD-DEM numerical model used in this study focusing on the implementation of contact detection, drag forces, lift forces and pitching torque for spherocylindrical particles (Section 2.2). Thereafter we present the simulation parameters for this study in Section 2.3. In Section 2.4 we explore the effect of varying lift and torque conditions in dense fluidised beds. Finally, we draw conclusions from this study and provide an outlook for future investigations.

2.2. NUMERICAL APPROACH

For this study we implement the CFD-DEM algorithm to simulate a coupled particle-fluid system, which has been extensively employed to simulate systems where particle-fluid interactions are relevant [26, 37–42]. The CFD component of the algorithm is solved using the Open Source package OpenFOAM while the DEM component is implemented using LIGGGHTS, which stands for LAMMPS Improved for General Granular and Granular Heat Transfer Simulations, and is an Open Source package for modelling granular material via the discrete element method (DEM). Coupling of the CFD and DEM components is facilitated by the Open Source coupling engine CFDEM, which executes both the DEM solver and CFD solver consecutively. The CFDEM engine allows for execution of the program for a predefined number of time steps after which data is exchanged between the OpenFOAM solver and LIGGGHTS solver [43]. In this study the open source codes have been adapted for the implementation of spherocylindrical particles and further details on the CFD-DEM approach can be found in the paper of Mahajan *et al.* [7].

2.2.1. DISCRETE ELEMENT METHOD (DEM)

To simulate interactions between the solid spherocylindrical particles we use the discrete element method (DEM), a soft contact model first introduced by Cundall and Strack (1979) to describe interactions between granular particles [44]. The simplest DEM contact model approximates grains as either disks in 2D or spheres in 3D, an approach that is sufficient to replicate laboratory-scale force chains [45, 46] and depict percolation-like contact networks [47]. In DEM, the trajectory of each particle is numerically integrated over time and subject to local contact forces and torques. Inter-particle forces develop only when particles spatially overlap.

We have adapted the DEM model to describe the interaction of spherocylinders with rotational and translational degrees of freedom. Consider a spherocylinder particle i in a dense gas-fluidized reactor. The translational motion for spherocylinder i can be calculated by integrating the expression

$$m_i \frac{d\mathbf{v}_i}{dt} = \sum_j \left(\mathbf{F}_{ij,n} + \mathbf{F}_{ij,t}\right) + \mathbf{F}_{i,f} + \mathbf{F}_{i,p} + \mathbf{F}_{i,b} \qquad (2.1)$$

where the sum runs over all neighbours j in contact with particle i, $\mathbf{F}_{ij,n}$ is the normal contact force acting on particle i due to its interaction with particle j, $\mathbf{F}_{ij,t}$ is the tangential contact force acting on on particle i due to its interaction with particle j, $\mathbf{F}_{i,f}$ is the total hydrodynamic force acting on the particle, $\mathbf{F}_{i,p}$ represents the pressure gradient (buoyancy) force acting on the particle and $\mathbf{F}_{i,b}$ is the body force acting on the particle including gravity. Further details on the hydrodynamic forces acting on the particle are presented in the next section. The rotational motion of a particle i can be solved using

$$\frac{d(\mathbf{I}_i \cdot \boldsymbol{\omega}_i)}{dt} = \sum_j \mathbf{T}_{ij} + \mathbf{T}_{i,f} \tag{2.2}$$

where $\mathbf{I}_i$ is the particle moment of inertia tensor, $\boldsymbol{\omega}_i$ is the angular velocity of the particle, $\mathbf{T}_{ij}$ is the contact torque acting on the particle i due to its interaction with neighbouring particle j, and $\mathbf{T}_{i,f}$ is the fluid-induced pitching torque. Note that for spherical particles, the contact torque $\mathbf{T}_{ij}$ is only caused by tangential contact forces. However, for non-spherical particles the torque is caused by *both* tangential and normal contact forces. Particle orientations are described by quaternions in the algorithm. For this study the equations of motion are integrated using the Velocity Verlet method.

Fig. 2.1 shows an example of an overlapping contact between two spherocylinder particles P_1 and P_2. The identification of contacts between spherocylindrical particles, and the subsequent calculation of the overlap region, is more complicated than in case of spheres. Two adjacent spherocylindrical particles are deemed to be overlapping once the distance between their shafts is smaller than the sum of their radii. For particle P_i, R is the characteristic radius or radius of the spherical part of the spherocylinder, $\mathbf{r}_i$ is the centre of mass, L is the shaft length, $\mathbf{u}_i$ is the orientation unit vector originating at $\mathbf{r}_i$ and $\mathbf{v}_i$ is the translational velocity. Two spherocylindrical particles are deemed to be in contact when the shortest distance between the the central axes is less than the sum of the particle radii i.e. $|\mathbf{s}_2 - \mathbf{s}_1| < 2R$ where $\mathbf{s}_1$ and $\mathbf{s}_2$ are points on the central axes of P_1 and P_2 respectively. The mid-point between $\mathbf{s}_1$ and $\mathbf{s}_2$ is the contact point $\mathbf{r}_c$, the degree of overlapping distance between the particles is δ_n, and $\mathbf{n}_{12}$ and $\mathbf{t}_{12}$ are the normal and tangential unit vectors for the contact respectively. A spherocylinder contact detection algorithm originally developed for granular flows has been used in this study [48–51].

To calculate the normal contact force exerted on particle P_1 by particle P_2 we use a linear spring-dashpot model such that the normal contact force is given by

$$\mathbf{F}_{12,n} = -k_n \delta_n \boldsymbol{n}_{12} - \eta_n \mathbf{v}_{12,n} \tag{2.3}$$

where k_n is the normal spring constant, η_n is the normal damping coefficient and $\mathbf{v}_{12,n}$ is the normal relative velocity between the particles. As shown in Eq. (2.3), the normal contact force is dependent on the degree of overlapping distance δ_n, which is calculated with the aforementioned collision detection scheme for spherocylinders. Using the degree of overlapping or penetrating volume instead of overlapping distance can lead to better resolved normal and tangential forces [52]. In addition, when the overlap distance is used for the normal contact force, the volume of the overlap region is effectively ignored and particle volume is not conserved. This can have ramifications for the calculation of local volume fraction, and thus affect the calculation of the coupling between

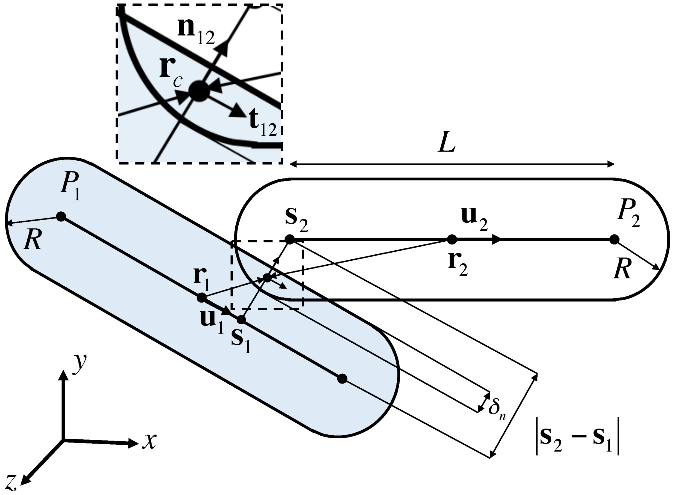

Figure 2.1: A schematic of a sample contact between two spherocylinders with each having a shaft length L and characteristic radius R. The inset image shows details of the normal and tangential unit vectors at the contact.

the solid and fluid phases. To overcome this issue, the volume of the overlapping region can be redistributed over the remaining surface of the particle, as demonstrated for spherical particles [53]. This issues are prevalent for more detailed, pure granular studies and in dense and compact granular configurations. However, as we aim to study the fluidization of spherocylinder particles above the minimum fluidization velocity, persistent compact particle domains are unlikely with particles more likely to be airborne and briefly contacting a smaller number of particles. Hence, we use simplified approach based upon overlapping distance without accounting for overlapping volume as an approximation. The tangential contact force is calculated from the Coulomb-type friction expression

$$\mathbf{F}_{12,t} = \min(|-k_t \boldsymbol{\delta}_t \boldsymbol{t}_{12} - \eta_t \mathbf{v}_{12,t}|, -\mu|\mathbf{F}_{12,n}|). \tag{2.4}$$

In this expression k_t, $\boldsymbol{\delta}_t$, η_t, μ and $\mathbf{v}_{12,t}$ are the tangential spring constant, tangential overlap, tangential damping coefficient, friction coefficient and tangential relative velocity respectively. $\boldsymbol{\delta}_t$ is calculated from the time integral of the tangential relative velocity since the development of the initial particle contact and given by

$$\boldsymbol{\delta}_t = \int_{t_{c,0}}^{t} \mathbf{v}_{12,t} dt \tag{2.5}$$

where $t_{c,0}$ is the time of initial contact between the particles. This expression represents the elastic tangential deformation of the particles since the onset of particle contact. Interactions between the walls and particles are also modelled using the linear spring-dashpot approach of Eq. (2.3) with the tangential expression given by Eq. (2.4).

2.2.2. COMPUTATIONAL FLUID DYNAMICS (CFD)

In CFD-DEM, the fluid is treated as a continuum in which fluid flow features such as boundary layers or vortex shedding are not resolved. Rather, their effects are included through correlations of drag and lift forces. The fluid phase is described on basis of the volume-averaged Navier-Stokes equations, which are discretised on a uniform grid, and fluid calculations are based upon the standard k-ϵ turbulence model. The equation of continuity is given by

$$\frac{\partial(\epsilon_f \rho_f)}{\partial t} + \nabla \cdot (\epsilon_f \rho_f \mathbf{v}_f) = 0 \tag{2.6}$$

where ϵ_f is the fluid volume fraction, ρ_f is the fluid density and $\mathbf{v}_f$ is the fluid velocity. The expression for momentum conservation is given as

$$\frac{\partial(\epsilon_f \rho_f \mathbf{v}_f)}{\partial t} + \nabla \cdot (\epsilon_f \rho_f \mathbf{v}_f \mathbf{v}_f) = -\epsilon_f \nabla p + \nabla \cdot (\epsilon_f \boldsymbol{\tau_f}) + \mathbf{R}_{f,p} + \epsilon_f \rho_f \mathbf{g} \tag{2.7}$$

where $\boldsymbol{\tau}_f$ is the stress tensor for the fluid phase, $\mathbf{g}$ is gravity, and $\mathbf{R}_{f,p}$ represents the momentum exchange between the fluid and particle phase. The latter is obtained by distributing the particle interactions with the fluid phase using the following expression [54]

$$\mathbf{R}_{f,p} = -\frac{\sum_{p=1}^{N_p} (\mathbf{F}_D^p + \mathbf{F}_L^p)}{V_{\text{cell}}} \tag{2.8}$$

where p is the particle label, N_p is the number of particles in the computational fluid cell, $\mathbf{F}_D^p$ is the drag force acting on particle p due to the fluid, $\mathbf{F}_L^p$ is the lift force acting on particle p due to the fluid, and V_{cell} is the volume of the computational fluid cell. We do not consider two-way coupling of the torque since it has negligible localized effects on the fluid. Expressions for the hydrodynamic forces are outlined in the proceeding sections.

DRAG FORCE

The drag force on a single particle $\boldsymbol{F}_{D0}$, in the absence of neighbouring particles, acts in the direction of relative velocity between fluid and particle and is expressed as

$$\mathbf{F}_{D0} = \frac{1}{2} C_D \rho_f \frac{\pi}{4} d_p^2 \left| \mathbf{v}_f - \mathbf{v}_i \right| (\mathbf{v}_f - \mathbf{v}_i) \tag{2.9}$$

where C_D is the drag coefficient, d_p is the particle volume equivalent diameter or the diameter of a sphere with the same volume as the spherocylinder, $\mathbf{v}_f$ is the fluid velocity interpolated to the location of particle i, and $\mathbf{v}_i$ is the velocity of particle i. A number of drag correlations have been developed in the past that account for particle shape [2, 29, 30, 33, 35, 55]. In this study, as an approximation, we employ the drag force correlation for arbitrary shaped particles established by Hölzer and Sommerfeld [30]

	Correlation Type	**Correlation Expression**
Zastawny *et. al* (2012) [2]	Lift	$C^Z_{L,\alpha} = (\frac{b^Z_1}{Re^{b^Z_2}} + \frac{b^Z_3}{Re^{b_4}})\sin(\alpha)^{b^Z_5 + b^Z_6 Re^{b^Z_7}}$ $\cos(\alpha)^{b^Z_8 + b^Z_9 Re^{b^Z_{10}}}$
Sanjeevi *et. al* (2018) [3]	Lift	$C^S_{L,\alpha} = (\frac{b^S_1}{Re} + \frac{b^S_2}{Re^{b^S_3}} + \frac{b^S_4}{Re^{b^S_5}})\sin(\alpha)^{1 + b^S_6 Re^{b^S_7}}$ $\cos(\alpha)^{1 + b^S_8 Re^{b^S_9}}$
Zastawny *et. al* (2012)	Torque	$C^Z_{T,\alpha} = (\frac{c^Z_1}{Re^{c^Z_2}} + \frac{c^Z_3}{Re^{c^Z_4}})\sin(\alpha)^{c^Z_5 + c^Z_6 Re^{c^Z_7}}$ $\cos(\alpha)^{c^Z_8 + c^Z_9 Re^{c^Z_{10}}}$
Sanjeevi *et. al* (2018)	Torque	$C^S_{T,\alpha} = (\frac{c^S_1}{Re^{c^S_2}} + \frac{c^S_3}{Re^{c^S_4}})\sin(\alpha)^{1 + c^S_5 Re^{c^S_6}}$ $\cos(\alpha)^{1 + c^S_7 Re^{c^S_8}}$

Table 2.1: Table of the lift and torque correlation functions from [3] and [2] used in this study. The fitting coefficients are provided in the Appendix A.

$$\begin{aligned} C_D = \frac{8}{\mathrm{Re}_p}\frac{1}{\sqrt{\Phi_\parallel}} + \frac{16}{\mathrm{Re}_p}\frac{1}{\sqrt{\Phi}} + \frac{3}{\sqrt{\mathrm{Re}_p}}\frac{1}{\Phi^{3/4}} \\ +0.42 \times 10^{0.4(-\log\Phi)^{0.2}}\frac{1}{\Phi_\perp} \end{aligned} \tag{2.10}$$

where Re_p is the particle Reynolds number $\mathrm{Re}_p = \rho_f d_p \left|\mathbf{v}_f - \mathbf{v}_i\right| / \mu_f$ with μ_f being the fluid viscosity, Φ is the particle sphericity, $\Phi_\parallel$ is the lengthwise sphericity and $\Phi_\perp$ is the crosswise sphericity. Besides being universally applicable to different shapes and easy to implement, this expression is quite accurate given that it has a mean relative deviation from experimental data of only 14.1%, significantly lower than previous expressions [56, 57].

In a dense gas-fluidized system, the drag force acting on a given particle will be affected by neighbouring particles. To account for this effect, we implement the Di Felice modified drag force expression [58], which was originally derived for spherical particles and is applied here as an approximation for the effect of neighbouring non-spherical particles on the drag force experienced by a non-spherical particle

$$\mathbf{F}_D = \frac{1}{2} C_D \rho_f \epsilon_f^{2-\chi} \frac{\pi}{4} d_p^2 \left|\mathbf{v}_f - \mathbf{v}_i\right| (\mathbf{v}_f - \mathbf{v}_i) \tag{2.11}$$

where χ is a correction factor given by

$$\chi = 3.7 - 0.65 \exp\left[(-(1.5 - \log(\mathrm{Re}_p))^2/2\right] \tag{2.12}$$

where the particle Reynolds number Re_p is calculated using the expression previously defined. A revision of the Di Felice model by Rong *et al.* [59] accounts for the effect of porosity and Re on χ. However, in our previous study [7], we concluded that this extension demonstrated similar behaviors to the Di Felice model. Therefore, we do not consider the expressions of Rong *et al.* in this study.

LIFT FORCE

For non-spherical particles suspended in a fluid flow, a shape induced lift force, similar to the concept of an aerofoil in aerodynamics, can significantly affect the trajectory of a particle. When the axis of an elongated particle, such as the spherocylindrical particles in this study, is inclined to the direction of relative fluid flow the flow fields on the upper and lower sides of the particle differ. The pressure drops in regions of rapid flow while the pressure increases in regions where the fluid velocity decreases [33], thus leading to an asymmetric pressure distribution and inducing a lift force perpendicular to the direction of relative fluid flow. An example of the lift force $\mathbf{F}_L$ due to a fluid flow for a spherocylinder that is not aligned with the direction of fluid flow is shown in Fig. 2.2. Here $\mathbf{v}'_{fi}$ is the relative velocity of the fluid with respect to the particle i. The lift force $\mathbf{F}_L$ is orthogonal to $\mathbf{v}'_{fi}$ and, because of symmetry, lies in the plane defined by the particle orientation vector $\mathbf{u}_i$ and $\mathbf{v}'_{fi}$. For spherocylinder particles, there is no lift force when the central particle axis is perpendicular to or aligned with the direction of relative fluid flow as there will be no resulting pressure difference. However, arbitrary shaped particles can still be subject to a lift force even when they are aligned with the flow direction, similar to effects observed for a cambered airfoil.

The magnitude of the lift force F_L experienced by an isolated spherocylinder is expressed as

$$F_L = \frac{1}{2} C_L \rho_f \frac{\pi}{4} d_p^2 \left|\mathbf{v}_f - \mathbf{v}_i\right|^2 \tag{2.13}$$

where C_L is the lift force coefficient. To ensure that the lift force for a particle is correctly oriented, F_L is multiplied by the lift force orientation vector $\hat{\mathbf{e}}_{L_0}$ which is given as

$$\hat{\mathbf{e}}_{L_0} = \frac{\mathbf{u}_i \cdot \mathbf{v}'_{fi}}{\left|\mathbf{u}_i \cdot \mathbf{v}'_{fi}\right|} \frac{(\mathbf{u}_i \times \mathbf{v}'_{fi}) \times \mathbf{v}'_{fi}}{\left\|(\mathbf{u}_i \times \mathbf{v}'_{fi}) \times \mathbf{v}'_{fi}\right\|} \tag{2.14}$$

The resultant lift force experienced by a particle is then expressed as $\mathbf{F}_L = F_L \hat{\mathbf{e}}_{L_0}$. For this study we use two lift correlation functions [2, 3], which are presented in Table 2.1.

HYDRODYNAMIC TORQUE

As demonstrated in the preceding sections, drag force acts in the direction of relative fluid flow and depends on particle orientation relative to the flow [36], while lift force leads to a force perpendicular to the relative fluid flow [2, 35, 60]. When the centre of pressure $\mathbf{x}_{cp}$ acting on a non-spherical particle does not coincide with the centre of mass of the particle $\mathbf{x}_{cm}$, a hydrodynamic pitching torque results and acts around the axis

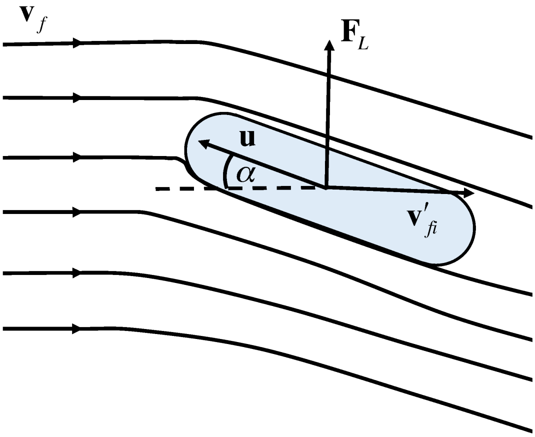

Figure 2.2: Lift vector orientation based on the relative velocity of the fluid with respect to the particle $\mathbf{v}'_{fi} = \mathbf{v}_f - \mathbf{v}_i$ and particle orientation vector $\mathbf{u}_i$. The angle of incidence of the fluid flow α is also indicated on the figure.

perpendicular to the plane of relative fluid velocity $\mathbf{v}'_{fi}$ and particle orientation vector $\mathbf{u}_i$. The torque can change the angle of incidence α of the particle. The development of hydrodynamic torque acting on a spherocylindrical particle is shown in Fig. 2.3. In the figure the angle of incidence α is defined as the angle between the direction of flow and the unit normal joining $\mathbf{x}_{cp}$ and $\mathbf{x}_{cm}$. Note that a particle can also experience rotational torque that acts around the axis of symmetry of the particle. However, we do not include such a rotational torque in this study. For the remainder of this thesis pitching torque is referred to as hydrodynamic torque.

There are only a few studies that have previously focused on the formulation of expressions for hydrodynamic torque. While approximate torque expressions have been generated for different non-spherical particle types [2, 33, 35, 36], the most pertinent expression for this study has been recently derived by Sanjeevi *et al.* [3] for the exact spherocylindrical particles of this study. Hydrodynamic torque can be calculated using two approaches. First, the hydrodynamic torque can be calculated using $\Delta\mathbf{x}$ [36], which is the vector between $\mathbf{x}_{cp}$ and $\mathbf{x}_{cm}$ (Fig. 2.3), and the normal force $\mathbf{F}_n$ acting through $\mathbf{x}_{cm}$ using the expression

$$\mathbf{T} = \Delta\mathbf{x} \times \mathbf{F}_n. \tag{2.15}$$

Here, $\mathbf{F}_n$ is normal component of the sum of all forces acting at $\mathbf{x}_{cp}$. Using an expression for non-spherical particle torques [55], the magnitude Δx can be expressed as a function of α by

$$\Delta x = \frac{L}{4}(1 - (\sin\alpha)^3) \tag{2.16}$$

where L is the particle length.

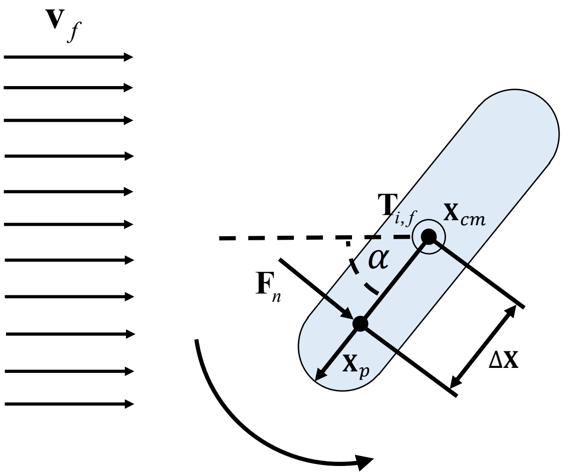

Figure 2.3: A spherocylinder subject to torque. The difference between the centre of pressure $\mathbf{x}_{cp}$ and the centre of mass $\mathbf{x}_{cm}$ leads to the development of a hydrodynamic torque $\mathbf{T}_{i,f}$. $\Delta\mathbf{x}$ is the distance between $\mathbf{x}_{cp}$ and $\mathbf{x}_{cm}$.

In this study, we have employed a second approach for the calculation of the hydrodynamic torque acting on an isolated spherocylinder, which uses an expression similar to that used for the calculation of drag (Eq. (2.9)) and lift (Eq. (2.13)) and expressed as

$$T_P = \frac{1}{2} C_T \rho_f \frac{\pi}{8} d_p^3 \left| \mathbf{v}_f - \mathbf{v}_i \right|^2 \tag{2.17}$$

where C_T is the torque coefficient. The hydrodynamic torque is directed perpendicular to the plane of particle relative velocity and particle orientation vector in Fig. 2.3. Hence, the torque orientation vector $\hat{\mathbf{e}}_{T_0}$ is given by

$$\hat{\mathbf{e}}_{T_0} = \frac{\mathbf{v}'_{fi} \cdot \mathbf{u}_i}{\left| \mathbf{v}'_{fi} \cdot \mathbf{u}_i \right|} \frac{\mathbf{v}'_{fi} \times \mathbf{u}_i}{\left\| \mathbf{v}'_{fi} \times \mathbf{u}_i \right\|} \tag{2.18}$$

The resultant torque is then expressed as $\mathbf{T}_p = T_p \hat{\mathbf{e}}_{T_0}$. For the torque coefficient, we use the expressions in Table 2.1 in this study. We do not include two-way coupling for the hydrodynamic torques i.e. there is a one-way coupling. Therefore we only consider the influence of the flow on the particles. Similar to the lift force, we do not apply the Di Felice approximation to account for the effect of adjacent particles since it has not been derived for pitching torque.

CFD parameters

Parameter	Symbol	Value
Reactor base	L_x, L_y	0.15 m, 0.15 m
Reactor height	H_z	0.99 m
Number of grid cells	n_x^g, n_y^g, n_z^g	10 × 10 × 66
Grid cell dimensions	$c_x = c_y = c_z$	0.015 m
Min. fluidisation velocity	U_{mf}	1.7 m/s
Input fluid velocity	$V_f = 1.7U_{\mathrm{mf}}$	2.89 m/s
Time step	t_{CFD}	$1 \text{ x } 10^{-4}$ s
Fluid density	ρ_f	1.2 kg/m^3

Spherocylinder & DEM parameters

Parameter	Symbol	Value
Number of particles	N_p	30000
Particle length	L	12 mm
Particle width	$2R$	3 mm
Particle aspect ratio	$L/2R$	4
Time step	t_{DEM}	1×10^{-5} s
Particle density	ρ_p	1395 kg/m^3
Initial bed height	h_{init}	0.19 m
Coefficient of friction	μ	0.46
Cofficient of rolling friction	μ_r	0.46
Coefficient of restitution	e	0.43

Table 2.2: Relevant parameters for the CFD-DEM algorithm.

2.3. SIMULATION PARAMETERS AND VOID FRACTION CALCULATION

Parameters for CFD-DEM simulations are presented in Table 2.2. Particle material properties represent alumide particles that have been used in previous fluidisation experiments [7, 26]. Reactor dimensions are equivalent to a laboratory scale apparatus. The incoming fluid velocity is set to $1.7U_{\mathrm{mf}}$ to ensure operation in the bubbly regime. The minimum fluidisation velocity has been estimated from experiments [7, 26]. The simulation time is equal to 18 seconds, which is more than sufficient for the system to attain a steady-state [7]. For the results presented in the next section, we assume that the system has reached steady-state after 5 s and we analyse the remaining 13 s of the simulation.

The dimensions of a grid cell used to solve the fluid flow with CFD are also presented in Table 2.2. In a CFD-DEM study on the fluidization of monodisperse spherical particles, a grid cell size $c_{x,y,z}$ of least $1.6d_p$ has been proposed to accurately solve the fluid and solid phases [61], where d_p is the diameter of the volume equivalent sphere. Additionally, the grid cell size should not exceed $5d_p$, otherwise flow structures cannot be properly resolved. For spherocylinder particles, an additional criterion for an appropriate grid cell size is required such that a particle can be placed at the centre of a grid cell and freely rotated in all directions without intersecting any grid cell boundary. This avoids particle from occupying 3 consecutive cels in any particular direction. A grid size of $2.83d_p$ can satisfy both criterions for the spherocylinders considered in this study. The size of the grid cell is also of relevance for the calculation of the drag force experienced by a particle (Eq. (2.11)). If the grid cell is too small, the local void fraction ϵ_f will be underestimated given that a cell may be almost entirely filled with a solid particle. Hence, the drag force as calculated with the Di Felice expression will be overestimated. In addition, a grid cell that is too small can lead to inaccurate solution of the continuity (Eq. (2.6)) and momentum conservation (Eq. (2.7)) expressions associated with the fluid. However, if the grid cell is too large, then local heterogeneities in the bulk and near boundaries cannot be resolved.

Finally, we present the approach used to calculate the fluid void fraction ϵ_f in each grid cell, which is required to solve the continuity equation (Equation (2.6)), the momentum conservation equation (Equation (2.7)), and for the calculation of the drag force on the particle. Calculation of the solid fraction contribution of a particle to any grid cell $\epsilon_s = 1 - \epsilon_f$ is subject to the following procedure. First, each particle is populated with a number of evenly-spaced satellite points n_{sp} throughout the particle volume where each point is assigned an equal weight or fraction of the particle volume. Second, the parent cell for a given particle is identified subject to the centre of mass position vector $\mathbf{r}_i$. Third, the particle volume is assigned to the parent cell and the adjacent cells subject to the location of the satellite points on the underlying grid. If the entire particle volume is located within the parent cell then no distribution of particle volume is necessary. If desired, the procedure can be optimised to allow for variation of n_{sp}.

2.4. RESULTS

We now present simulation results of fluidised spherocylindrical particles subject to varying conditions of drag, lift and torque. We will present results for seven different hydrodynamic force conditions, which are summarised in Table 2.3. We consider one case where lift and torque are absent, denoted as “Drag only” for this study. In the “Drag only” case, the drag force includes the correlation of Holzer and Sommerfeld (Eq. (2.10)) with the Di Felice approximation (Eq. (2.11)) to account for the effects of surrounding particles on the drag. Thereafter all cases include this description of drag force. For the other cases, we consider varying lift and torque conditions using the correlation functions of Zastawny *et al.* [2] and Sanjeevi *et al.* [3] as specified in Table 2.1. We consider two cases of differing lift force (L_{Zast} and L_{Sanj}), two cases of differing torque force (T_{Zast} and T_{Sanj}) and two cases with both lift and torque (All_{Zast} and All_{Sanj}).

2.4.1. PARTICLE DYNAMICS

Figure 2.4 shows five characteristic snapshots of a typical fluidisation cycle for two different hydrodynamic cases. In Fig. 2.4 (a) we present a fluidisation cycle for a “Drag only” case while Fig. 2.4 (b) shows the same cycle for a case where drag is supplemented with lift and torque (All_{Sanj}) from Sanjeevi *et al.* [3]. Both cycles start with an initial bed

Case Label	**Drag Force**	**Lift Force**	**Hydrodynamic Torque**
Drag only	Holzer-Sommerfeld	N/A	N/A
L_{Zast}	Holzer-Sommerfeld	Lift, Zastawny *et al.*	N/A
L_{Sanj}	Holzer-Sommerfeld	Lift, Sanjeevi *et al.*	N/A
T_{Zast}	Holzer-Sommerfeld	N/A	Torque, Zastawny *et al.*
T_{Sanj}	Holzer-Sommerfeld	N/A	Torque, Sanjeevi *et al.*
All_{Zast}	Holzer-Sommerfeld	Lift, Zastawny *et al.*	Torque, Zastawny *et al.*
All_{Sanj}	Holzer-Sommerfeld	Lift, Sanjeevi *et al.*	Torque, Sanjeevi *et al.*

Table 2.3: Hydrodynamic force cases explored in this study.

expansion (1) which terminates with a maximum bed expansion (3). The bed then releases and eventually returns to a configuration ready to undergo the fluidisation cycle once more. While it is difficult to decipher any differences between the cycles, there is some visual evidence to suggest that the particles are horizontally orientated to a greater extent upon the start of release for the case including lift and torque forces (Stage (4) in Fig. 2.4 (b)). We will explore this response quantitatively in the proceeding sections.

Figure 2.5 shows the variation of the temporally-averaged number of particles or particle occupancy $\langle n_p \rangle$ with with reactor height in the z-direction for a number of hydrodynamic force cases. We note that variation of $\langle n_p \rangle$ with z is effectively invariant to changes in the hydrodynamic force conditions. The dip in $\langle n_p \rangle$ for $z < 4$ is due to the proximity of this domain to the fluidisation velocity, which leads to a slightly lower density of particles in this layer by pushing the particles into the layers above. The upper domain of the reactor $z > 30$ is quite dilute with $\langle n_p \rangle \leq 2$.

2.4.2. PARTICLE VELOCITY ALONG z-AXIS

Figure 2.6(a) shows a snapshot of the fluidized bed with rigid boundaries located along the x-axis and y-axis. We sample the particle velocity along the gravity direction (z-axis) denoted as v_z at three positions in the reactor, as shown in Fig. 2.6(b), where $z = 0.0675\,\text{m}$ is closest to the bottom of the reactor or the flow inlet, and $z = 0.3075\,\text{m}$ is furthest for the flow inlet and a region with dilute particle conditions. These positions are approximately midway along the y-axis ($0.06\,\text{m} \leq \text{y} \leq 0.075\,\text{m}$). We have also highlighted these positions in Fig. 2.5. Evidently from snapshot in Fig. 2.6, just as for Fig. 2.5, we find that particle occupancy is higher close to the bottom of the reactor while at the highest position considered here particle flow is more dilute.

We now consider the effect of hydrodynamic force conditions on the particle velocity parallel to the direction of gravity. We constructed temporally averaged profiles along the x-axis in the range $0.0\,\text{m} \leq \text{x} \leq 0.15\,\text{m}$ and for fixed y-axis and z-axis positions as illustrated in Fig. 2.6. The temporally-averaged particle velocity along the z-direction v_z at a given grid cell in the fluidised bed reactor over a specific time interval is calculated using the expression

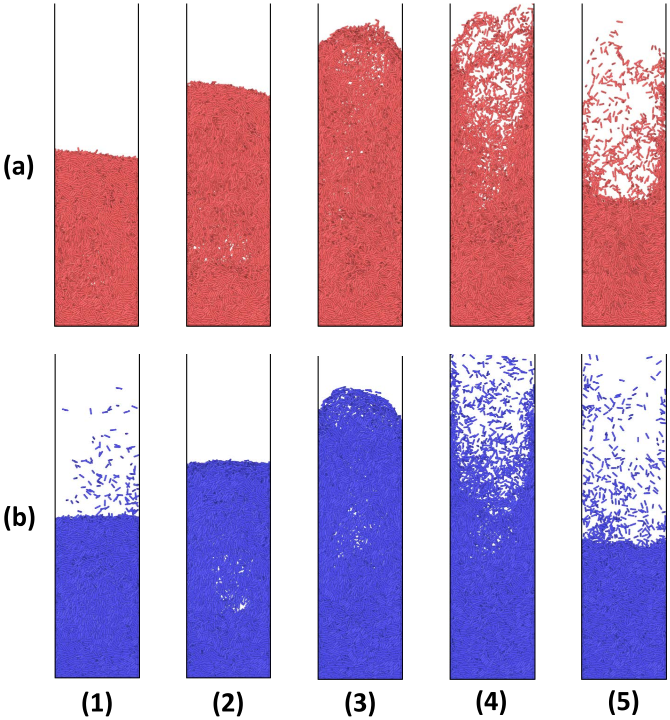

Figure 2.4: Visualisation of a typical fluidisation cycle lasting approximately 1.2 seconds. (a) Drag only. (b) All_{Sanj}. Five characteristic snapshots are shown and labelled as follows: (1) Start of bed expansion; (2) Mid-way of bed expansion; (3) Maximum bed expansion; (4) Start of release; (5) End of release. These system snapshots were visualised using OVITO [1]).

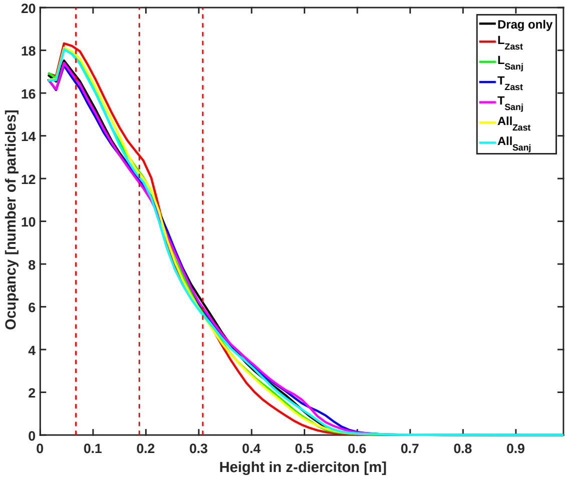

Figure 2.5: Variation in the particle occupancy $\langle n_p \rangle$ with reactor height. The red dashed lines indicate the positions along the z-axis used for the calculation of v_z profiles in section 2.4.2.

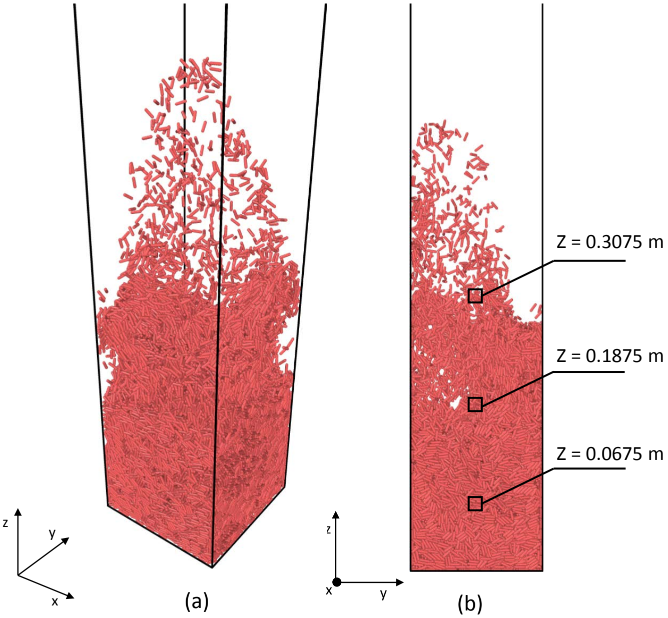

Figure 2.6: (a) Snapshot of the fluidized bed reactor with fluid velocity $1.7U_{mf}$ where the particles hydrodynamic force case is “Drag only”. (b) Analysis positions in the bed reactor along the z-direction. These system snapshots were visualised using OVITO [1]).

$$v_z = \frac{\sum_{t=t_0}^{t_{\text{end}}} \sum_{p=1}^{N_{\text{cell}}(t)} v_z(p,t)}{\sum_{t=t_0}^{t_{\text{end}}} N_{\text{cell}}(t)} \tag{2.19}$$

where t_0 is the start time, t_{end} is the end time, $N_{\text{cell}}(t)$ is the number of particles in the grid cell at time t, p is the particle label and $v_z(p,t)$ is the velocity of particle p in the grid cell at time t. We note that the average velocity v_z is not the same as the average mass flux, because there may be strong correlations between the local solids volume fraction and the instantaneous velocity of a particle. This has recently been shown experimentally for spherocylindrical particles in a pseudo-2D fluidised bed [7]

Figure 2.7 shows that the inclusion of lift has a noticeable effect on v_z throughout the reactor while torque has a negligible effect on v_z. For example, at $z = 0.0675$ m, inclusion of the correlation for lift (L_{Zast}) leads to a large increase in v_z approximately halfway along the x-axis in comparison to the case where particles are only subject to drag. We observe an analogous behaviour upon consideration of the Sanjeevi lift correlation (L_{Sanj}) although the increase in v_z is lower than with the inclusion of the Zastawny lift correlation (L_{Zast}). Similar trends are also recorded at other heights in the reactor although at $z = 0.3075$ m the differences between the trends are not as pronounced as at $z = 0.0675$ m. This may be attributed in part to the lower particle density, and hence increase in void fraction, at higher positions in the bed. A typical representation of this decrease in particle density is evident in the snapshot of particle fluidisation shown in Fig. 2.6. On the other hand, inclusion of either the Zastawny or Sanjeevi torque correlation has little or no effect on the velocity profiles. For cases with all hydrodynamic forces, there is no significant change in v_z in comparison to cases with just drag and lift force. This demonstrates that torque does not appreciably affect v_z, even in combination with lift force.

The changes in the v_z profiles observed here with the inclusion of lift force are similar to those noted in our previous study of particle dynamics in a small reactor [60]. Here v_z increases halfway along the x-axis upon inclusion of lift force while in the study on a small reactor, we also find a similar increase in v_z along the x-axis. However, in the previous study, we also applied the Di Felice expression to the lift force to further explore effect of varying lift conditions. The results showed that with the Di Felice expression the lift force effects become even stronger.

2.4.3. PARTICLE ORIENTATION

We now consider variations in particle orientation parallel to the direction of flow. Figure 2.8 shows the variation of the temporally-averaged fraction of particles f_p with a certain orientation relative to the z-axis for different hydrodynamic force conditions. If $u_z = \pm 1$ the particle is fully aligned with the flow while at $u_z = 0$ the particle is perpendicular to the flow. All trends are calculated in steady-state using the expression

$$f_p(u_z) = \frac{1}{(t_{\text{end}} - t_0)h_{u_z}} \sum_{t=t_0}^{t_{\text{end}}} \frac{n_p(u_z,t)}{N_p} \tag{2.20}$$

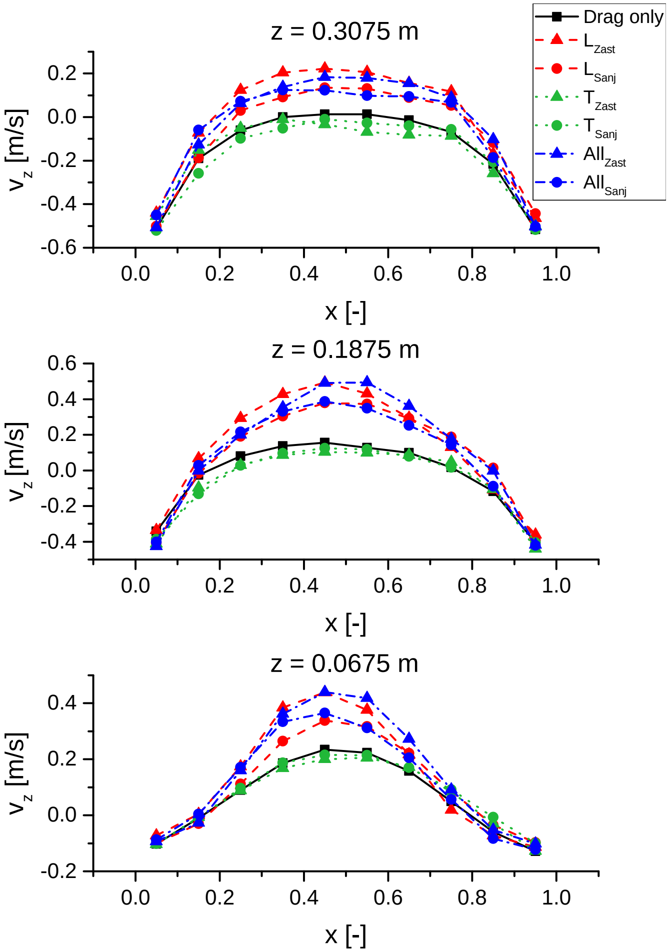

Figure 2.7: Comparison of the temporally-averaged v_z along the x-axis for the positions defined in Figure 2.6(b) in a fluidized bed reactor for different hydrodynamic conditions: Drag only, lift force described by Zastawny (L_{Zast}), lift force described by Sanjeevi (L_{Sanj}), HD Torque described by Zastawny (T_{Zast}) and by Sanjeevi (T_{Sanj}). In these plots x is the position normalised by the length of reactor along the x-axis (0.15 m). Cases with lift force are presented red dashed lines (- - - -), cases with torque with the green dotted line (. . . . .) and cases with all forces included with the blue dash-dot lines. (-·-·-). The filled triangles represents cases of Zastawny *et al.* [2] and the filled circles are cases using the correlations of Sanjeevi *et al.* [3].

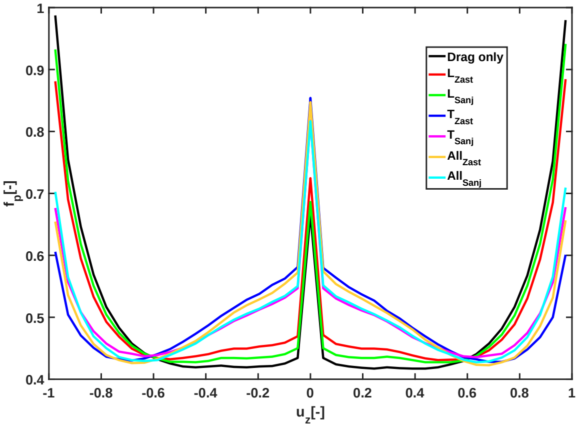

Figure 2.8: Preferred particle orientation. Variation of $f_p(u_z)$ for differing hydrodynamic force conditions.

where $n_p(u_z)$ is the number of particles with an orientation u_z at time t, N_p is the number of particles in the reactor and the bin width $h_{u_z} = 0.05$. Figure 2.8 shows that for the case of drag only and the cases with drag and lift only the majority of particles tend to align with the direction of the fluid flow. From the figure it can also be concluded that the introduction of lift has little or no effect on the preferred orientation of particles. Upon inclusion of the hydrodynamic torque expressions there is a discernible change in the trend with the majority of particles tending to orient perpendicular to the flow. This is demonstrated for both Zastawny's and Sanjeevi correlation functions. Inclusion of lift force along with drag and torque leads to little or no change in the preferred orientation of particles as observed for cases with all forces described by Zastawny and Sanjeevi correlations ($\mathrm{All}_{\mathrm{Zast}}$ and $\mathrm{All}_{\mathrm{Sanj}}$).

While Fig. 2.8 demonstrates the average orientation of particles with respect to the z-axis, it does not provide information with regards to preferred particle orientations in specific domains of the reactor. To resolve the preferred particle orientation we calculate the particle orientation tensor $\mathbf{S}_i$ using the expression

$$\mathbf{S}_i = \begin{bmatrix} \langle u_x^2 \rangle & \langle u_x u_y \rangle & \langle u_x u_z \rangle \\ \langle u_y u_x \rangle & \left\langle u_y^2 \right\rangle & \langle u_y u_z \rangle \\ \langle u_z u_x \rangle & \langle u_z u_y \rangle & \langle u_z^2 \rangle \end{bmatrix}. \tag{2.21}$$

The diagonal components of this tensor can be used to determine the preferred alignment in the reactor. If the difference between the diagonal components is less than 0.1 i.e. $\left|\langle u_x^2 \rangle - \langle u_y^2 \rangle\right| < 0.1$, $\left|\langle u_x^2 \rangle - \langle u_z^2 \rangle\right| < 0.1$ and $\left|\langle u_y^2 \rangle - \langle u_z^2 \rangle\right| < 0.1$, the particle is considered to be randomly oriented. On the other hand, if one component is considerably larger than the other two components, we conclude that the particle is preferably aligned with the corresponding axis.

Figures 2.9, 2.10 and 2.11 show the preferred particle alignment in steady-state in the grid cells for different lift and torque force conditions respectively. We study the particle alignment in the grid cells on the x-z plane and for a cross section along the y-axis ($0.06\,\text{m} \leq y \leq 0.075\,\text{m}$). From Table 2.2 the number of grid cells along the x-axis and z-axis are $n_x^g = L_x/c_x = 10$ and $n_z^g = H_z/c_z = 66$ respectively. We have applied a colour scheme to differentiate cells with particular particle orientations with blue cells indicating a preferred alignment with the x-axis, green cells indicating a preferred alignment with the y-axis and red cells indicating a preferred alignment with the z-axis. Cyan cells represent domains where there is no preferred orientation such that particles are randomly orientated.

From Fig. 2.9 we observe that inclusion of the lift force with drag does not lead to large changes in the preferred orientation of particles near the base of the reactor i.e. up to $z = 15$. However, we note that the particle orientations tend to become more random in the central domains of the reactor. With increasing height, differences between the preferred orientations are negligible due to the low density of particles in these domains of the reactors. With the inclusion of torque (Fig. 2.10), we find a noticeable effect on particle orientation as we have already observed in Fig. 2.8. Rather than being predominantly aligned with the z-axis, the particles are now aligned either randomly or perpendicular to the z-axis i.e. aligned with the x-axis and y-axis. We also highlight a change in the alignment of particles next the boundaries in comparison to the inclusion of lift (Fig. 2.9). In the cases with lift, particles near the walls tends to be aligned with the z-axis, while for cases with torque the particles tend to align with the y-axis. In addition, hydrodynamic torque has a strong influence on particle orientation in the diluted domain of the reactor, in particular in the range $30 < z < 50$ where particles have a strong preferred horizontal orientation. This is indicative of the rotational effects of torque on the particles to align the particles perpendicular to the fluid flow. In the lowest section of the reactor ($z < 20$), particles retain a preferred vertical orientation even with the inclusion of hydrodynamic torque. Figure 2.11 shows the effect of combined lift and torque conditions on the spatial distribution of particles preferred orientation. Similar to Fig. 2.8, we do not see any large difference in particle orientations upon inclusion of lift with drag and hydrodynamic torque. The majority of particles tend to orient horizontally with particles in the lower section of the reactor having a preferred vertical orientation. Comparing Fig. 2.10 and 2.11 we highlight a slight difference in particle orientation in the central section of reactor between i.e. $15 < z < 30$, where particles have a preferred horizontal orientation. We also find a slight increase of particles vertically aligning adjacent to the walls, which is similar to the effect noted for cases with just drag and lift.

2.4.4. ANGULAR MOMENTUM

Figures 2.12, 2.13 and 2.14 show the temporally-averaged magnitude of the angular momentum at grid cells on the x-z plane averaged along the y-axis for different hydrodynamic force conditions. We notice that particles have the largest angular momentum in the freeboard or upper region of the bed where particle flow is quite dilute with the average particle occupancy $\langle n_p \rangle (z) < 2$ (Fig. 2.5). Comparing Figs. 2.12 and 2.13, we note that the inclusion of lift only leads to a considerable increase in angular momentum, while the inclusion of hydrodynamic torque only has almost no effect on particle rotation. In addition, use of the Zastawny *et al.* lift correlation leads to a much larger change

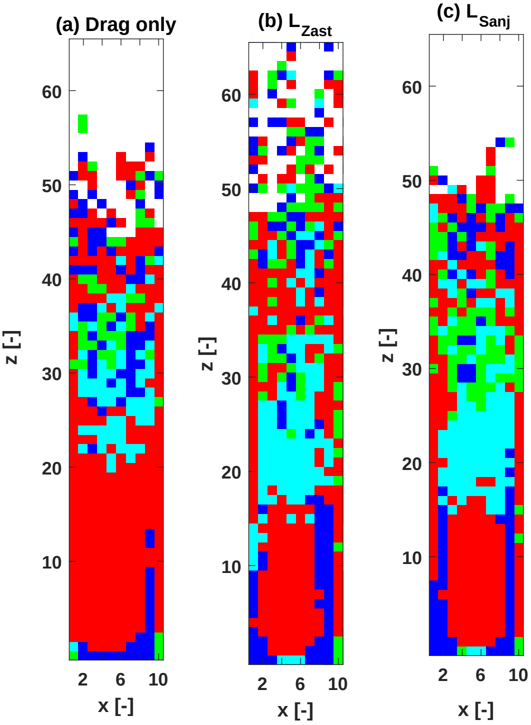

Figure 2.9: Preferred orientation of particles in the grid cells of the reactor for different cases of hydrodynamic force, with drag only and cases with lift force. (a) Drag only. (b) L_{Zast}. (c) L_{Sanj}. Here the colour scheme is: blue squares (🟦) are x-aligned, green squares (🟩) are y-aligned, red squares (🟥) are z-aligned and cyan squares (🟦) are randomly orientated. White space represents empty cells. The dimensions of the reactors on the xz-plane are $L_x \times H_z = 0.15\,\mathrm{m} \times 0.99\,\mathrm{m}$. In this plot, the dimensions are normalised by the grid cell size thus leading to $n_x^g = L_x/c_x = 10$ and $n_z^g = H_z/c_z = 66$.

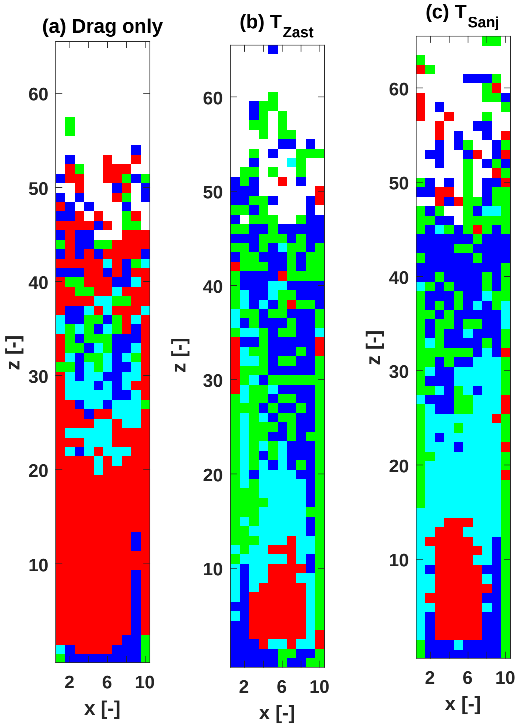

Figure 2.10: Preferred orientation of particles in the grid cells of the reactor for different cases of hydrodynamic force, with drag only and cases with hydrodynamic torque. (a) Drag only. (b) T_{Zast}. (c) T_{Sanj}. Details of the colour scheme are provided in the caption of Fig. 2.9.

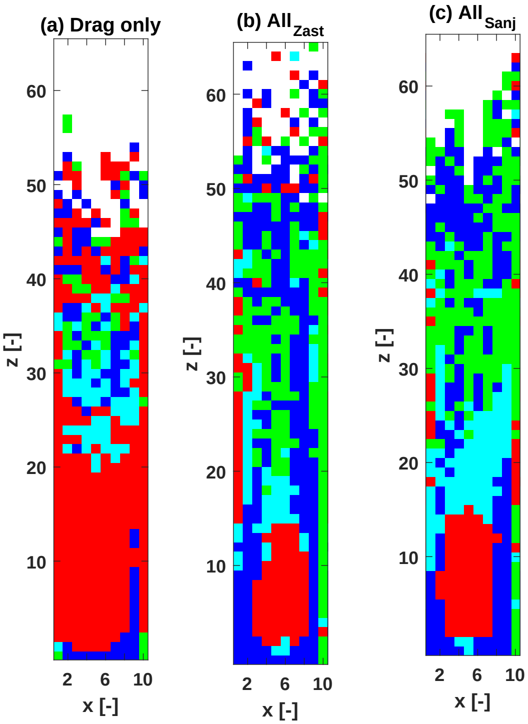

Figure 2.11: Preferred orientation of particles in the grid cells of the reactor for different cases of hydrodynamic force, with drag only and cases with all forces included. (a) Drag only. (b) All_{Zast}. (c) All_{Sanj}. Details of the colour scheme are provided in the caption of Fig. 2.9.

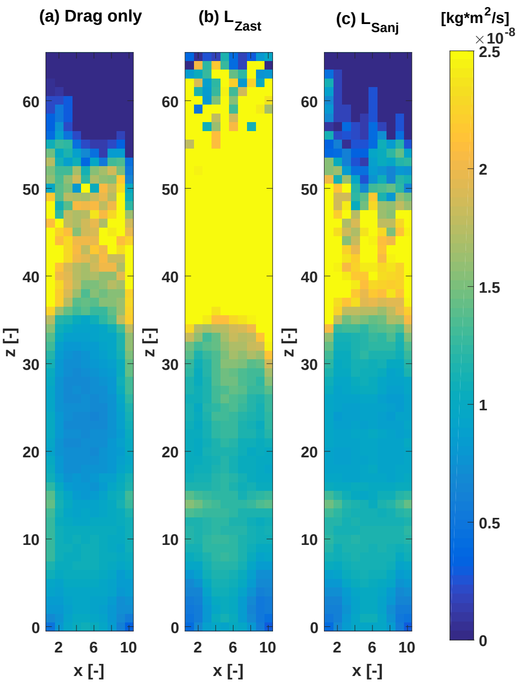

Figure 2.12: Angular momentum in x-z plane, temporally-averaged and averaged through y-direction for cases with (a) drag only and (b, c) drag and lift

in angular momentum in comparison to the results with the Sanjeevi *et al.* lift correlation. The greater influence of lift force on particle rotation can be attributed to the generation of larger torques by particle-particle and particle-wall interactions in contrast to hydrodynamic forces. As presented in Section 2.4.2, the inclusion of lift force leads to an increases in v_z, and consequently, more vigorous particle interactions, which results in larger variations in angular momentum. Including hydrodynamic torque has considerably less effect on particle rotation and it actually stabilises the particles, thus inhibiting free rotation, which is caused by the hydrodynamic torque always acting in the direction opposite to particle rotation. When all forces are included (Fig. 2.14), there is little difference with the case of drag and lift only (Fig. 2.12), which indicates that lift force has the dominant effect on particle rotation. From the comparison of Fig. 2.12 and Fig. 2.14 we conclude that the inclusion of hydrodynamic torque has a stabilising effect on particle rotation, hence lowering the total angular momentum.

2.5. DISCUSSION AND CONCLUSION

We have investigated via numerical simulations the effect of differing hydrodynamic force conditions on spherocylindrical particles (aspect ratio = 4) in dense gas-fluidised

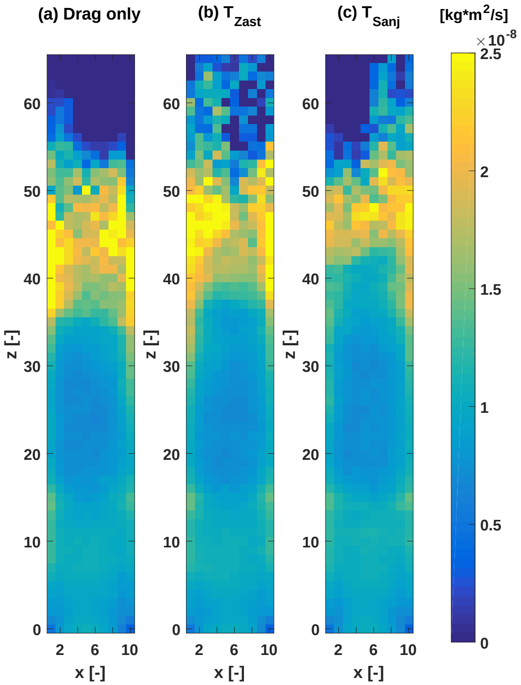

Figure 2.13: Angular momentum in x-z plane, temporally-averaged and averaged through y-direction for cases with (a) drag only and (b, c) drag and torque.

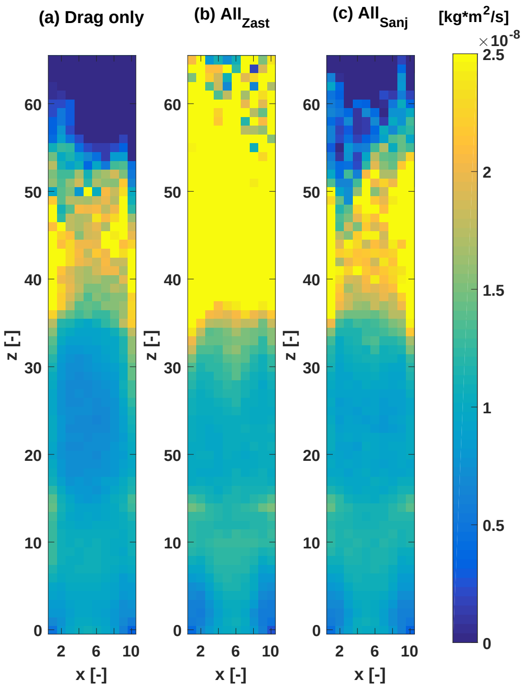

Figure 2.14: Angular momentum in x-z plane, temporally-averaged and averaged through y-direction for cases with (a) drag only and (b, c) all hydrodynamic forces included.

beds. To account for the coupling between the solid particle phase and fluid phase, we have employed the CFD-DEM algorithm where the CFD component solves the fluid motion and DEM solves the particle-particle interactions. In this study we have considered several different hydrodynamic force cases where particles are subject to varying lift and torque closures (Table 2.3). First, we have used lift and torque expressions from Zastawny *et al.* [2] that were derived for ellipsoids and disk-like particles. From in-house direct numerical simulations (DNS), fitting coefficients suitable for spherocylindrical particles in this study have been calculated for the expressions in [2]. Second, we have employed lift and torque expressions specifically for the spherocylindrical particles explored in this study from recent DNS simulations of Sanjeevi *et al.* [3]. While we account for multiparticle effects in the calculation of the drag force by using the Di Felice approximation [58], the correlation functions considered here for the estimation of the lift and torque have been derived for isolated single spherocylinder particles and thus are applied here as an approximation of lift and torque conditions in a dense fluidized bed.

While we have explored a number of hydrodynamic force cases, a key observation from the results is the relevance of hydrodynamic torque on particle dynamics, in particular on particle orientation. In Section 2.4.3, we examined the effect of differing hydrodynamic force conditions on particle orientation in respect to the fluid flow or z-axis over the entire reactor and in specific domains of the reactor. First, Fig. 2.8 revealed that inclusion of torque leads to a considerable change in particle orientations, with particles less likely to be orientated parallel to the flow and more likely to be orientated perpendicular to the flow. We confirmed this observation by studying preferred particle orientations for differing lift and torque conditions. Second, although the addition of lift only has a slight effect on particle orientation (Fig. 2.9), marked by an increase in random orientation of particles in the middle section of the reactor, the inclusion of torque leads to considerable changes in the particle orientations throughout the reactor (Fig. 2.10). We note that only particles near the flow inlet of the reactor show alignment with the direction of fluid flow for both lift force cases. This is more than likely due to the collation of contacting particles into groups that move as a single solid unit with the direction of fluid flow. Beyond this region the particles become randomly orientated after which the particles tend to align perpendicular to the direction of flow (Fig. 2.10). This conforms with the visualisations presented in Fig. 2.4 where during the start of release particles appear to be orientated perpendicular to the z-axis. Additionally, the inclusion of torque leads to a large decrease in particle alignment with the z-axis for particles adjacent to the boundaries. Without torque, the particles can rotate more freely, however with torque, the degree of particle rotation decreases such that particles tend to orient perpendicular to the fluid flow. We do not find an appreciable difference in particle angular momentum with or without hydrodynamic torque or lift (see Figs. 2.12, 2.13 and 2.14). This suggests that changes in particle angular momentum may be dominated by interparticle interactions.

We also examined the effect of varying hydrodynamic forces on particle velocity along the z-axis (v_z) at specific locations in the reactor (Fig. 2.7). For cases with just torque we find that there is little or no difference in the velocity profile in comparison to the case with drag forces only. However, inclusion of lift leads to a drastic change in the profile when compared with a case of just hydrodynamic torque, in particular midway along the x-axis. These results indicate that lift has a greater influence than hydrodynamic torque on particle velocity. However, while lift affects particle velocity, torque has a marked affect on particle orientation (Fig. 2.8). In combination, lift and torque conditions are of paramount importance for the interactions experienced by particles, and hence on the resulting flow conditions. We must also emphasise that both the lift and torque are calculated without consideration of multiparticle effects. Our previous study suggests that a multiparticle expression for lift force can have an even stronger effect on v_z profiles than using the single particle expression [60]. To comprehensively establish the precise effect of lift and torque in multiparticle setting requires new multiparticle expressions for the calculation of the lift and torque that could be derived from DNS simulations similar to those used to define the isolated lift and torque correlations [3].

While single-particle lift and torque correlations do not account for multiparticle effects and may lead to an overestimation of lift and torque in the dense or lower bulk domains of the reactor, particle dynamics in the upper domains of the reactor are argued to have greater accuracy. As shown in Fig. 2.5, temporally-averaged particle occupancy $\langle n_p \rangle$ in the upper domains of the reactor are significantly lower than in dense domains. For example, at $z = 0.0675\,\mathrm{m}$, which lies in the dense region of the reactor, $\langle n_p \rangle \approx 17$. However, at $z = 0.3075\,\mathrm{m}$, which lies in the dilute domain of the reactor, $\langle n_p \rangle \approx 5$. Hence, in the upper regions of the bed, on average, particles will be subject to lower multiparticle effects and thus lower deviations from the idealised single particle case. Thus, we surmise that the lift and torque conditions experienced by particles, and hence the ensuing dynamics in the upper regions of the bed can be suitably described using single-particle lift and torque correlations. Further studies on varying lift and torque conditions are necessary to corroborate this effect.

Domains near the base of the reactor are typified by long-lasting particle contacts and groups of interlocked or jammed particles. These groups will tend to move as single units and thus experience hydrodynamic conditions dictated by local multiparticle effects. Intuitively one would expect that the lift and torque on an individual particle in a group would be suppressed. The lift and torque correlations used in this study do not account for such complex multiparticle effects. Imperatively, we point out that this study is a preliminary investigation on the importance of lift and torque on fluidized spherocylinders. Once accurate and appropriate multiparticle lift and torque correlations become available, we will perform further simulations to explore particle dynamics and fully assess the limitations of single-particle lift and torque correlations for spherocylinders.

We have also not considered rotational torque, which develops due to the relative rotation of a particle with respect to the fluid. An expression for rotational torque has been defined in a previous study on ellipsoids and disk-like particles [2]. However, the coefficients are not applicable to the spherocylinders studied here. In addition, we deemed that rotational torque was not relevant for particle dynamics. Nonetheless, an accurate expression for spherocylindrical rotational torque could be calculated with DNS simulations for future CFD-DEM investigations.

In the case of the drag closure, with multiple-particle correlation expressions for spherocylinder particles unavailable, we account for the effect of neighbouring particles by adapting the expression of Di Felice (Eqs. 2.11 and 2.12). However, the Di Felice approximation has been derived for spherical particles [58] and is used here to approximate the neighbouring or swarm effect on the drag forces experienced by spherocylindrical particles. Previous studies on spherocylinder-like particles have also employed the Di Felice expression to account for multiple-particle effects [62–66]. While the Di Felice expression accounts for variations in the particle Reynolds number, it does not take into consideration the orientation of the particle of interest or the orientation of the neighbouring particles, given that it has been defined for perfect spheres. As a result, the expression may coarse grain key geometrical aspects of particle arrangements near a particle of interest and hence provide only a rough estimate of the true drag force. Compared to the spherical case, the change in drag force experienced by a spherocylinder due to the proximity of other spherocylinder particles may depend on the configuration of the neighbouring particles.

Experiments with pseudo-2D fluidised beds can be used for accurate particle image velocimetry (PIV) and particle tracking velocimetry (PTV) studies [7]. Unfortunately such experiments do not provide information in relation to particle dynamics in the bulk of a fluidised bed i.e. distant from the boundaries of the system.

To gain better insight into the fluidisation response in laboratory scale 3D fluidized beds, in the future, we plan to perform Magnetic Particle Tracking (MPT) experiments [67–69] where the magnetic field associated with a single magnetic tracer particle is measured using a magnetic sensor array. This approach has previously been used to track both spheres and rods in a cylindrical fluidised bed [68]. Data from future MPT experiments will be compared with current numerical results and also used to motivate further CFD-DEM investigations.

3

FLUIDIZATION OF SPHERICAL VERSUS ELONGATED PARTICLES - EXPERIMENTAL INVESTIGATION USING MAGNETIC PARTICLE TRACKING

In biomass processing fluidized beds are used to process granular materials where particles typically possess elongated shapes. However, for simplicity, in computer simulations particles are often considered spherical, even though elongated particles experience more complex particle-particle interactions as well as different hydrodynamic forces. The exact effect of these more complex interactions in dense fluidized suspensions is still not well understood. In this study we use the Magnetic Particle Tracking (MPT) technique to compare the fluidization behavior of spherical particles to that of elongated particles. We found a considerable difference between fluidization behavior of spherical versus elongated particles in the time-averaged particle velocity field as well as in the time-averaged particle rotational velocity profile. Moreover, we studied the effect of fluid velocity and the particle's aspect ratio on the particle's preferred orientation in different parts of the bed, which provides new insight in the fluidization behavior of elongated particles.

Part of this chapter has been published in AIChE Journal **66** (2019) [70].

3.1. INTRODUCTION

Fluidized beds are encountered in many industrial applications such as gasification, drying, coating, food processing and gas phase polymerization. In many of these processes the fluidized particles have a non-spherical shape. This is particularly the case in biomass processing which is rapidly gaining importance because of the need to switch to more sustainable energy and material sources. Biomass such as wood chips, wood pellets and straw-like materials are characterized by an elongated shape. Elongated particles feature much more complex particle-particle interactions as well as complex hydrodynamic forces that depend on particle shape and orientation to the flow. This creates a need for better understanding of fluidization of elongated particles which explains why such systems have received considerable attention in recent years. Fluidization of elongated particles such as cylinders, ellipsoids and spherocylinders has been the topic of several numerical investigations [7, 8, 71–73]. More fundamental research has also been conducted to obtain a better understanding of the hydrodynamic forces acting on individual elongated particles [2, 3, 32, 74].

Experimental investigations for validation of computational models for dense gas-particle flows are still quite scarce, especially for 3D systems. The best established and mostly used non-invasive technique is PIV-DIA [75], but it is limited to quasi-2D systems. The first experimental research on fluidization of non-spherical particles was carried out using this technique [7, 63, 76]. For 3D systems, X-ray tomography (XRT) has been widely used for fluidized beds with spherical particles [77–80]. For most particle sizes, this technique can only provide insight in the bubble behavior of fluidized beds and unfortunately no information on the particle orientation, which is an important parameter for non-spherical particles. The latter requires particle tracking techniques. Recently, X-ray particle tracking velocimetry was used to investigate binary fluidized beds with cylindrical particles [81, 82]. X-ray rheography is a novel technique that can be used to obtain velocity fields for 3D granular systems [83, 84]. Positron emission particle tracking (PEPT) is another established particle tracking technique [85, 86], which has also been successfully used to track the orientation of non-spherical particles [87].

The disadvantage of employing techniques like XRT and PEPT is that they require special facilities and safety measures. Therefore, the application of these techniques is challenging. Magnetic particle tracking (MPT) [67–69, 88–91] has emerged as a novel experimental technique that has proven to be less expensive and safer than XRT and PEPT. MPT relies on following a magnetic dipole of a single tracer particle which allows tracking of the particle position, together with its orientation.

In this work we use the Magnetic Particle Tracking (MPT) technique to investigate the fluidization behavior of elongated particles. In particular, we will investigate spherocylinders of different aspect ratio, representative of biomass particles. We compare the fluidization behaviour of spherocylindrical particles of two aspect ratios: aspect ratio 4 (AR-4) and aspect ratio 6 (AR-6), with that of spherical particles (AR-1), for several superficial gas velocities.

3.2. MAGNETIC PARTICLE TRACKING (MPT)

The principles behind magnetic particle tracking technique are thoroughly discussed in [67]. Here we only present a short summary. MPT is an experimental technique which relies on tracking a single magnetic marker. The magnetic tracer particle generates a quasi-static magnetic field, given by:

$$\mathbf{H}(\mathbf{u}_p, \mathbf{r}_{ps}) = \frac{1}{4\pi}\left(-\frac{\mu_m \mathbf{u}_p}{|\mathbf{r}_{ps}|^3} + \frac{3\mu_m(\mathbf{u}_p \cdot \mathbf{r}_{ps})\mathbf{r}_{ps}}{|\mathbf{r}_{ps}|^5}\right) \tag{3.1}$$

where $\mathbf{r}_{ps} = \mathbf{r}_p - \mathbf{r}_s$ is the relative position vector between the tracer particle and the sensor, μ_m is the magnetic moment of the tracer particle, and $\mathbf{u}_p$ is its unit orientation vector. The magnetic field generated by the tracer particle is detected by employing multiple Anisotropic Magneto Resistive (AMR) sensors. The tracer particle position and orientation is estimated by minimizing the difference between the theoretical and measured magnetic field strength of all sensors. The theoretical magnetic field strength is calculated for each sensor based on its position and orientation by multiplying Eq. 3.1 with the orientation vector of the sensor

$$S_t = \mathbf{H}(\bar{e}_p, \mathbf{r}_{ps}) \cdot \mathbf{e}_s \tag{3.2}$$

Subsequently, the difference between the theoretical field strength and sensor data is minimized using Eq. 3.3:

$$P = \frac{\sum_{i=1}^{N} \mathrm{erf}\left(\frac{S_{t,i} - S_{m,i}}{\sqrt{2}\sigma_i}\right)}{N} \tag{3.3}$$

where N is the number of sensors, Sequential Quadratic Programming is used to solve the associated minimization problem.

The experimental error in determining the magnetic tracer position and orientation depends on magnetic moment of the magnet. For the tracer with a magnetic moment of 0.014 Am^2 used in this work, the uncertainty in determining its position and orientation is of the order of 2 mm and 2 degree, respectively. More information about determination of uncertainty can be found in [88]

3.3. EXPERIMENTAL SETUP

The experimental setup used in this work is shown in Fig. 3.1. A square gas-fluidized bed is surrounded by a 3D sensor array that consists of four rings, each carrying six tri-axis AMR sensors. Setup and control are provided by Matesy GmbH. Each tri-axis sensor measures the magnetic field in 3 orthogonal directions, resulting in a total of 72 signals coming from the whole sensor array. The fluidized bed and sensor array are positioned in the center of a large Helmholtz coil to counter the effect of the earth's magnetic field. The fluidizing gas is air, the source of which is connected to a humidifier to minimize generation of static charge during fluidization. Because in these experiments we

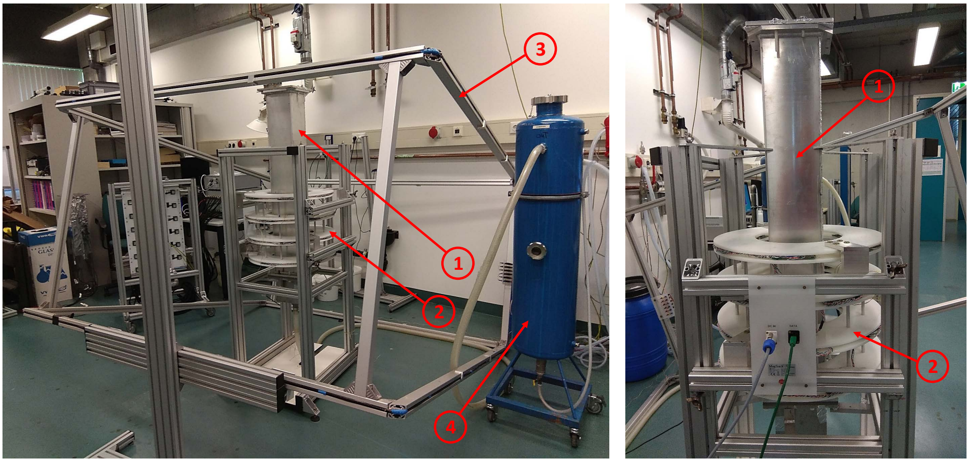

(a) (b)

Figure 3.1: (a) Full experimental setup, (b) close-up of the column with sensor array. 1-Fluidized bed, 2-Sensor array, 3-Helmholtz coil, 4-Humidifier.

are using relatively large granular particles, not powders, using moist air for fluidization will not lead to sticking agglomerate formation. All equipment parts consist of non-magnetizable materials. The dimensions and properties of the experimental setup are listed in Table 3.1.

In this study three types of particles are investigated, with different aspect ratios (L/D = 1, 4 and 6), shown in Fig. 3.2 . Particles of aspect ratio 1 (AR-1) and 4 (AR-4) are volume equivalent to each other, while particles with aspect ratio 6 (AR-6) have the same diameter as AR-4 but differ in length. The minimum diameter of the particles is limited by the need to insert a magnet inside the tracer particle. The particles are 3D printed and made of alumide, a 3D printing material consisting of nylon filled with aluminum dust. The advantage of using this material (over more commonly used plastics) is that it allows, through particle contacts, for electrically conductive paths to the aluminum bed walls, thus preventing slow buildup of static charge during the experiments. In all experiments the mass of the bed is kept the same at 3.3 kg. For this mass of the bed, the initial bed heights for our particles are 17.5 cm, 17.9 cm and 18.5 cm for AR-1, AR-4 and AR-6 particles respectively. Tracer particles for aspect ratios 4 and 6 are made of European lime wood, with a density of 548 kg/m^3, and have the same shape and size as the bulk particles. The wooden particle is drilled along its long axis and in the middle of the particle a cylindrical neodymium magnet is inserted. The spherical tracer particle is made in a similar way: a cork sphere with a density of 240 kg/m^3 and 5.3 mm diameter is drilled from side to side and in the middle a spherical magnet with 3 mm diameter is positioned. The drilled holes are closed and filled with silicone. Inserting a magnet inside the tracer particle will change its moment of inertia which has to be taken into account when the presented results are used for validation of numerical models. The dimension and properties of the particles, tracer particles and magnets used are listed in Table 3.2 . The overall tracer particle density closely matches the density of the bulk particles. In

Fluidized bed

Parameter	Value
Width	0.15 m
Depth	0.15 m
Height	1 m
Column material	Aluminum

MPT sensor array

Parameter	Value
Sensor type	Tri-axis AMR
Number of sensors	24
Height	0.45 m
Distance between opposing sensors	0.26 m
Frequency	1000 Hz

Table 3.1: Dimensions and properties of the experimental setup.

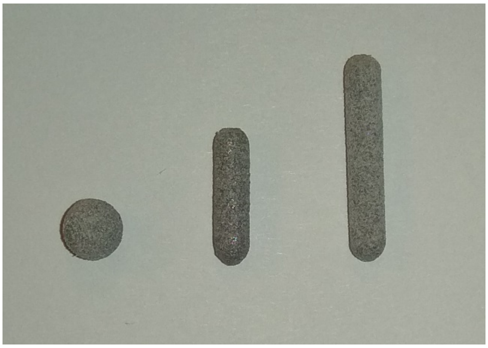

Figure 3.2: 3D printed alumide particles of aspect ratio AR-1, AR-4 and AR-6.

case of aspect ratio 6 particles, the density of the tracer particle and bulk particle is identical. However, a difference in density between the tracer particle and the bulk particles for AR-1 particles is 25 % and for AR-4 particles 31 %. Due to the higher density of the tracer particle, it can spend a longer time at the bottom of the column and will not be lifted as high in the freeboard region as the other particles. This difference in density does not present a problem because in dense fluidizing conditions, the tracer particle will move with the rest of the bulk particles and there will be no segregation [67, 92]. The only regions where caution should be taken for interpreting the results are the freeboard region and the lower part of the bed, close to the distributor plate.

3.4. RESULTS

In this section we present and compare the fluidization characteristics for spherocylindrical particles of three different aspect ratios (aspect ratio 1, 4 and 6). The particles of aspect ratio 1 and 4 were fluidized using 4 different gas velocities, at $1.4U_{mf}$, $1.6U_{mf}$, $1.8U_{mf}$

Particles

Parameter	AR-1	AR-4	AR-6
Number of particles	30000	30000	17750
Particle length [L]	-	12 mm	18 mm
Particle diameter [2R]	5.3 mm	3 mm	3 mm
Particle material	Alumide	Alumide	Alumide
Particle density	1442 kg/m^3	1442 kg/m^3	1442 kg/m^3
Mass of particle	0.112 g	0.112 g	0.186 g
Bed height	18 cm	18.4 cm	19.2 cm
Minimum fluidization velocity	1.58 m/s	1.7 m/s	2.64 m/s
Magnet			
Material	N52 (NdFeB)	N52 (NdFeB)	N52 (NdFeB)
Length	-	7.00 mm	12 mm
Diameter	3 mm	1.6 mm	1.2 mm
Density	7200 kg/m^3	7200 kg/m^3	7200 kg/m^3
Magnetic moment	0.14 Am^2	0.14 Am^2	0.14 Am^2
Tracer particle			
Particle length [L]	-	12 mm	18 mm
Particle diameter [2R]	5.30 mm	3 mm	3 mm
Particle material	Cork	European lime	European lime
Particle density (without magnet)	240 kg/m^3	548 kg/m^3	548 kg/m^3
Particle density (with magnet)	1796 kg/m^3	2057 kg/m^3	1498 kg/m^3
Mass of particle (with magnet)	0.14 g	0.16 g	0.18 g

Table 3.2: Particle properties.

and $2U_{mf}$, while the particles of aspect ratio 6 were fluidized only at 1.4 and $1.6U_{mf}$ due to limitations of the air supply. All experiments were run for three hours to obtain good statistical averages. We present our results in terms of the particle velocity in the vertical (z) direction, particle orientation and particle rotation velocity.

3.4.1. MINIMUM FLUIDIZATION VELOCITY

The minimum fluidization velocity U_{mf} for the particles was obtained from pressure drop measurements as described in [6, 7] by intersection of the packed bed pressure drop line and the fluidized bed static pressure drop at decreasing flow rate. The pressure drop measurements were carried out using a MPX5050DP differential pressure sensor attached to the bottom of the column. The air flow rate was incremented in steps of 10 nm^3/h, and for each value measurements were taken for 60 seconds at 100 Hz for both increasing and decreasing flow rate. The pressure drop curves for the 3 types of particles are presented in Figure 3.3 . When determining the minimum fluidization velocity for elongated particles we need to be careful because of the additional fluidization regimes that appear in the fluidization of such particles. When fluidizing elongated particles there is no direct transition from a fixed bed to a fluidized bed, but rather there are two channeling phases (active and passive channeling), described in [7], before the bed reaches the bubbling fluidizing regime. For long particles, with aspect ratio 6, the transition from a fixed bed to passive channeling is clearly noticeable in the pressure drop curve at a gas velocity of 2 m/s. The channels formed in the bed of AR-6 particles are more stable than in beds of lower aspect ratio particles, which makes it harder for them to transition to bubbling fluidization. The determined minimum fluidization velocities are listed in Table 3.2.

3.4.2. PARTICLE VELOCITY

Figures 3.4, 3.5 and 3.6 show the velocity distributions in the x-z plane for particles of aspect ratio 1, 4 and 6, respectively. The data were averaged in the y-direction and weighted by the number of particles in each cell of 1x1 cm used for averaging. From Figure 3.4 it can be seen that spherical particles tend to rise in the middle of the column and fall down next to the walls. However, at low gas inlet velocities ($1.4U_{mf}$ and $1.6U_{mf}$) two counter-rotating vortices can be noticed, one below 7 cm height, where particles rise next to the wall and move towards the center of the bed, and another one above 7 cm where particles rise in the center of the column. Increasing the gas inlet velocity reduces the size of these lower vortices until they completely disappear leaving only the upper vortex as the dominant one, which in our case for spheres can already be observed at $1.8U_{mf}$. This behavior is well-known and reported in the literature [6, 93], and can be explained by motion of small bubbles near the walls that tend to move away from the walls due to coalescence with neighboring bubbles. As bubble motion is the main driver of particles movement in the fluidized bed, a shift of bubble activity towards the center of the column will cause particles to rise in the middle and descend in the vicinity of the walls. With increasing gas inlet velocity, more bubbles will form above the distributor plate and their size will be larger, which leads to faster coalescence. Therefore, increasing the gas inlet velocity decreases the size of the lower vortex until it completely disappears.

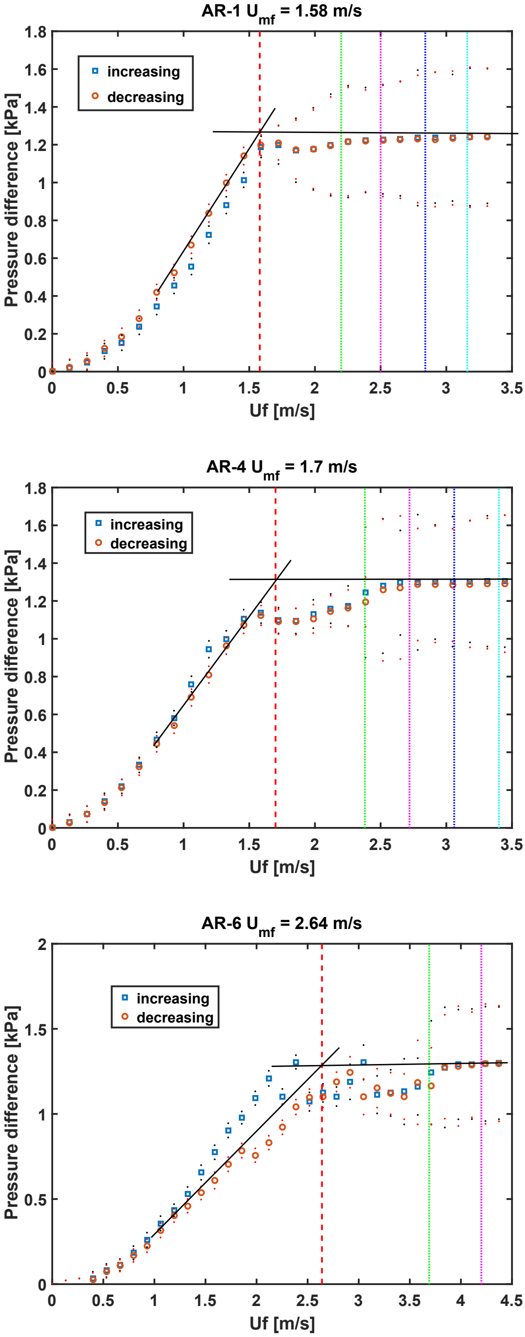

Figure 3.3: Pressure drop measurements and minimum fluidization velocity determination for AR-1, AR-4 and AR-6 particles. The dashed red line represents the determined minimum fluidization velocity, the dotted lines indicates the used fluidization velocities: green $1.4U_{mf}$, purple $1.6U_{mf}$, blue $1.8U_{mf}$ and cyan $2U_{mf}$.

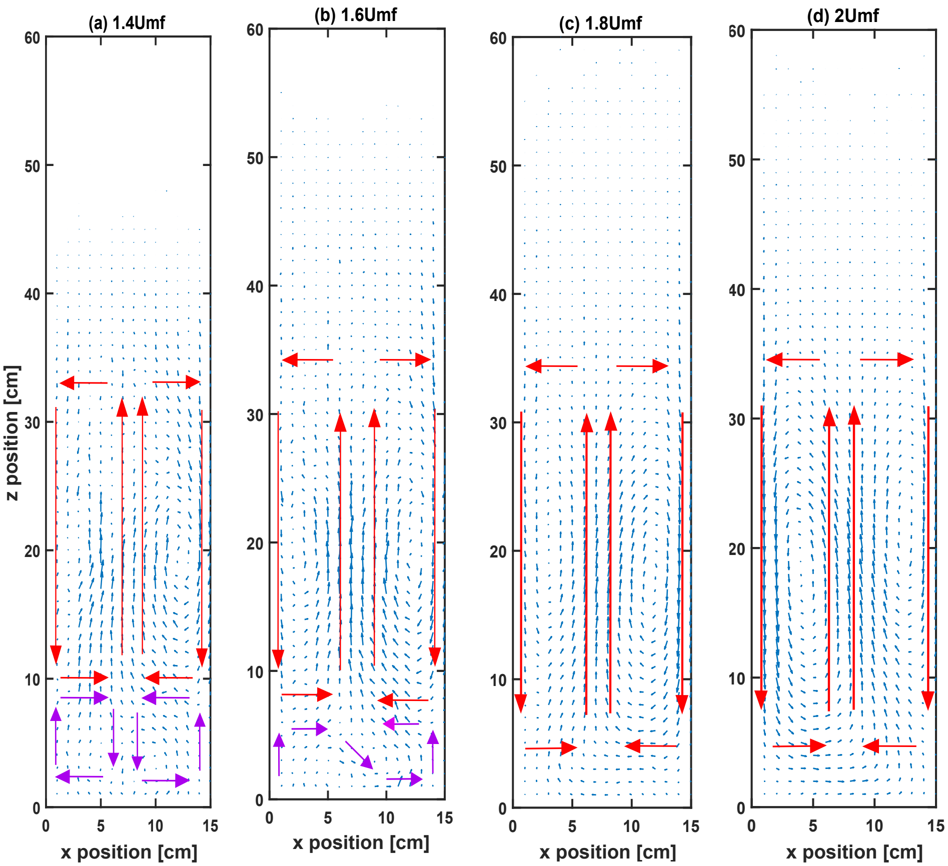

Figure 3.4: Velocity distributions for AR-1 particles in the X-Z plane for different gas inlet velocities. Positions are indicated in cm. Red and purple arrows indicate the directions of the main vortices.

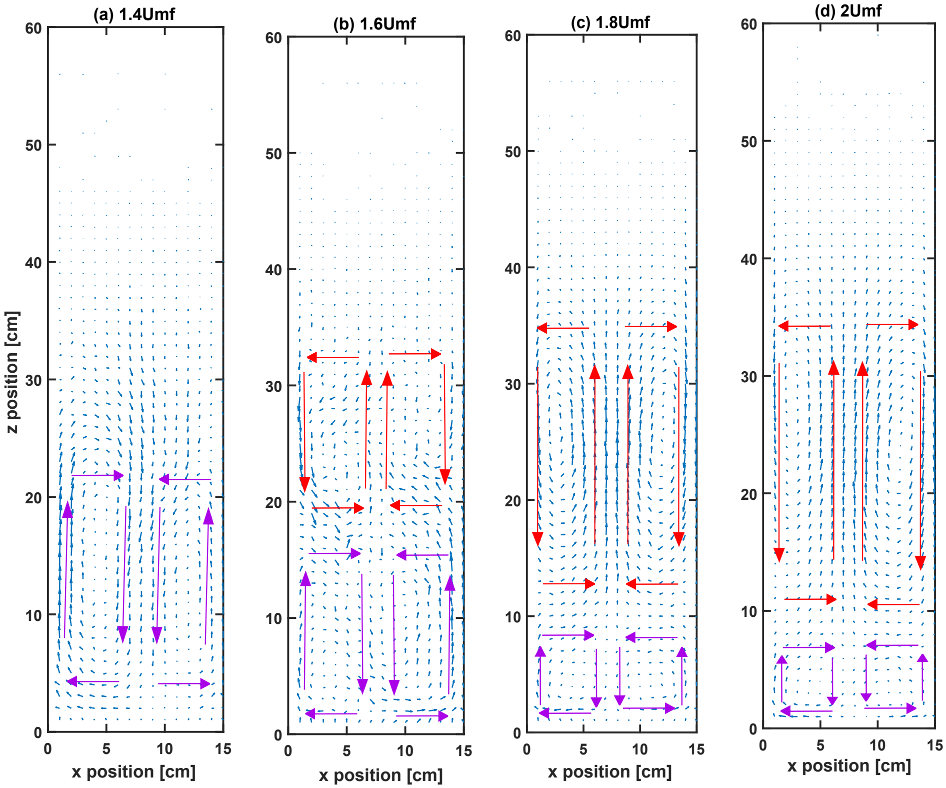

Figure 3.5: Velocity distributions for the AR-4 particles in X-Z plane for different gas inlet velocities. Positions are indicated in cm. Red and purple arrows indicate the directions of the main vortices.

Comparing the velocity profiles of spherocylindircal particles, shown in Figures 3.5 and 3.6, to the above discussed spherical particles it can be noticed that they show substantially different circulation patterns. At a low gas inlet velocity of $1.4U_{mf}$, spherocylindrical particles show only one vortex and, unlike the spheres, they rise next to the walls and descend in the middle of the column. This behavior is not discernible during the fluidization of spherical particles and agrees with the observations reported in [68]. An increase of gas velocity to $1.6U_{mf}$ leads to the separation of the flow and a double circulation pattern emerges such that the lower and upper vortex are roughly the same size. A further increase of the gas inlet velocity leads to a decreases of the size of the lower vortex, but it remains present even at the highest gas velocity that we considered. Spherocylindrical particles clearly show more distinct double circulation patterns, with considerably larger lower vortices than spherical particles.

The specific circulation pattern of spherocylindrical particles can be explained to be a consequence of the stronger packing of spherocylinders compared to spheres. Entanglement and higher contact surface between the particles makes it harder for bubbles to move through such a strong packing of entangled particles compared to propagation

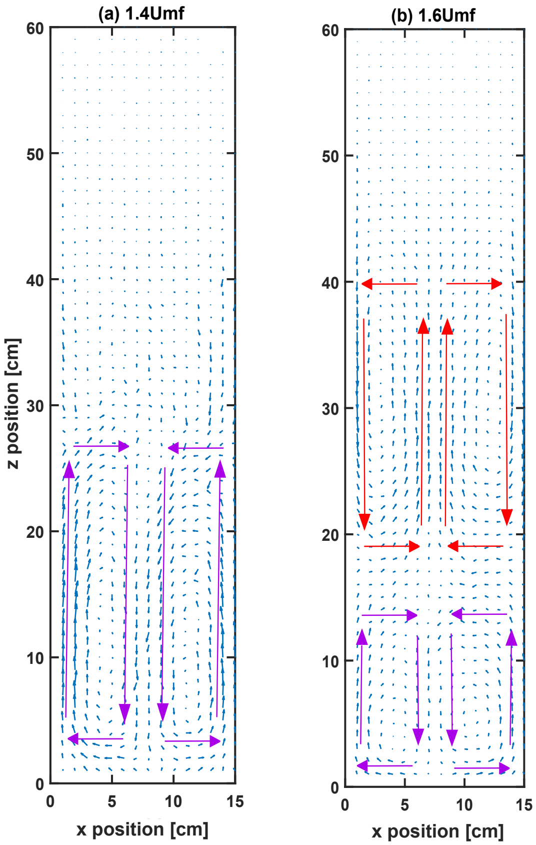

Figure 3.6: Velocity distributions for AR-6 particles in the X-Z plane for different gas inlet velocities. Positions are indicated in cm. Red and purple arrows indicate the directions of the main vortices.

through the space between particles and walls. Therefore, at low inlet gas velocity, particles will be lifted next to the walls and descend in the middle of the column. Stronger packing also makes it harder for bubbles to coalescence and move towards the central region of the column, leading to a larger and more stable lower vortex.

3.4.3. PARTICLE ROTATIONAL VELOCITY

The Magnetic Particle tracking technique allows us to track the components of the rotational velocity perpendicular to the magnetic axis, which in case of our tracer particles is aligned with the particle main axis. Figures 3.7 and 3.8 show profiles of the magnitude of the particle rotational velocity in the x-z plane, averaged along the y-axis, for particles of aspect ratio 4 and 6, respectively. From both figures it can be observed that AR-4 and AR-6 particles have the highest rotational velocities in the free board region. From these figures it can also be seen that an increase in gas velocity leads to an increase in particle rotational velocity in the entire bed. Comparing figures 3.7 and 3.8, it can be observed that particles with aspect ratio 6 have much higher rotational velocities than aspect ratio 4 particles.

From Figure 3.9 it can be seen that, unlike spherocylinders, for spherical particles, the highest rotational velocities are not encountered in the freeboard region but in the vicinity of the walls (Figure 3.9 (a) and (b)). With increasing gas velocity, the particle rotational velocity in the bulk region of the bed also increases.

The occurrence of high rotational velocities next to the walls in case of spherical particles can be associated with rolling of particles along the wall, caused by tangential particle-wall friction. In contrast, rolling of spherocylindrical particles along the wall around an axis parallel to the wall, but perpendicular to the particles long axis is nearly impossible because of the elongated shape. There exists a possibility that spherocylinders do roll along the long particle axis, but this mode of rotation is not detectable with our current MPT system.

Even though the tracer particles have the same size and shape as the rest of the bulk particles, this is not the case for the moment of inertia, because of the inserted magnet. This needs to be taken into consideration when the presented experimental data is used to validate numerical models.

3.4.4. PARTICLE ORIENTATION

Unlike spherical particles, non-spherical particles can possess different orientation relative to direction of the fluid flow. This is an important characteristic of non-spherical particles, because orientation of the particles relative to the fluid flow affects the magnitude of the drag force they experience and also increases the importance of shape induced lift force and hydrodynamic torque [32][3][8]. Figure 3.10 shows the effect of changing the gas velocity on particle orientation relative to the z-axis. To avoid the effect of the slightly higher tracer density, discussed in section 3.3 , the free-board region and lower part of the bed, close to the distributor plate, are excluded from the averaging. We therefore focus on the bulk region between 10 cm and 35 cm height. For particles in a fluidized bed, the orientation with respect to the main direction of gas flow is important.

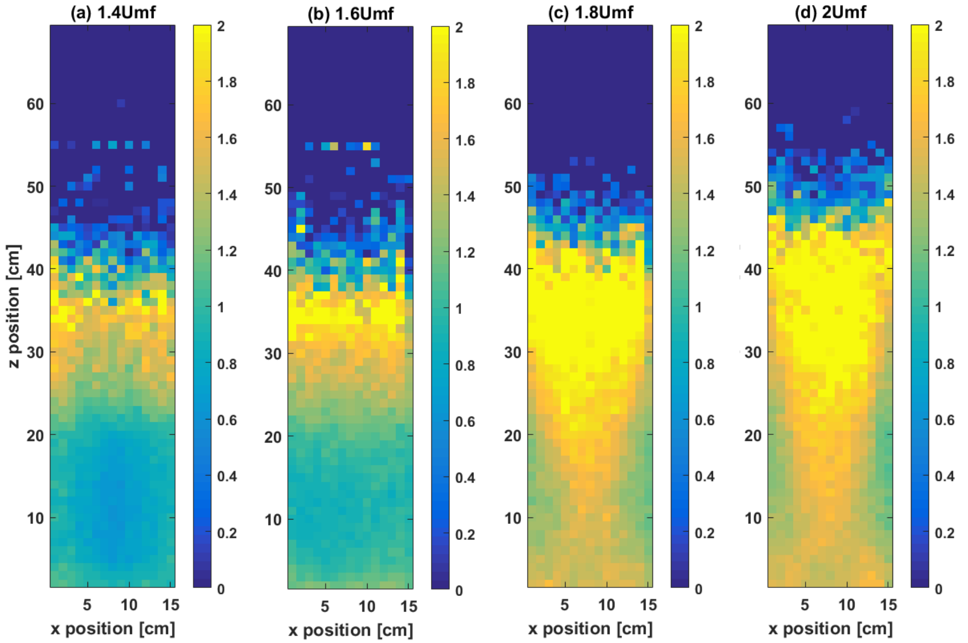

Figure 3.7: Rotational velocity [rot/s] distributions, for rotations around axes perpendicular to the long axis of the particle, in the x-z plane for AR-4 particles.

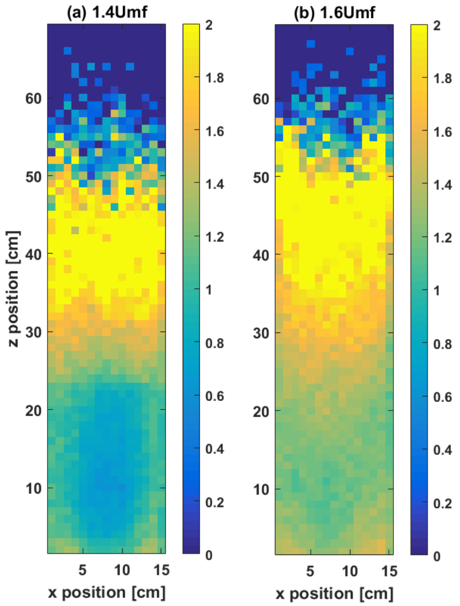

Figure 3.8: Rotational velocity [rot/s] distributions, for rotations around axes perpendicular to the long axis of the particle, in the x-z plane for AR-6 particles.

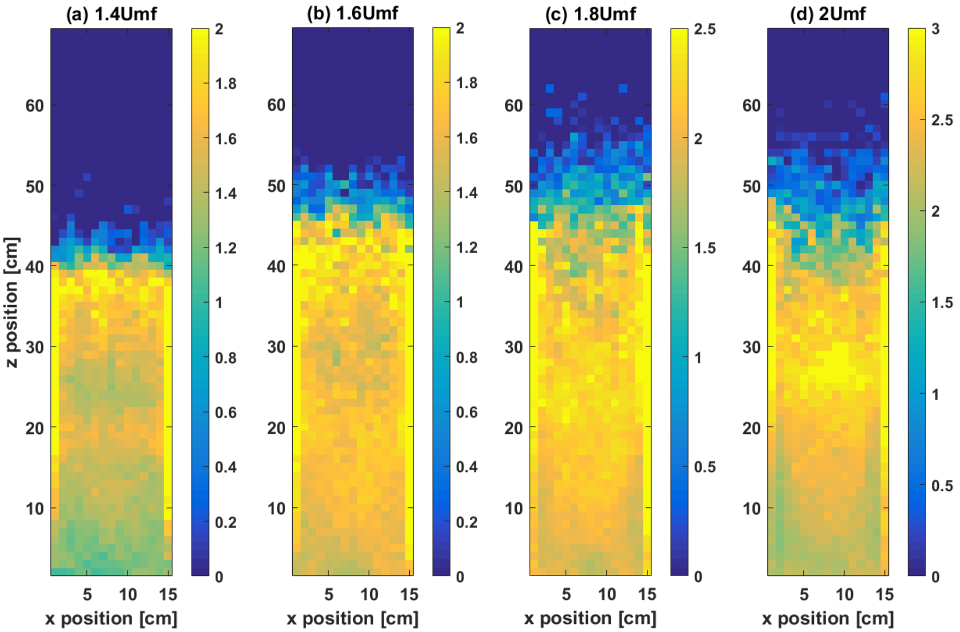

Figure 3.9: Rotational velocity [rot/s] distributions in the x-z plane for AR-1 particles.

Therefore we focus on the z-component of the particle orientation vector u_z , which can provide information on the particles alignment: for $u_z = \pm 1$ the particle is fully aligned with the main flow, while for $u_z = 0$ the particle is perpendicular to the main flow direction.

Figure 3.10 shows that with increasing gas velocity, the fraction of particles oriented vertically increases while the fraction of particles that orient horizontally decreases. At a low gas velocity of $1.4U_{mf}$ for both aspect ratio particles there exists a peak for horizontal orientation of particles, which disappears with increasing gas velocity. Figure 3.11 compares the z-orientation distribution of AR-4 and AR-6 particles at two different gas velocities. At a gas velocity of $1.4U_{mf}$ in both cases we observe a clear peak for horizontal orientation. However while the majority of AR-4 particles at this velocity tend to orient horizontally in case of AR-6 particles there is also a strong preference for vertical orientation. At a superficial velocity of $1.6U_{mf}$ in both cases an increase in fraction of particles oriented vertically can be observed but the stronger preference of AR-6 particles for vertical orientation is still evident.

While Figures 3.10 and 3.11 give insight into the average orientation of particles with respect to the z-axis, Figures 3.12 and 3.13 display the preferred orientation of particles in different parts of the reactor. The particle preferred orientation can be measured using the nematic tensor **S** defined as:

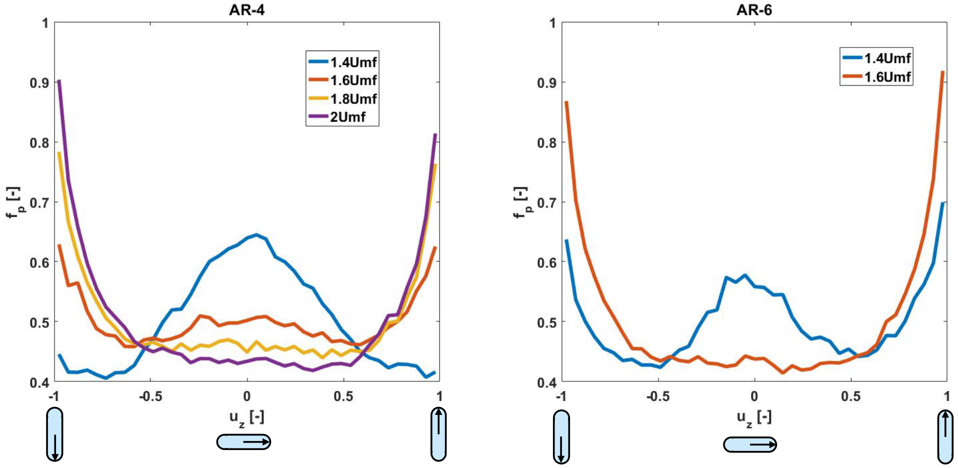

Figure 3.10: Effect of gas velocity on the time-averaged fraction (f_p) of particle orientation in the z-direction (u_z) of AR-4 and AR-6 particles.

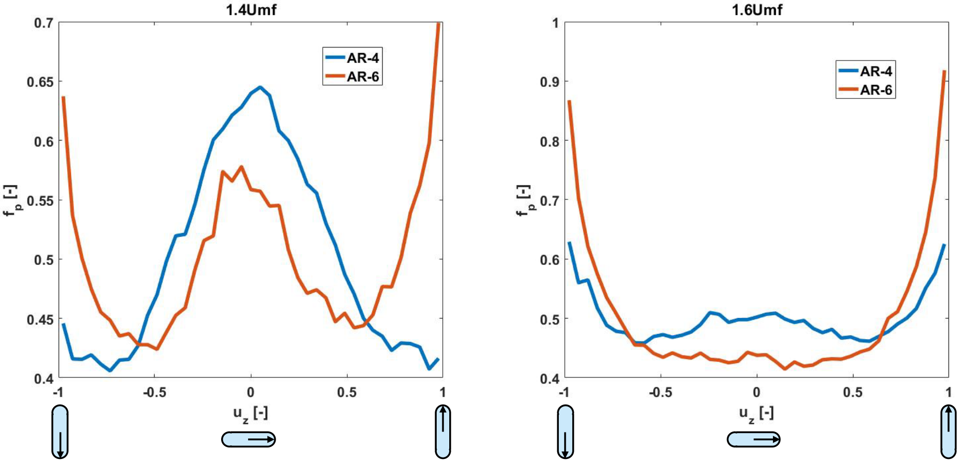

Figure 3.11: Comparison of time-averaged particle orientation in the z-direction for AR-4 and AR-6 particles.

$$\mathbf{S} = \begin{bmatrix} \langle u_x^2 \rangle & \langle u_x u_y \rangle & \langle u_x u_z \rangle \\ \langle u_y u_x \rangle & \langle u_y^2 \rangle & \langle u_y u_z \rangle \\ \langle u_z u_x \rangle & \langle u_z u_y \rangle & \langle u_z^2 \rangle \end{bmatrix}. \tag{3.4}$$

Values of the diagonal components of the orientation tensor indicate preferred alignment of particles with one of the Cartesian axes. If one of the components is considerably larger than others, it can be concluded that the particle is preferably aligned with that corresponding axis. Otherwise, if the difference between the diagonal components is less than 0.1 i.e. $\left|\langle u_x^2\rangle - \langle u_y^2\rangle\right| < 0.1$, $\left|\langle u_x^2\rangle - \langle u_z^2\rangle\right| < 0.1$ and $\left|\langle u_y^2\rangle - \langle u_z^2\rangle\right| < 0.1$, the particle is considered to be randomly oriented.

Figures 3.12 and 3.13 reveal the predominant particle alignment in different parts of the bed in the x-z plane for different inlet gas velocities. Values are temporally averaged and averaged over the y-direction. The coding color scheme is such that blue cells indicate preferred orientation of particles in the x-direction, green cells indicate preferred alignment with the y-direction and red cells indicate alignment with the z-axis. Cyan cells indicate random orientation of the particles.

From Figure 3.12 (a) it can be seen that at 1.4$\mathrm{U_{mf}}$ particles in the entire bed feature either horizontal or random orientation. In the lower part of the fluidized bed (below 10 cm), as well as in the central section and in the vicinity of the walls, particles assume a horizontal orientation such that in the middle they align with the x-axis but next to the walls they align with the y-axis. The horizontal orientation of the particles observed in the bulk region at the lowest fluidization velocity is due to the very mild fluidization at this velocity and less randomizing particle-particle collisions, therefore the features are still close to that in a non-fluidized packed bed. In the freeboard region, and in the parts between the middle section and walls, particles are randomly oriented. In Figure 3.12 (b), for $u_f = 1.6\mathrm{U_{mf}}$, an increase in random orientation of particles can be observed. In the lower part, close to the distributor plate, particles still have a preferably horizontal alignment, as well as in the lower free-board region, between 30 cm and 40 cm height. The horizontal orientation of the particles in the lower free-board region is the consequence of hydrodynamic torque [8]. In this region, particles move more-or-less individually and without the perturbing influence of neighboring particles they tend to orient horizontally in a planar upwards flow due to the stabilizing effect of hydrodynamic torque. Next to the walls, particles still tend to align with the y-axis but an increase of alignment with the z-axis can also be seen in that region. A further increase of the gas velocity, see Figure 3.12 (c) and (d), leads to an increase in vertical orientation, particularly in the middle of the dense region of the fluidized bed, between 10 cm and 20 cm height and next to the walls. At the same time, we notice a stronger preference in the lower freeboard region, between 30 cm and 40 cm height, for particles to orient horizontally.

Similar trends can be observed for AR-6 particles, as shown in Figure 3.13. An increase of fluid velocity reduces the tendency of particles to orient horizontally and increases the preference for vertical orientation. Comparing Figures 3.12 and 3.13 (a) and (b) reveals that AR-6 particles show stronger preference to orient vertically compared to AR-4 particles. This was already concluded from Figure 3.11, but from Figures 3.12 and

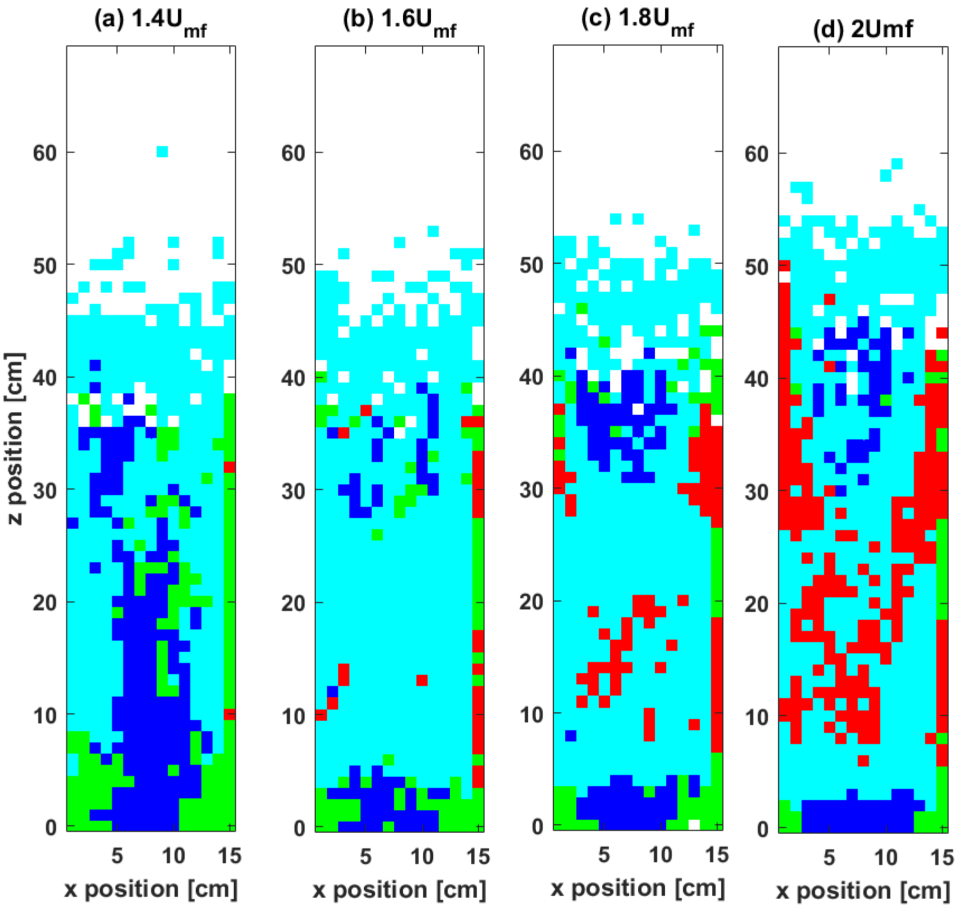

Figure 3.12: Distribution of the predominant orientation of AR-4 particles in the x-z plane. Here the colour scheme is: blue squares (🟦) are *x*-aligned, green squares (🟩) are *y*-aligned, red squares (🟥) are *z*-aligned, and cyan squares (🟦) are randomly oriented. White space represents empty cells. Schematic representation of color scheme is shown in Figure 3.13

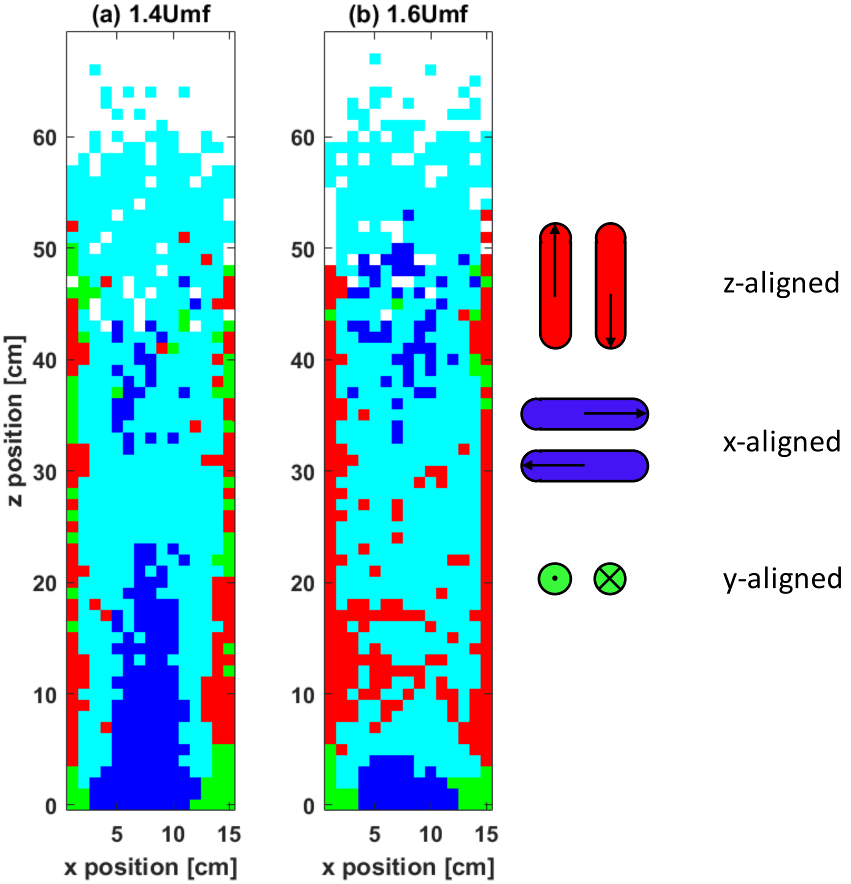

Figure 3.13: AR-6 particle prefered orientation in x-z plane. Here the colour scheme is: blue squares (🟦) are *x*-aligned, green squares (🟩) are *y*-aligned, red squares (🟥) are *z*-aligned and cyan squares (🟦) are randomly orientated. White space represents empty cells.

3.13 it becomes apparent that the stronger preference of AR-6 particles to orient vertically is mostly occurring next to the walls.

3.5. Discussion and conclusion

In this work, we applied Magnetic Particle Tracking (MPT) to compare the fluidization behavior of spherical and elongated particles at different gas velocities. We studied three types of particles: spheres and spherocylinders with aspect ratio 4 and 6. The MPT technique provides us detailed insight into particles translation and rotation as well as particle orientation in a full 3D gas-fluidized bed.

Regarding the particle preferred orientation, we observed a higher tendency for AR-6 particles to align with the gas flow than AR-4 particles. This is particularly the case in the wall region where in both cases particles align to the walls but AR-6 particles are also preferably aligned with the direction of gas flow, while AR-4 particles are perpendicular to it. Using the MPT results we have also mapped out different zones in our gas-fluidized bed based on the particles preferred orientation, as shown in Figures 3.12 and 3.13. In all considered cases, the particles assume a horizontal position in the lower part of the bed, close to the distributor plate. In the wall region, particles tend to align with the walls, where at low gas velocities they are lying in a horizontal position but with increase in gas velocity they align with the flow and assume a vertical position. The bulk region of dense particle flow is defined between 10 cm and 20 cm height and 5 cm and 10 cm in the horizontal x-direction. In this region, at low gas velocities ($1.4U_{mf}$), the particles are oriented horizontally. An increase in gas velocity leads to randomization of particle orientations, while further increase to $1.8U_{mf}$ and $2U_{mf}$ changes the particle's preferred orientation to vertical. Generally, we observed that with increasing the gas velocity the particles preference to align with the direction of gas flow increases.

In the distribution of the particle rotational velocity we see a clear difference between spherical and elongated particles. For a bed of spherical particles, we observe the highest rotational velocities in the bulk region and in the vicinity of the walls, while elongated particles posses the highest rotational velocities in the free-board region. These results are consistent with findings by [68]. Varying the particle aspect ratio also has an effect on the rotational velocity: we found that higher aspect ratio particles experience higher magnitudes of rotational velocity. As previously stated in section 3.4.3, we have to be cautious when considering the results of particle rotation obtained from MPT, because we are only capturing one mode of rotation.

A clear difference between spherical and elongated particles is also observed in the particle velocity distributions, discussed in section 3.4.2. For spherical particles, the velocity distribution shows that particles rise in the middle of the bed and descend next to the walls. This behavior is dominant at all gas velocities. However, in case of elongated particles we observed a completely different behavior. At low gas velocity ($1.4U_{mf}$), particles rise next to the walls and descend in the middle of the bed, a result which is not obtained for fluidization of spherical particles. For both spherical and elongated particles we encounter cases where double circulation patterns are present and flow is separated into two counter rotating vortices: a lower one where particles rise next to the walls and descend in the middle of the bed and an upper one where they are rising in the middle and descend next to the walls. For spherical particles this behavior can be noticed only at the lowest gas velocity ($1.4U_{mf}$) while it is the main characteristic of elongated particles. For AR-4 and AR-6 particles at a gas velocity of $1.6U_{mf}$, the particle velocity distribution is separated in two counter rotating vortices of the same size. Increasing the gas velocity reduces the size of the lower vortex, while the upper one where particles rise in the middle of the bed becomes the dominant one.

The considerable difference between spherical and elongated particles, reported in this chapter, emphasizes the need for further development of numerical models for simulation of gas-fluidized beds with elongated particles. The presented results will be valuable for future validations of simulation results. Magnetic Particle Tracking (MPT) is a powerful non-invasive experimental technique that can provide insight into the behavior of particles in full 3D fluidized bed. However, it also has its limitations. It can give us only time-averaged values for important fluidization parameters, therefore short lived structures, like bubbles and clusters, can not be captured with it. As bubble properties are important characteristics of gas-fluidized beds, necessary for optimization of the equipment, in the next chapter we will apply X-ray tomography analysis of the same systems to study bubbling behavior of elongated particles.

4

FLUIDIZATION OF SPHERICAL VERSUS ELONGATED PARTICLES - EXPERIMENTAL INVESTIGATION USING X-RAY TOMOGRAPHY

In many industrial applications, particles used in fluidized bed clearly deviate from ideal spheres. This leads to an increasing need for better understanding and developing better simulation models for fluidization of non-spherical particles. So far, the literature is quite scarce when it comes to experimental results which can be used for validation of numerical models. Also, the exact difference in fluidization behavior between spherical and elongated particles in dense fluidizing conditions is not well understood. In this chapter, we apply X-ray tomography to compare the fluidization behavior of a bed of a Geldart D-type spherical particles of aspect ratio 4 to that of volume equivalent spherocylindrical particles for different gas velocities. Even though the beds of both spherical and elongated particles are operating in the slugging regime, due their size and high bed height to width ratio, we see clear differences in their fluidization behavior. Our results indicate that the bed of elongated particles is slugging less than the one with spherical particles. This is indicated by a lower average bubble size in the case of elongated particles, together with a higher bubble rise velocity. The bed of elongated particles has a considerably higher distribution of small and medium bubbles. The slug waiting time distribution and slug frequency distribution indicate that a bed of elongated particles periodically switches between slugging and turbulent fluidization, unlike the bed of spherical particles which remains in the constant slugging regime.

Part of this chapter has been published in Chemical Engineering Journal **397** (2019) [94].

4.1. INTRODUCTION

Fluidized beds are irreplaceable equipment for the process industry, offering the best contact between a dispersed solid and continuous fluid phase. Fluidized beds have broad application, ranging from food-processing, waste disposal, coating, and chemical synthesis to energy production. Due to its important role in the chemical industry, fluidized beds have been the focus of numerous research in the past decades. However, a large fraction of this research focuses on a relatively smoothly bubbling fluidized beds with Geldart A or B particles. With such a versatile application of fluidized beds in industry, particles that are being fluidized can have various shapes and sizes. With the rising need to switch to more sustainable and renewable material and energy sources, fluidized beds have found an important role in biomass processing. Typical biomass particles used in the process industry, such as wood chips, pellets and straw like material are not only characterized by an elongated shape but are also of considerably larger size than powder like materials which are typically used in fluidized beds. These large elongated particles have much more complex particle-particle interactions and experience additional orientation dependent hydrodynamic forces [8, 32].

Fluidized beds with non-spherical particles have become a topic of research quite recently. There is already a large number of numerical investigations of such systems [7, 8, 71–73]. However, experimental studies are still quite scarce. Most experiments deal with pseudo 2D fluidized beds and are done using Particle Image Velocimetry (PIV) and/or Digital Image Analysis (DIA) [63, 76, 95]. However, in dense fluidized beds, such methods can only give insight into the near-wall region of the bed. To get insight into a full 3D fluidzed bed is much more challenging, and requires more advanced non-intrusive 3D experimental techniques. One possible methods is particle tracking. There are various methods of particle tracking techniques, the most famous one in fluidization is PEPT [96, 97]. The magnetic particle tracking technique (MPT) [67] is a novel method, that was successfully applied to fluidized beds of elongated particles [68, 70]. X-ray particle tracking is another method that was recently applied to investigate fluidization of binary mixtures of cylindrical and spherical particles [81, 82]. Particle tracking is a powerful method that gives insight into time-averaged single particle features, such as orientation, occupancy and translation and rotation velocities.

Tomographic methods like electrical capacitance tomography[98–100] and X-ray tomography on the other hand, can give an overall picture of gas-solids distribution. X-ray tomography was one of the first non-intrusive 3D experimental techniques applied on fluidized beds [77, 78, 101]. Tomographic reconstruction is a unique method which is able to give insight into gas bubble size, shape and location in the fluidized bed. The bubble dynamics plays a significant role in the fluidization process as it is the main driving force for solids motion and also determines the contact surface between gas and solid phase. Therefore, understanding the bubble behavior inside a fluidized bed is crucial for determining its efficiency and for equipment optimization. So far, most of the research using X-ray tomography focused on bubbling fluidized beds. However due to the use of various types of particles, fluidzed beds can operate in different regimes like slugging and turbulent fluidization [102]. This operating regime received considerably less attention compared to bubbling fluidization and most available findings are not of recent date [103–106]. Recently, a few more studies on slugging behavior in small diameter columns appeared [107–109]. However these focus only on Geldart A type powders. When it comes to Geldart D type particles, the only available models for estimating bubble properties have been developed by Baeyens and Geldart [103] and more recently by Agu et al. [4, 110]. Venier et al. [111] looked in to slugging fluidization of different type of particles, including Geldart D type, both experimentally and numerically. However these studies are limited to high bed height to diameter ratios.

In this chapter we investigate the fluidization behavior of a deep bed of Geldart D particles that is expected to operate in the slugging regime by means of X-ray tomography. We will compare fluidization properties of a bed containing spherical particles to one containing elongated, spherocylindrical particles, for different gas velocities.

4.2. EXPERIMENTAL SETUP AND METHODS

X-ray tomography (XRT) is a well established non-intrusive method for studying fluidzed beds [80, 112–114]. The main idea behind applying this method in fluidized bed investigation is to reconstruct the solid or gas fraction, based on the intensity of X-rays detected after passing trough the fluidized bed. The 2D image reconstruction for horizontal cross sections of the fluidized bed in this chapter is done using the simultaneous algebraic reconstruction technique (SART) as defined in [78], implemented in the ASTRA Toolbox package. This technique has already been successfully applied in the same fluidized bed vessel with other particles [115]. More information about the measurement principles can be found in [78, 79].

4.2.1. FLUIDIZED BED AND PARTICLES

In this work experiments were conducted in a perspex cylindrical column with an inner diameter of 14 cm and a height of 140 cm. The fluidized bed column is positioned inside the X-ray setup, surrounded by three X-ray sources placed at 120° around the column, as shown in Fig. 4.1. Each X-ray source is paired with a detector plate positioned on the opposite side, so that the column is in-between them. The X-ray sources used in this setup were YXLON Y.TU 160-D06 tubes with a maximum voltage of 150 kV and a maximum current of 12 mA. The used voltage and current depend on the investigated material and setup and have to be chosen such that the X-ray intensity is high enough to be detected after passing trough the full bed but not exceed the upper limit of the detector after passing through an empty bed. The choice of X-ray source voltage and current used in this work is shown in Fig 4.1 (b). The X-ray detector plates are Xineos-3131 with a sensitive area of 307 mm × 302 mm and a resolution of 1548 × 1524 pixels. The dimensions of each pixel are 198 µm × 198 µm. The energy range in which the detectors can operate is from 40 kV to 120 kV. In this work we used a field of view of 1548 × 100 pixels in order to do measurements at an elevated rate of 200 frames per second.

Two types of particles were considered, spherical (aspect ratio 1, AR-1) and volume equivalent spherocylinders of aspect ratio 4 (AR-4). The particles were 3D printed by means of selective laser sintering and made of alumide, a 3D printing material which is a mixture of nylon and aluminium fine powder. The obtained particles can be classified

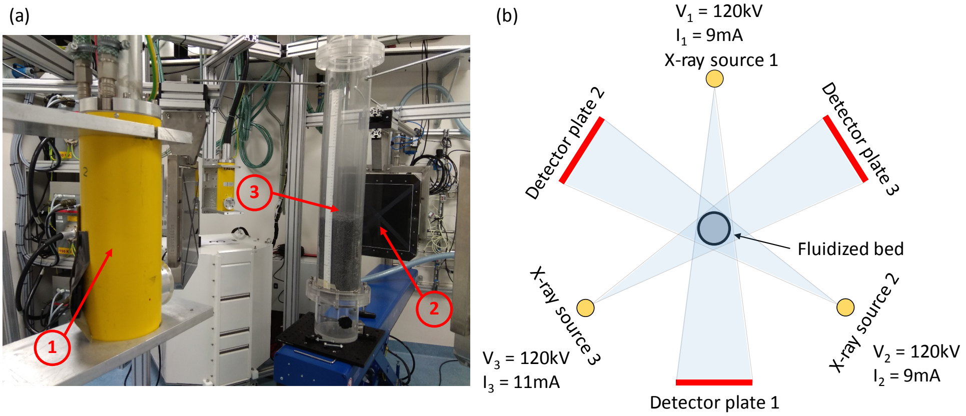

Figure 4.1: (a) View of the fluidized bed column between the source and the detector plate, 1-X-ray source tube, 2-Detector plate, 3-Fluidized bed column. (b) Schematic of X-ray setup (top view).

Parameter	AR-1	AR-4
Particle mass of the bed	3.3 kg	3.3 kg
Initial bed height	25.5 cm	26 cm
Particle length [L]	-	12 mm
Particle diameter [2R]	5.3 mm	3 mm
Particle material	Alumide	Alumide
Particle density	1442 kg/m^3	1442 kg/m^3
Mass of particle	0.112 g	0.112 g
Minimum fluidization velocity [U_{mf}]	1.58 m/s	1.7 m/s

Table 4.1: Particle properties.

as Geldart D particles and all their properties are listed in Table 4.1. In all experiments, the total particle mass in the bed was kept constant at 3.3 kg. The ratios between the initial bed height and the column diameter are 1.82 and 1.85 for AR-1 and AR-4 particles, respectively, so these fluidized beds are categorized as deep beds. Deep beds of Geldart D particles are expected to operate in the slugging regime [102].

4.2.2. CALIBRATION AND PHANTOM RECONSTRUCTION

Image reconstruction was done using two point calibration with the empty and full bed as upper and lower limits to the signal. Separate calibration has been performed for the spherical and elongated particles. The quality of the reconstruction is tested using phantoms of known dimensions. Cylindrical phantoms of 5.2 cm and 2 cm diameter were inserted vertically in the packed bed of particles. Images of the reconstructed horizontal cross sections of the phantoms and their estimated sizes are shown in Fig. 4.2. The reconstructed image is presented on a 100 × 100 cell grid, where the gray area indicates space around the column, black color refers to areas of the bed packed with

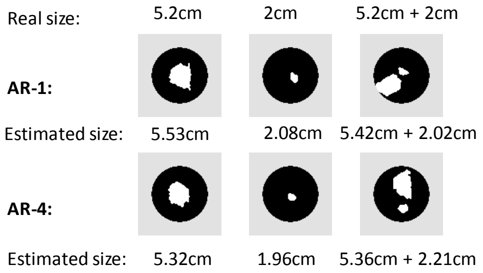

Figure 4.2: Reconstructions of different combinations of phantoms in beds of AR-1 and AR-4 particles.

particles, while white color responds to reconstructed voids (bubbles). The estimations of the phantom sizes are accurate: in the worst case it overestimates the real size by only 6.34 %. Based on the phantom reconstructions, the threshold chosen for distinguishing bubbles from a packed area of the bed is 0.09 (relative between minimum and maximum intensity value). As the particles used in this investigation are quite coarse (see Table 3.2), the voids presented inside the packing can also be quite large and they can lead to a distortion of the reconstructed phantom shape and overestimation of its size. This is particularly the case for the large phantom which, due to its higher contact surface with the particles around it, has a large relative overestimation of its size. The 2 cm phantom is reconstructed successfully in all cases and therefore we set it as the minimum size of the bubbles that can be reconstructed with certainty. All bubbles smaller than 2 cm will be neglected in the further analysis.

4.3. RESULTS

In this section we present results on the average bubble diameter, average bubble velocity, waiting time distribution between the slugs and slug frequency. The measurements were done at two different heights within the bed: $h_{low} = 70$ mm and $h_{hig} = 240$ mm above the distributor plate. For AR-1 particles we investigated 5 different excess gas velocities: $U - U_{mf} = 0.4$, 0.65, 0.9, 1.15 and 1.4 m/s. Due to the specifics of its fluidization, AR-4 particles were fluidized at only three excess gas velocities: $U - U_{mf} = 0.6$, 0.9 and 1.15 m/s. At a gas velocity of $U - U_{mf} = 0.4$ m/s, AR-4 particles were in an active channeling regime and there were no proper bubbles or slugs forming, while at the highest gas velocity of $U - U_{mf} = 1.4$ m/s slugs of particles were lifted to the top of the column and remain stuck there, clogging the column.

As stated in section 4.2.2 bubbles with an average diameter less than 2 cm are neglected in further analysis together with bubbles that are present in less than 10 frames. Measurements are done for 60 s in case of average bubble diameter and bubble velocity, while for the waiting time distribution and slug frequency measurements were run for 600 s in order to collect sufficient statistics.

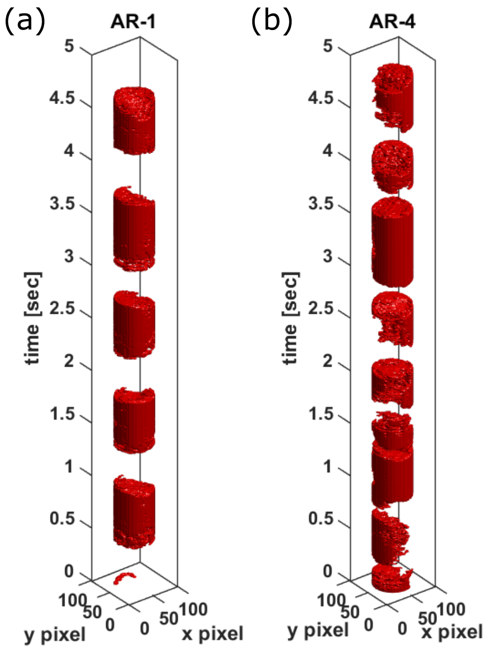

Figure 4.3: Bubble visualizations for at bed height of 240mm and $U - U_{mf} = 0.65$ m/s for (a) AR-1 and (b) AR-4 particles.

4.3.1. AVERAGE BUBBLE DIAMETER

The average bubble diameter can be directly obtained from the reconstructed tomographic images. For each frame, individual bubbles are detected and their surface is calculated by summing the number of pixels that are allocated to them. A sphere-equivalent bubble diameter is calculated for each bubble and the average bubble diameter is calculated for the whole measurement. Some examples of reconstructed images and bubble visualizations are presented in Fig. 4.3. This is a pseudo-3D representation of reconstructed bubbles as the z-axis is a temporal and not spatial coordinate. Already from this visualizations it is clear that the fluidized beds are operating in the slugging regime. Therefore the bubble size actually refers to the slug size.

Time averaged bubble diameters for AR-1 and AR-4 particles at two heights in the bed and for different excess gas velocities are shown in Fig. 4.4. As the fluidized bed is operating in the slugging regime, a change of fluid velocity does not have a considerable effect on the bubble diameter at the higher position in the bed. However it can be noticed that in all cases the average bubble diameters are smaller for the AR-4 particles than for the AR-1 particles. This can indicate that the AR-4 particles are actually slugging less and have more small and medium size bubbles. In all cases investigated, bubble diameters are larger at the higher position in the bed which is something already expected from basic theory of bubbling fluidized beds [102]. However, it is surprising that the average bubble diameter at the lower height in the bed of AR-1 particles is reducing with

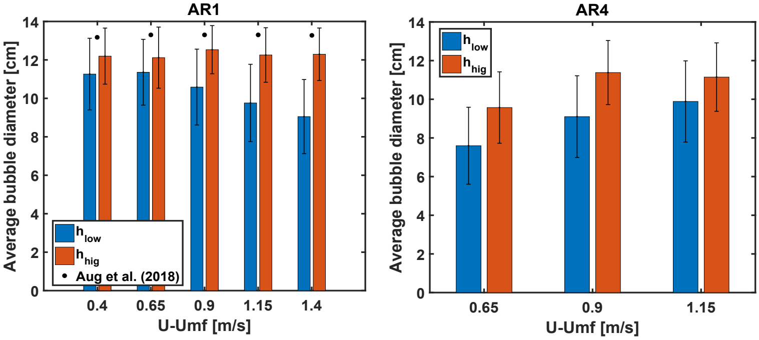

Figure 4.4: Average bubble diameter for AR-1 and AR-4 particles on different excess gas velocities. Error bars indicate standard deviation of bubble diameters. The dots indicate indicate the average bubble size predicted by Aug et al. [4] for spherical (AR-1) particles in a high aspect ratio bed.

increasing fluid velocity.

This counter-intuitive results can be explained if we look at the average number of bubbles shown in Fig. 4.5. It can be seen that at high position in the reactor (red crosses), the number of bubbles remains roughly the same or shows a slight increase with an increase of gas velocity. At a low position in the reactor (blue stars), for AR-1 particles it can be seen that the decrease of average bubble diameter is accompanied by a monotonous increase of number of bubbles. On the other hand Fig. 4.4 shows that for AR-4 particles the average bubble diameter at the low position in the bed is increasing and from Fig. 4.5 it can be seen that this is accompanied by a decrease in the number of bubbles.

A model for predicting the average bubble diameter for Geldart D type particles in the slugging regime, which was recently developed by Aug et al. [4], is the only one comparable with the fluidized bed investigated in this chapter. Even though this model was not tested for bed height to diameter ratios below 4 and for $U - U_{mf}$ greater than 0.4 m/s, we compare it to our experimental results for AR-1 particles in Fig. 4.4. This model does not depend on the height in the bed and it can be seen that it slightly overpredicts the bubble diameters, but it is still in the upper range of standard deviation at the higher position in the bed. However for AR-4 particles the model predicts fully developed slugs with diameters close to the column diameter (13.96 cm) and does not change considerably with increase of gas excess velocity, therefore it is not included in Fig. 4.4.

In order to get a better insight in the fluidization behavior of the considered particles, the bubble size distributions are presented in Fig. 4.6. The clear peak at a bubble diameter of around 13 cm indicates clear slugging behavior, knowing that the column diameter is 14 cm. It can be seen that in all cases the AR-1 particles show more extreme slugging behavior. The AR-4 particles show a much higher distribution of small and medium size bubbles compared to the AR-1 particles. The height of the peak at maximum bubble diameter is also smaller for AR-4 than AR-1 particles. At the lower position in the bed (H_{Low}) it can also be noted that an increase in the gas velocity leads to an increase of the number of small and medium size bubbles for AR-1 particles, however never reaching the large number of small and medium bubbles observed for AR-4 particles. In the case

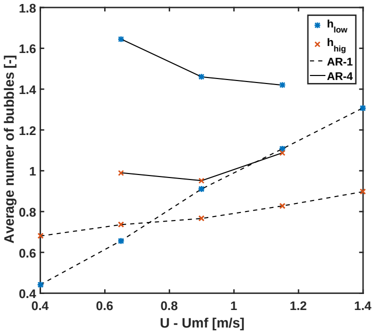

Figure 4.5: Average number of bubbles present in the horizontal cross-sections at low (*) and high (x) positions in the bed, for AR-1 (- - -) and AR-4 (—) particles, as a function of excess gas velocity.

of AR-4 particles, the opposite is the case: an increase of the gas velocity actually reduces the number of small and medium size bubbles while increasing the number of slugs. In summary, at the lower position in the bed, the trend of the bubble size distribution with gas velocity is opposite for AR-1 and AR-4 particles, where at high gas velocity the distribution seem to approach each other. In all cases the prevalence of medium and small size bubbles is lower at the higher position in the bed.

4.3.2. BUBBLE RISE VELOCITY

The bubble rise velocity is calculated by applying a cross-correlation between the signals at the 5th and 95th rows of pixels of the measured domain. The vertical distance of 90 pixels between the two rows corresponds to a distance of 1.26 cm. This is sufficiently large to make an accurate estimate of the bubble rise velocity, yet sufficiently small to neglect changes in bubble size (i.e. they do not grow, split or coalesce) over this distance. Details of the procedure of applying a cross-correlation function for calculating the bubble rise velocity are explained in [80].

Fig. 4.7 presents the bubble rise velocities for AR-1 and AR-4 particles as a function of bed height. In all cases the bubble rise velocity is larger at the higher position in the bed and it generally increases with an increase of the gas velocity. The only exception is the slightly higher bubble rise velocity observed for AR-1 particles at the lower position in the bed at an excess gas velocity of 0.4 m/s compared to that at the next excess gas velocity of 0.65 m/s. This is caused by the presence of fewer but significantly larger bubbles at the lowest gas velocity. In the case of AR-4 particles, the bubble rise velocities are considerably higher than for AR-1 particles. This is another indication that AR-4 particles are slugging less than the AR-1 particles, because large slugs have a lower rise velocity than smaller bubbles [102].

4.3.3. WAITING TIME DISTRIBUTION

We now investigate the waiting time, defined as the time that passes between two consecutive slugs passing trough a horizontal measurement plane. In particular, we are in-

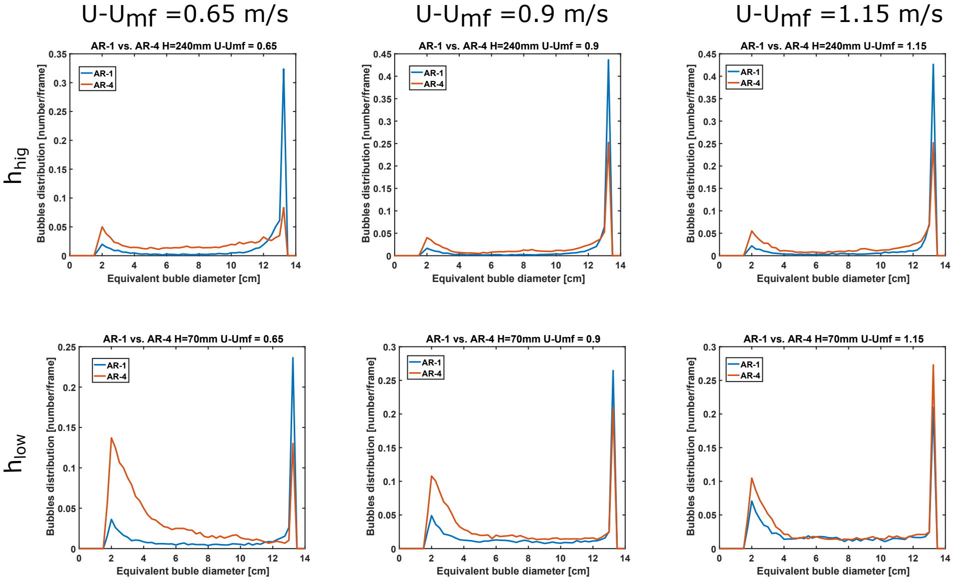

Figure 4.6: Bubble size distribution for AR-1 and AR-4 particles on different excess gas velocities and low and high positions in the bed.

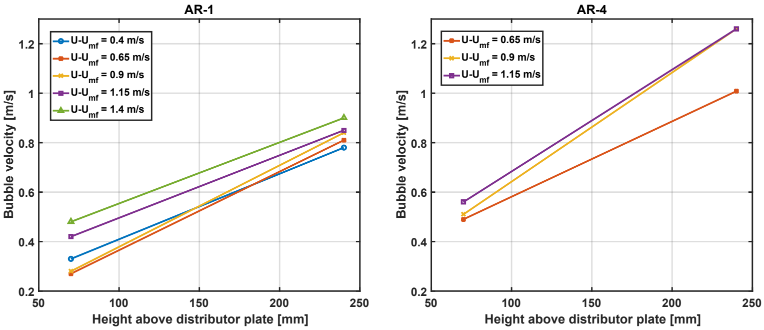

Figure 4.7: Bubble velocities for AR-1 and AR-4 particles on different gas excess velocities as a function of bed height.

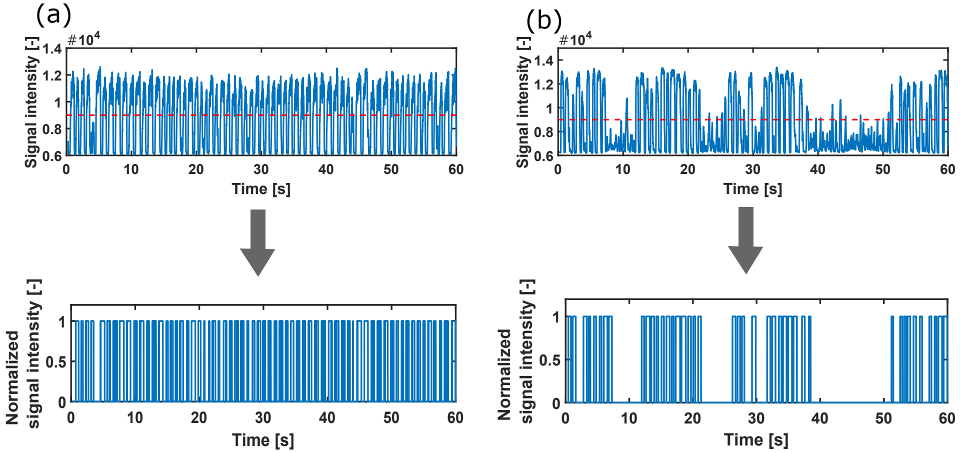

Figure 4.8: Signal intensity before and after applying threshold for (a) AR-1 and (b) AR-4 particles at h_{hig} and $U - U_{mf} = 0.65\,\mathrm{m/s}$

terested in the waiting time *distribution*. The signal intensity measured on one of the detector plates is averaged over a horizontal row of pixels at the height of interest. In order to consider only slugs, and neglect small and medium size bubbles, we apply a threshold on the averaged signal intensity, as shown in Fig. 4.8. The waiting time is calculated as the time interval between the centers of two consecutive slugs identified through the normalized signal intensity shown in the lower images of Fig. 4.8. Already from the signal intensities in the upper images of Fig. 4.8, a clear difference between AR-1 and AR-4 particles can be seen. In the case of AR-1 particles, high intensities peaks corresponding to slugs appear regularly with almost identical distance between them. In contrast, for AR-4 particles we observe a mixture of periods with high intensity peaks and periods with smaller intensity peaks, the latter of which corresponds to small and medium bubbles passing by. Similar trends are observed for other gas excess velocities (not shown).

For brevity we present the waiting time distributions for AR-1 and AR-4 particles only at the higher position in the bed h_{hig} because we find this to be the most relevant for analyzing slugging behavior. Fig. 4.9 shows quite discrete waiting time distributions for AR-1 particles. For all gas velocities there is a relatively narrow peak at a waiting time of around 1 s. At the lowest gas velocity considered (Fig. 4.9 (a)) the main peak at 1 s is followed by clear peaks at around 2, 3 and 4 s. This shows that large slugs are sometimes skipped at low gas velocity, probably because a smaller slug passes by which does not overcome our threshold value for detection. With increasing the gas velocity these peaks at longer waiting times are disappearing followed by a widening of the main peak at 1 s. Overall, this shows that slugs for AR-1 particles appear regularly with break of around 1 s between them.

Fig. 4.10 shows the waiting time distributions for AR-4 particles. Notice that AR-4 particle show completely different waiting time distributions than AR-1 particles. For AR-1 particles all waiting time distributions were in range from 0.5 s up to 7.5 s, with

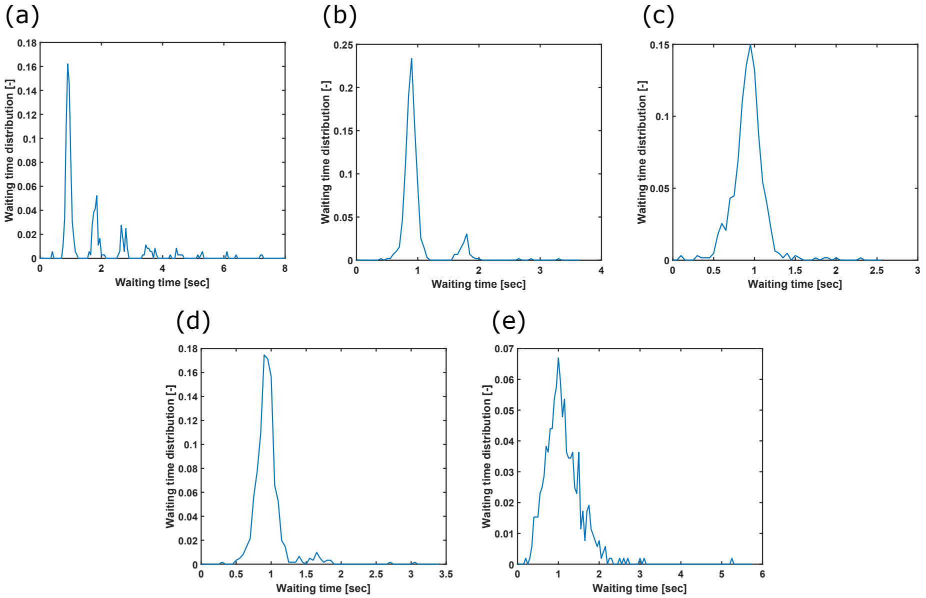

Figure 4.9: Waiting time distribution for AR-1 particles at the higher bed height h_{hig} and excess gas velocities $U - U_{mf}$ of: (a) 0.4, (b) 0.65, (c) 0.9, (d) 1.15 and (e) 1.4 m/s.

the majority of the distributions occurring in the range between 0.5 s and 2 s. For AR-4 particles, a much wider waiting time distribution can be seen, with peaks appearing at 12, 20 and even up to 60 s. Due to this large spread in waiting times, some of the figures in Fig. 4.10 are presented on a logarithmic scale for the waiting time. Clearly, there are long periods in the fluidization of AR-4 particles without appearance of slugs, but rather with medium and smaller size bubbles. This explains lower average bubble sizes and higher average number of bubbles appearing for AR-4 particles discussed in section 4.3.1.

4.3.4. SLUG FREQUENCY

The waiting time distribution discussed in the previous section indicate that there is a certain regularity in slug appearance. More information about the frequency of slugs can be obtained from a power spectrums of the signal intensity as seen in Fig. 4.8. The power spectrum is calculated by applying a fast Fourier transformation with a Hanning window on the normalized signal intensity. This frequency analysis is done for the same cases as the waiting time distribution discussed in section 4.3.3.

The power spectra for AR-1 particles are shown in Figure 4.11. As expected, a clear peak at a frequency of 1 Hz can be observed at all gas excess velocities. The dominant frequencies that can be seen in our cases are in the same range as predicted by [103]. At lower gas velocities, Fig. 4.11 (a) and (b) show smaller peaks at 2, 3 and 4 Hz. These peaks should be distinguished from the peaks that appear in Fig. 4.11 (c), but rather represent the 2nd, 3rd and 4th harmonics of the main frequency at 1 Hz. This demonstrates how

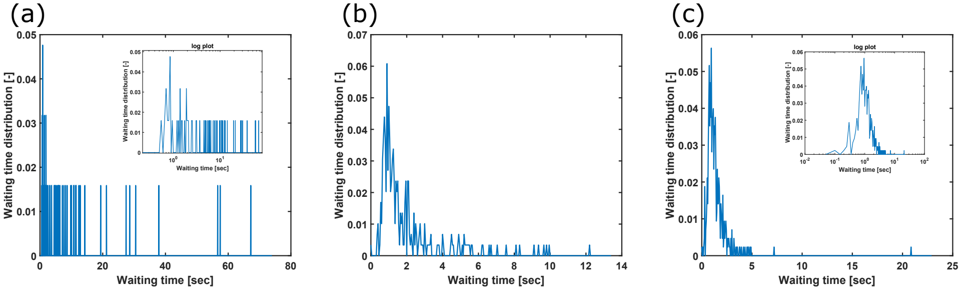

Figure 4.10: Waiting time distribution for AR-4 particles at the higher bed height h_{hig} and excess gas velocities $U - U_{mf}$ of: (a) 0.65, (b) 0.9 and (c) 1.15 m/s.

regular the frequency of slug appearance actually is. With further increase of gas velocity, Fig. 4.11 (d) and (e) shows that the main peak at 1 Hz is widening, which indicates a transition to a more turbulent fluidizing regime.

Fig. 4.12 shows the power spectra for AR-4 particles at different gas excess velocities. It can be seen that frequency of slugs ranges predominantly between 0 and 2 Hz, however unlike the case of AR-1 particles no distinct peaks can be seen. This confirms that for AR-4 particles slugs do not appear as regularly as for AR-1 particles. The increased randomness in slug appearance indicates that the AR-4 fluidized bed is actually operating in a turbulent regime [105, 116].

4.4. DISCUSSION

In this work, we applied X-ray tomography (XRT) to investigate the differences in fluidization behavior between spherical (AR-1) and elongated (AR-4) particles. Two different bed heights were considered, together with five different excess gas velocities for spheres and three for elongated particles. As the particles used in this investigation are Geldart D particles, and the initial bed height corresponds to a deep bed, the fluidized bed was operating in a slugging regime. Even though the considered particles were volume equivalent and the initial bed heights were approximately the same, the results presented in this chapter show considerably different behavior between AR-1 and AR-4 particles.

Regarding the average bubble diameter, AR-4 particles showed lower bubble sizes than AR-1 particles for all considered cases (Fig. 4.4), which was accompanied by a higher average number of bubbles for the case of AR-4 particles (Fig. 4.5). This finding was supported by the results on the bubble size distribution, which clearly showed a higher tendency for AR-1 particles to form slugs with almost no small or medium size bubbles (Fig. 4.6). On the other hand, AR-4 particles showed a considerably higher distribution of medium and small size bubbles. For the average bubble rise velocity, AR-4 particles showed higher values than AR-1 particles (Fig. 4.7). This was another indication that AR-4 particles are slugging less as smaller size bubbles have higher rise velocities than slugs [102].

The waiting time distributions between slugs and their power spectra, discussed in

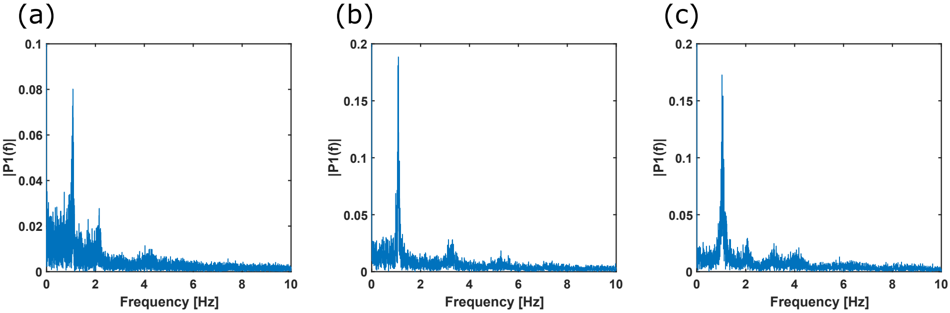

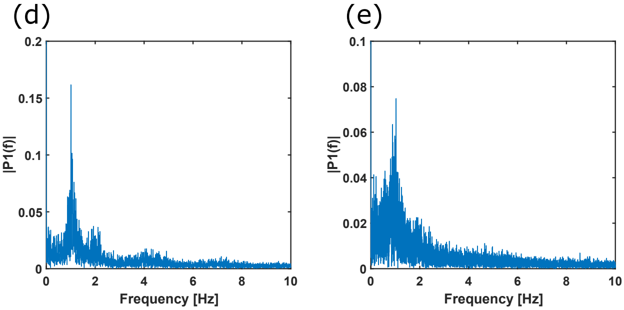

Figure 4.11: Power spectra for appearance of slug for the AR-1 particles at the higher bed height h_{hig} and excess gas velocities $U - U_{mf}$ of: (a) 0.4, (b) 0.65, (c) 0.9, (d) 1.15 and (e) 1.4 m/s.

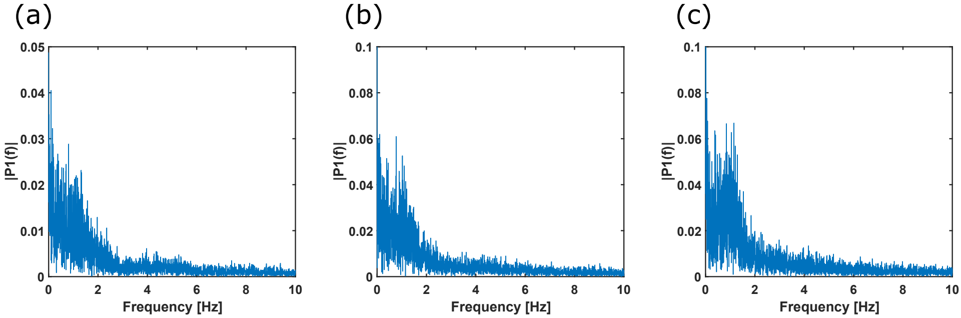

Figure 4.12: Power spectra for the AR-4 particles at the higher bed height h_{hig} and excess gas velocities $U - U_{mf}$ of: (a) 0.65, (b) 0.9 and (c) 1.15 m/s.

sections 4.3.3 and 4.3.4 gave more insight in the periodicity and frequency of slug appearance. AR-1 particles showed a clear and narrow main peak in waiting time distribution at 1 s and a corresponding dominant frequency of 1 Hz. However, the AR-4 particles waiting time distributions showed a much larger spread and the dominant peak around 1 s was considerably wider than in the case of AR-1 particles. Similar behavior was noticed in the power spectra where the main frequency ranges between 1 and 2 Hz but without any clear peak of dominant frequency. This showed that once the bed of AR-1 particles is in a slugging regime, slugs appear with a quite regular frequency while AR-4 particles show much more turbulent behavior and switch between slugging and turbulent behavior [105].

Based on the results presented in this chapter, it can be concluded that a bed of elongated particles shows more turbulent fluidizing behavior than a bed of volume-equivalent spherical particles. With an increase of gas velocity, a slugging bed of AR-1 particles will at some point transition to turbulent fluidization [102, 105]. We started to see an indication of this transition in our experiments at $U - U_{mf} = 1.4\,\mathrm{m/s}$. However for elongated AR-4 particles more turbulent fluidization can be already be seen at the lowest gas excess velocity studied. When fluidizing elongated particles, periodic transitions between slugging and turbulent fluidization can be observed. Elongated particles also show other specifics when it comes to fluidization, starting from channeling, different particle rotational velocities and solids circulation patterns, as discussed in [70, 95].

We note that in this chapter we investigated non-spherical particles of a specific shape and aspect ratio, namely spherocylinders of aspect ratio 4. One may wonder what is the limit of aspect ratio and shape that still shows the qualitatively different fluidization behavior between non-spherical particles and spheres. We expect this limit will be for elongated particles around an aspect ratio of 2, because particle interlocking and hydrodynamic lift and torque start to play an important role for elongated particles with aspect ratios beyond approximately 2 [8, 32]. However, at this point this is speculation, and more experimental work is needed to confirm this.

Applying X-ray tomography for coarse systems such as these has its limitations and challenges. Therefore we advice a certain caution when considering some of presented results. From the phantom reconstructions shown in section 4.2.2 it can be seen that while the sizes of phantoms are estimated with high accuracy, the same cannot be said for their shapes. Even though we showed that small phantom with 2 cm diameter can be reconstructed with high accuracy, the high distribution of small size bubbles in Fig. 4.6 for AR-4 particles at low position in the bed should be interpreted with caution. Due to the higher turbulence, solid particles can be more dispersed in the gas phase and the bed shows a broader distribution of voidages, making it harder to make a clear distinction between the bubble and emulsion phases [117]. Considering all the specifics and the observed different fluidization behavior of elongated particles, we emphasize the need for better understanding and further development of numerical simulations of these kinds of systems. The results presented in this chapter, together with our previous findings using Magnetic particle tracking (MPT) technique [70], will be valuable for future validation of simulation results.

4.5. CONCLUSION

The results presented in this chapter demonstrate clear difference in fluidization behavior between spherical and elongated particles of Geldart D type. Elongated particles show a considerably larger distribution of small and medium size bubbles compared to spherical particles which show larger average bubble diameters for all gas excess velocities and bed heights considered. In all cases, elongated particles showed larger average bubble velocities. A clear difference was also observed in the waiting time distribution between slugs. In case of spherical particles, slugs appeared with more regular waiting time than elongated particles, which demonstrated a wide distribution of waiting times. Similar behavior was observed when looking into the slug frequency where spherical particles showed a clear peak at a frequency of 1 Hz, while elongated particles had a wider spread up to 2 Hz and showed no distinct peaks. All presented results indicate that elongated particles show less slugging behaviour than spherical particles and that during fluidization they periodically switch between slugging and more turbulent fluidization.

5

FLUIDIZATION OF ELONGATED PARTICLES - EFFECT OF MULTI-PARTICLE CORRELATIONS FOR DRAG, LIFT AND TORQUE IN CFD-DEM SIMULATIONS

Having proper correlations for hydrodynamic forces is essential for successful CFD-DEM simulations of a fluidized bed. For spherical particles in a fluidized bed, efficient correlations for predicting the drag force, including the crowding effect caused by surrounding particles, are already available and well tested. However for elongated particles, next to the drag force, the lift force and hydrodynamic torque also gain importance. In this work we apply recently developed multi-particle correlations for drag, lift and torque in CFD-DEM simulations of a fluidized bed with spherocylindrical particles of aspect ratio 4 and compare them to simulations with widely used single-particle correlations for elongated particles. Simulation results are compared with previous magnetic particle tracking (MPT) experimental results. We show that multi-particle correlations improve the prediction of particle orientation and vertical velocity. We also show the importance of including hydrodynamic torque.

Part of this chapter has been accepted to AIChE Joural (2020) [118].

5.1. Introduction

Fluidized beds are irreplaceable equipment in industry as they offer the highest contact between solid particles and gas, together with rapid mixing of particles and most efficient heat transfer between gas and solids. Due to their industrial importance, fluidized beds have been subject of numerous experimental and numerical research over the past century. Thanks to the advancements in computer performance in recent decades, many numerical models, able to successfully simulate operation of industrial scale fluidized beds with spherical particles have been developed. Usage of such models considerably reduce the time and costs of optimization and development of the processes that rely on fluidized beds. Coupled CFD-DEM is viewed as one of the most accurate models in fluidized bed research because it fully resolves particle-particle interactions while particle-fluid interactions are resolved through closures for hydrodynamic forces. Having closures that can accurately predict the hydrodynamic forces experienced by the particles in a fluidized bed is crucial for successful usage of CFD-DEM models.

A considerable number of processes in industry rely on usage of fluidized beds for manipulating granular materials where the particle shape is non-spherical. This is specifically the case for processes where biomass is used. The biomass is usually dried, milled and processed into pellets. These kinds of particles are considerably larger than powder like materials usually used in fluidized beds and are characterized by an elongated shape. Existing numerical models, developed for fluidization of spherical particles, cannot be applied to fluidization of these kinds of particles as elongated particles will have much more complex particle-particle interactions together with orientation dependent hydrodynamic forces. Our previous investigation [70] showed that additional forces like shape induced lift force and hydrodynamic torque have considerable effect on fluidization of elongated particles and cannot be neglected.

While fluidization of spherical particles is thoroughly investigated and there is a number of accurate and well tested drag correlations for spherical particles available in literature [119], this is not the case for elongated particles. When it comes to the drag force experienced by a single elongated particle, a few correlations are available in literature. Haider and Levenspiel [56] presented a drag correlation based on particle sphericity which however did not take into account particle orientation. Ganser [57] on the other hand proposed a drag correlation based on Stokes' and Newton's shape factors. More recently, Hölzer and Sommerfeld [120] introduced a general drag force correlation based on particle sphericity, crosswise and lengthwise sphericity and Reynolds number, while Zastawny et al. [2] and Sanjeevi et al. [3] proposed correlations for specific particle shapes. So far, the correlation by Hölzer and Sommerfeld [120] has been widely applied in fluidization of non-spherical particles, as it proved to be the most flexible. For shape induced lift force and hydrodynamic torque on elongated particles, the only correlations available in literature are proposed by Zastawny et al. [2], Ouchene et al.[35] and Sanjeevi et al. [3].

During fluidization, particles rarely find themselves isolated in a fluidized bed, but are most of the time surrounded by other particles in dense fluidizing conditions. The surrounding particles in dense fluidizing conditions can have an effect on hydrodynamic forces experienced by a particle. For spherical particles there are correlations that takes into account this effect of the surrounding particles. The first one that bridged dilute and dense particulate conditions was the expression by Di Felice [58]. Recently Tenneti et al. [121] and Tang et al. [122] proposed new expressions for static assemblies of spheres, and Rong et al. [59] suggested extension of the Di Felice equation. For non-spherical particles the multi-particle effect only recently came into the spotlight when Li et al. [123] discussed the drag and lift force and He and Tafti [124] the drag, lift and torque on assemblies of ellipsoidal particles. So far, the only correlations for drag, lift and torque applicable to elongated particles that take into account the effect of surrounding particles, have been proposed by Sanjeevi et al. [5]. However this correlations has not been applied in CFD-DEM simulations so far, and their influence on fluidization is still unknown.

In this chapter, we investigate the effect of multi-particle correlations for hydrodynamic forces and torque on the fluidization charcateristics of elongated, spherocylindrical particles with aspect ratio 4 using CFD-DEM simulations. Simulations with Sanjeevi multi-particle correlations [5] are compared to simulations with the Hölzer and Sommerfeld drag model [120], expanded with Di Felice expression [58] and lift and torque correlations proposed by Zastawny et al. [2] for an isolated particle. For validation, the simulation results are compared with experimental results previously obtained using magnetic-particle tracking (MPT) [8].

5.2. NUMERICAL MODEL

The CFD-DEM algorithm used in this chapter is based on open source software, namely OpenFoam to solve the fluid equations (CFD) and LIGGGHTS to solve the particle equations (DEM). These two algorithms are coupled using open source CFDEM coupling [43]. The open source codes were adapted so that they can be applied to spherocylindrical particles without relying on a multi-sphere approach. More in-depth information about the model and its validation can be found in previous Chapter 2 and in work by Mahajan et al. [7].

Drag force is the strongest force that the fluid exerts on particles and is the main driver of fluidization. In this chapter we use two approaches to calculate the drag force: the single particle drag correlation by Hölzer and Sommerfeld [120], extended with Di Felice's [58] expression to take into account the effect of surrounding particles and by the correlation proposed by Sanjeevi et al. [5], developed specifically for assemblies of elongated particles.

Single particle drag force with Di Felice extension. The correlation presented by Hölzer and Sommerfeld [120] can be applied to arbitrary shaped particles where the shape of the particle is taken into account through sphericity, and lengthwise and crosswise sphericity. The drag force coefficient C_D as proposed by Hölzer and Sommerfeld is:

$$C_D = \frac{8}{\mathrm{Re}_p}\frac{1}{\sqrt{\Phi_\parallel}} + \frac{16}{\mathrm{Re}_p}\frac{1}{\sqrt{\Phi}} + \frac{3}{\sqrt{\mathrm{Re}_p}}\frac{1}{\Phi^{3/4}} + 0.42 \times 10^{0.4(-\log\Phi)^{0.2}}\frac{1}{\Phi_\perp} \tag{5.1}$$

where Re_p is the particle Reynolds number $\mathrm{Re}_p = \rho_f d_p \left|\mathbf{v}_f - \mathbf{v}_i\right| / \eta_f$ with ρ_f the fluid density, d_p the volume-equivalent particle diameter, η_f the fluid viscosity, Φ the particle sphericity, $\Phi_\parallel$ the lengthwise sphericity, and $\Phi_\perp$ the crosswise sphericity.

The effect of surrounding particles (crowding effect) on the drag force experienced by a particle is taken into account through Di Felice's [58] modified drag force expression:

$$\mathbf{F}_D = \frac{1}{2} C_D \rho_f \epsilon_f^{2-\chi} \frac{\pi}{4} d_p^2 \left|\mathbf{v}_f - \mathbf{v}_i\right| (\mathbf{v}_f - \mathbf{v}_i) \tag{5.2}$$

where $\mathbf{v}_f$ is the fluid velocity interpolated to the location of particle i, $\mathbf{v}_i$ is the velocity of particle i, and χ is the Di Felice correction factor given by

$$\chi = 3.7 - 0.65 \exp\left[(-(1.5 - \log(\mathrm{Re}_p))^2/2\right] \tag{5.3}$$

where the particle Reynolds number Re_p is calculated using the expression defined after equation 2.10. Note that the appearance of the additional factor ϵ_f^2 in equation 5.2 comes from the use of a superficial relative velocity in Di Felice's work.

The Di Felice expression was originally developed for spherical particles but because it is one of the few available expressions to take into account crowding effects it has also been applied in simulations of elongated particles fluidization [7, 63, 65, 70, 125, 126].

Multi-particle drag correlation proposed by Sanjeevi et al. [5] calculates the drag force experienced by a particle as:

$$\mathbf{F}_D = 3\pi\eta_f d_p \overline{F}_{D,\phi} (\mathbf{v}_f - \mathbf{v}_i) \tag{5.4}$$

where $\overline{F}_{D,\phi}$ is the average drag (normalised by the drag on an isolated volume equivalent sphere) based on particle orientation to the fluid flow. As the average drag $\overline{F}_D$ for different particle incident angles ϕ follows a sine-square interpolation, for individual particles [3] as well as assemblies [5], it can be calculated for any ϕ as:

$$\overline{F}_{D,\phi} = \overline{F}_{D,\phi=0^\circ} + (\overline{F}_{D,\phi=90^\circ} - \overline{F}_{D,\phi=0^\circ}) \sin^2\phi \tag{5.5}$$

$\overline{F}_{D,\phi=0^\circ}$ and $\overline{F}_{D,\phi=90^\circ}$ are a function of Re and ϕ:

$$\overline{F}_D(\mathrm{Re}, \epsilon_s) = F_{d,isol} \cdot (1-\epsilon_s)^2 + F_{\epsilon_s} + F_{\mathrm{Re},\epsilon_s} \tag{5.6}$$

The corresponding terms are as follows:

$$F_{d,isol}(Re) = C_{d,isol} \frac{\mathrm{Re}}{24} \tag{5.7}$$

where $C_{d,isol}$ is calculated as proposed by Sanjeevi et al. [3]:

$$C_{d,isol} = \left(\frac{a_1}{\mathrm{Re}} + \frac{a_2}{\mathrm{Re}^{a_3}}\right) \exp(-a_4 \mathrm{Re}) + a_5 (1 - \exp(a_4 \mathrm{Re})) \tag{5.8}$$

where the coefficients ($a_1 ... a_5$) for parallel ($\phi = 0^o$) and perpendicular ($\phi = 90^o$) orientation are given in Table 5.1.

$$F_{\epsilon_s}(\epsilon_s) = a\sqrt{\epsilon_s}(1-\epsilon_s)^2 + \frac{b\epsilon_s}{(1-\epsilon_s)^2} \tag{5.9}$$

$$F_{\mathrm{Re},\epsilon_s}(\mathrm{Re}, \epsilon_s) = \mathrm{Re}^c {\epsilon_s}^d \left(e(1-\epsilon_s) + \frac{f{\epsilon_s}^3}{(1-\epsilon_s)}\right) + g\epsilon_s(1-\epsilon_s)^2 \mathrm{Re} \tag{5.10}$$

The coefficients for Equations 5.9 and 5.10 for parallel and perpendicular orientation are also given in Table 5.1.

	$\overline{F}_{\mathrm{D}}$			$C_{d,isol}$	
Coefficient	$\phi = 0°$	$\phi = 90°$		$\phi = 0°$	$\phi = 90°$
a	2	3	a_1	24.48	31.89
b	11.3	17.2	a_2	3.965	5.519
c	0.69	0.79	a_3	0.41	0.229
d	0.77	3	a_4	0.0005	0.0032
e	0.42	11.12	a_5	0.15	1.089
f	4.84	11.12			
g	0	0.57			

Table 5.1: Coefficients for drag force calculation as proposed by Sanjeevi et al. [3],[5].

Lift force appears when the long axis of an elongated particle is inclined with respect to the direction of relative fluid flow. The lift force acts in the direction perpendicular to the fluid's relative velocity $\mathbf{v}'_{fi} = \mathbf{v}_f - \mathbf{v}_i$ and lies in the plane defined by the particle long axis orientation vector $\mathbf{u}_i$ and $\mathbf{v}'_{fi}$. The lift force magnitude F_L is multiplied by the lift force orientation vector $\hat{\mathbf{e}}_{L_0}$ which is given as

$$\hat{\mathbf{e}}_{L_0} = \frac{\mathbf{u}_i \cdot \mathbf{v}'_{fi}}{\left|\mathbf{u}_i \cdot \mathbf{v}'_{fi}\right|} \frac{(\mathbf{u}_i \times \mathbf{v}'_{fi}) \times \mathbf{v}'_{fi}}{\left\|(\mathbf{u}_i \times \mathbf{v}'_{fi}) \times \mathbf{v}'_{fi}\right\|} \tag{5.11}$$

The resultant lift force experienced by a particle is expressed as $\mathbf{F}_L = F_L \hat{\mathbf{e}}_{L_0}$, while the magnitude of lift force is calculated with either the single particle correlation proposed by Zastawny et al. [2] or the multi-particle correlation proposed by Sanjeevi et al. [5].

Single particle lift force. The magnitude of shape induced lift force experienced by an isolated particle is expressed as

$$F_L = \frac{1}{2} C_L \rho_f \frac{\pi}{4} d_p^2 \left|\mathbf{v}_f - \mathbf{v}_i\right|^2 \tag{5.12}$$

where C_L is the lift force coefficient calculated using Zastawny et al. correlation [2]:

$$C_{L,\phi} = \left(\frac{b_1}{\mathrm{Re}^{b_2}} + \frac{b_3}{\mathrm{Re}^{b_4}}\right) \sin(\phi)^{b_5 + b_6 \mathrm{Re}^{b_7}} \cos(\alpha)^{b_8 + b_9 \mathrm{Re}^{b_{10}}} \tag{5.13}$$

Fitting coefficients used for the correlation can be found in Table 5.2.

Multi-particle lift force. In this chapter we have applied a simplified function for shape induced lift force, proposed by Sanjeevi et al. [5]. In this simplified approach the average lift force $\overline{\mathrm{F}}_L$ (normalised by the drag on an isolated volume equivalent sphere) experienced in a multi-particle system at different ϕ is calculated based on its relation to the normalised drag force as:

$$\overline{F}_{L,\phi} = (\overline{F}_{D,\phi=90°} - \overline{F}_{D,\phi=0°}) \sin\phi \cos\phi \tag{5.14}$$

The magnitude of multi-particle lift force is calculated as:

$$F_L = 3\pi\eta_f d_p \overline{F}_{L,\phi}|\mathbf{v}_f - \mathbf{v}_i| \tag{5.15}$$

Hydrodynamic torque considered in this chapter is a pitching torque, acting around the axis perpendicular to the plane of relative fluid velocity $\mathbf{v}'_{fi}$ and particle orientation vector $\mathbf{u}_i$. Hence, the torque orientation vector $\hat{\mathbf{e}}_{T_0}$ is given by

$$\hat{\mathbf{e}}_{T_0} = \frac{\mathbf{v}'_{fi} \cdot \mathbf{u}_i}{\left|\mathbf{v}'_{fi} \cdot \mathbf{u}_i\right|} \frac{\mathbf{v}'_{fi} \times \mathbf{u}_i}{\left|\left|\mathbf{v}'_{fi} \times \mathbf{u}_i\right|\right|} \tag{5.16}$$

The resultant torque is then expressed as $\mathbf{T}_p = T_p \hat{\mathbf{e}}_{T_0}$.

Single particle hydrodynamic torque. The magnitude of the hydrodynamic torque on an isolated particle is calculated as proposed by Zastawny et al. [2]

$$T_P = \frac{1}{2} C_T \rho_f \frac{\pi}{8} d_p^3 \left|\mathbf{v}_f - \mathbf{v}_i\right|^2 \tag{5.17}$$

where C_T is the torque coefficient calculated using Zastawny et al. correlation:

$$C_{T,\alpha} = \left(\frac{c_1}{\mathrm{Re}^{c_2}} + \frac{c_3}{\mathrm{Re}^{c_4}}\right) \sin(\phi)^{c_5 + c_6 \mathrm{Re}^{c_7}} \cos(\phi)^{c_8^Z + c_9^Z \mathrm{Re}^{c_{10}^Z}} \tag{5.18}$$

Lift		**Torque**	
Coefficient	Value	Coefficient	Value
b_1	1.884	c_1	-2.283
b_2	0.1324	c_2	-0.01145
b_3	0.001668	c_3	4.09
b_4	-0.8159	c_4	-0.01395
b_5	0.8562	c_5	0.3406
b_6	0.003624	c_6	0.3609
b_7	0.6598	c_7	0.1355
b_8	-0.2621	c_8	0.2356
b_9	0.8021	c_9	0.3612
b_{10}	0.04384	c_{10}	0.1358

Table 5.2: Coefficients for the lift and torque correlations with the functional form of Zastawney *et al.* [2] fitted for spherocylinder particles with aspect ratio of 4 using in-house DNS simulations [3].

Multi-particle hydrodynamic torque. The magnitude of multi-particle hydrodynamic torque proposed by Sanjeevi et al. [5] is calculated as:

$$T_P = 2\pi\eta_f d_p^2 \overline{T}_{P,\phi}|\mathbf{v}_f - \mathbf{v}_i| \tag{5.19}$$

Coefficients	$T_{\mathrm{Re},\epsilon_s}$
a	0.82
b	1.44
c	1.07
d	5.48
e	0.223

Table 5.3: Coefficients for torque calculation (Eq. 5.22) as proposed by Sanjeevi et al. [5]

where $\overline{T}_{P,\phi}$ is average hydrodynamic torque for multi-particle system, calculated by Sanjeevi et al. correlation:

$$\overline{T}_{P,\phi}(\mathrm{Re},\epsilon_s,\phi) = T_{P,\mathrm{mag}}(\mathrm{Re},\epsilon_s)\sin\phi\cos\phi \tag{5.20}$$

with

$$T_{P,\mathrm{mag}}(\mathrm{Re},\epsilon_s) = T_{p,\mathrm{isol}}(\mathrm{Re})\cdot(1-\epsilon_s)^2 + T_{\mathrm{Re},\epsilon_s}(\mathrm{Re},\epsilon_s) \tag{5.21}$$

$$T_{\mathrm{Re},\epsilon_s}(\mathrm{Re},\epsilon_s) = \mathrm{Re}^a{\epsilon_s}^b\left(c(1-\epsilon_s)+\frac{d{\epsilon_s}^3}{(1-\epsilon_s)}\right) + e\epsilon_s(1-\epsilon_s)^2\mathrm{Re} \tag{5.22}$$

Coefficients for equation 5.22 are given in Table 5.3.

5.3. SIMULATION PARAMETERS

Simulations were done for a rectangular fluidized bed, whose dimensions are the same as in previous magnetic particle tracking (MPT) experiments [8] and numerical investigation [70]. The column dimensions and main parameters necessary for the CFD-DEM simulation are presented in Table 5.4. The particles used in this investigation are capsule-like spherocylinders with aspect ratio of 4. The minimum fluidization velocities were determined experimentally [8] and particle properties are listed in Table 5.5.

The standard practice for choosing the grids size in CFD-DEM simulations for spherical particles is that the grid dimensions should be between $1.6d_p$ and $5d_p$ [39, 61]. For the particle and column dimensions used in this chapter a grid size of $2.83d_p$ was applied, where d_p is the diameter of a volume equivalent sphere. This grid size satisfies both standard practice for spherical particles and offers a cell size larger than the length of the spherocylindrical particle [70].

5.4. RESULTS

We will investigate the distributions of particle orientation and particle velocity along the vertical (z-)axis for two different inlet gas velocities ($1.6\mathrm{U_{mf}}$ and $2\mathrm{U_{mf}}$). Two simulation cases will be compared, the first with single particle (SP) correlations and the second with multi-particle (MP) correlations. For the SP case, the general Hölzer-Sommerfeld drag equation, with a simple correction for the multi-particle effect, is used. This is the

CFD parameters

Parameter	Symbol	Value
Reactor base	L_x, L_y	0.15 m, 0.15 m
Reactor height	H_z	1.05 m
Number of grid cells	n_x^g, n_y^g, n_z^g	$10 \times 10 \times 70$
Grid cell dimensions	$c_x = c_y = c_z$	0.015 m
Time step	t_{CFD}	$1 \text{ x } 10^{-4}$ s
Fluid density	ρ_f	1.2 kg/m^3
Fluid viscosity	η_f	$1.568 \cdot 10^{-5}$ Pa·s

DEM parameters

Parameter	Symbol	Value
Time step	t_{DEM}	1×10^{-5} s
Coefficient of friction	μ	0.46
Cofficient of rolling friction	μ_r	0.46
Coefficient of restitution	e	0.43

Table 5.4: Relevant parameters for the CFD-DEM algorithm.

Particles

Parameter	Value
Number of particles	32500
Particle length [L]	12 mm
Particle diameter [2R]	3 mm
Particle density	1442 kg/m^3
Minimum fluidization velocity [U_{mf}]	1.7 m/s

Table 5.5: Particle properties.

Case	Drag force	Lift force	Torque
SP-correlations	Hölzer-Sommerfeld [120] + Di Felice [58]	Zastawny et al. [2]	Zastawny et al. [2]
MP-correlations	Sanjeevi et al. [5]	Sanjeevi et al. [5]	Sanjeevi et al. [5]

Table 5.6: Correlations applied for single particle (SP) correlations and multi-particle (MP) correlations.

most common approach found in literature to deal with hydrodynamic forces on non-spherical particles in dense systems. Table 5.6 lists correlations applied in each case. The simulation results are compared with experimental results presented in Chapter 4 using magnetic particle tracking (MPT) technique [8]. More technical information about the MPT experimental technique can be found in the work by Buist et al. [67].

5.4.1. PARTICLE ORIENTATION

In this section we analyze the average particle orientation in the terms of the z-component of the particle orientation vector **u**. Figure 5.1 shows the time averaged distribution of the particle orientation relative to the z-axis (direction of the fluid flow). If $|\mathrm{u_z}| = 0$, the particle has a horizontal orientation and is perpendicular to the fluid flow, while for $|\mathrm{u_z}| = 1$, the particle is oriented vertically and is fully aligned with the fluid flow. Note that for fully randomly oriented particles, the expected distribution of $|u_z|$ is flat.

From Fig. 5.1 it can be seen that multi-particle correlations show slightly better agreement with experimental results compared to single particle correlations. This is specifically the case for predicting the fraction of particles oriented vertically ($|\mathrm{u_z}|$ close to 1). However in some regions, specifically for $|\mathrm{u_z}|$ around 0, single particle correlations show better agreement with the experimental results. The difference between MP and SP correlations is considerably larger for $|\mathrm{u_z}|$ near 1 then near 0 and it can be observed that the difference between MP correlations and MPT experiments for horizontally oriented particles is less notable than the over-prediction of the fraction of particles oriented vertically in case of SP correlations compared to MPT experiments.

Figure 5.1 (b) shows that an increase in fluid velocity leads to an increase of the fraction of vertically aligned particles and a reduction of horizontally aligned particles. The difference between MP and SP correlations is also considerably smaller for $2U_{mf}$ compared to $1.6\mathrm{U_{mf}}$, but the same conclusions still apply.

Figures 5.2 and 5.3 give more insight into the preferred particle orientation in different parts of the fluidized bed. The preferred particle orientation is determined based on the particle orientation tensor **S**, calculated using the expression

$$\mathbf{S} = \begin{bmatrix} \langle u_x^2 \rangle & \langle u_x u_y \rangle & \langle u_x u_z \rangle \\ \langle u_y u_x \rangle & \left\langle u_y^2 \right\rangle & \langle u_y u_z \rangle \\ \langle u_z u_x \rangle & \langle u_z u_y \rangle & \langle u_z^2 \rangle \end{bmatrix}. \tag{5.23}$$

The diagonal components of this tensor can be used to determine the preferred alignment in the reactor. If the difference between the diagonal components is less than 0.1 i.e. $\left|\langle u_x^2\rangle - \langle u_y^2\rangle\right| < 0.1$, $\left|\langle u_x^2\rangle - \langle u_z^2\rangle\right| < 0.1$ and $\left|\langle u_y^2\rangle - \langle u_z^2\rangle\right| < 0.1$, the particle is consid-

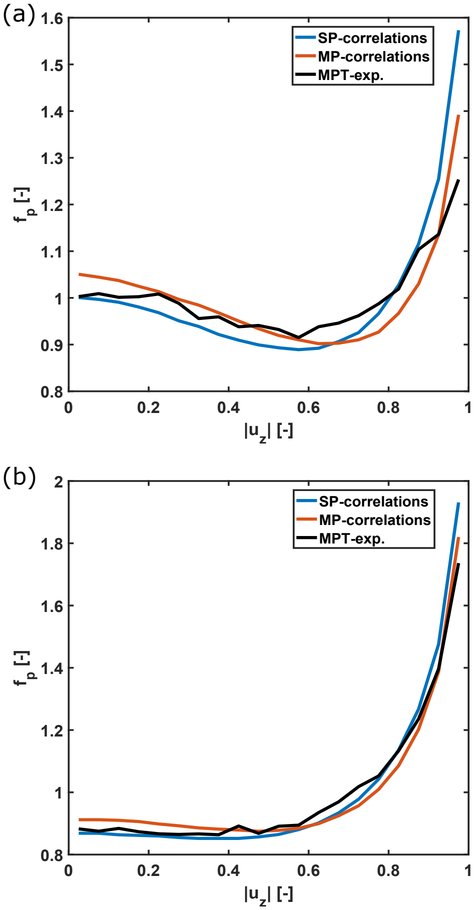

Figure 5.1: Probability distribution function for the particle orientation at (a) $1.6U_{mf}$ and (b) $2U_{mf}$. Simulations with single (SP) and multi (MP) particle correlations are compared with MPT experiments.

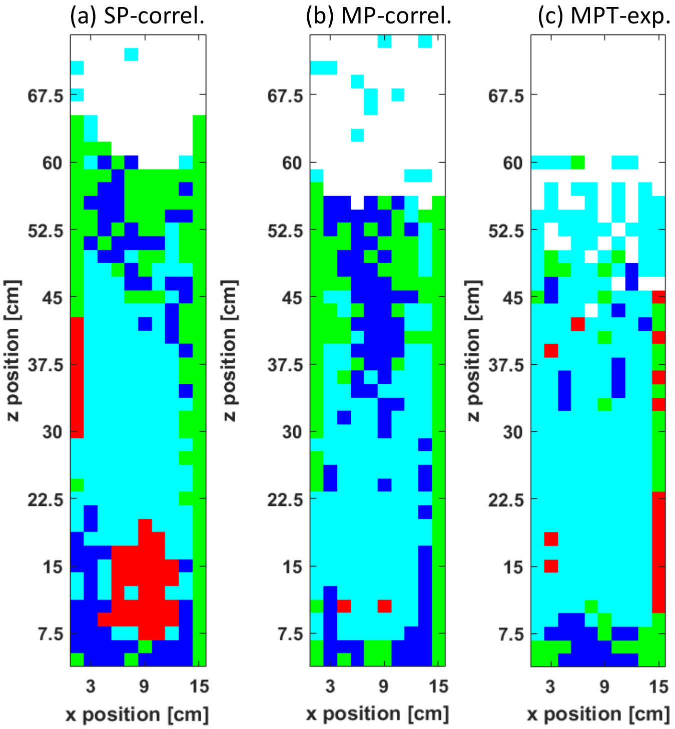

Figure 5.2: Preferred orientation of particles in the grid cells of the reactor for (a) single-particle (b) multi-particle correlations and (c) experimental results at $1.6U_{mf}$. Here the colour scheme is: blue squares (🟦) are *x*-aligned, green squares (🟩) are *y*-aligned, red squares (🟥) are *z*-aligned and cyan squares (🟦) are randomly orientated. White space represents empty cells.

ered to be randomly oriented. On the other hand, if one component is considerably larger than the other two components, we conclude that the particle is preferentially aligned with the corresponding axis. Figures 5.2 and 5.3 show time-averaged preferred particle orientation in the x-z plane for a cross section cutting through the center of the bed in the y-direction (6 cm ≤ y ≤ 7.5 cm).

From figures 5.2 and 5.3, the improved prediction of particle orientation by multi-particle correlations becomes more evident. Looking at the lower part of the column (z-position ≤ 30 cm) it is clear that MP correlations show better agreement with experimental results and that SP correlations over-predict the amount of regions in which particles are preferably oriented vertically. With an increase of the fluid velocity (Fig. 5.3) there is an increase in the amount of regions where particles preferably align vertically, in the lower part of the bed (z-position ≤ 30 cm) and in the wall region. From Figure 5.3 it can still be inferred that MP correlations have better agreement with experimental results in the lower part of the bed and in the wall region. In the case of single-particle correlations (Fig. 5.3 (a)), in the lower part of the bed the over-prediction of particles oriented vertically is noticeable, but also in the higher parts, near walls the SP results differ from the experimental results more than in case of MP correlations.

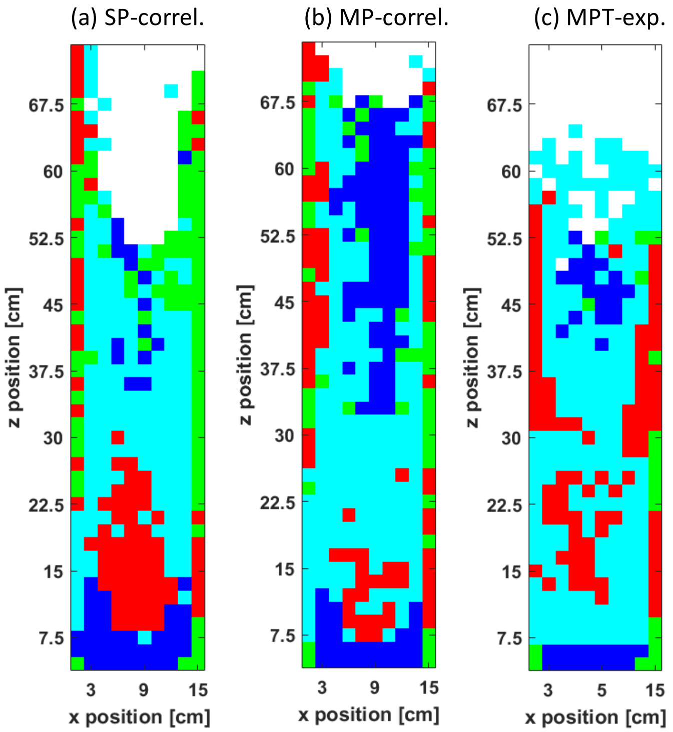

Figure 5.3: Preferred orientation of particles in the grid cells of the reactor for (a) single-particle (b) multi-particle correlations and (c) experimental results at $2U_{mf}$. Here the colour scheme is: blue squares (🟦) are *x*-aligned, green squares (🟩) are *y*-aligned, red squares (🟥) are *z*-aligned and cyan squares (🟦) are randomly orientated. White space represents empty cells.

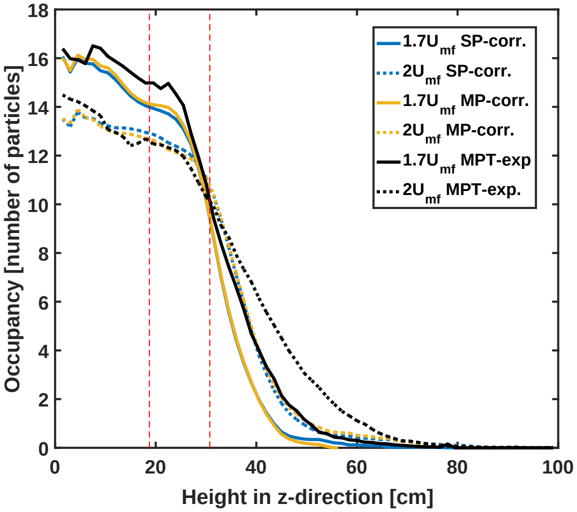

Figure 5.4: Average cell occupancy along the height in z-direction. The dashed red lines indicate the positions along the z-axis used for the sampling of v_z profiles in section 5.4.3.

In the higher parts of the bed (z-position > 30 cm), Figures 5.2 and 5.3, show that the simulations results predict a higher preference for the particles to orient horizontally, compared to the experimental results where particles are more randomly oriented. This is more evident in the case of MP correlations, particularly at the gas velocity of 2U$_{\text{mf}}$ (Fig. 5.3 (b)). In this region, the single-particle correlations show better agreement with experimental results.

However, as can be seen in Figure 5.4, above 30 cm in the z-direction the average cell occupancy is dropping dramatically and above 40 cm there is on average less than 1 particle per cell. The region above the height of 30 cm can therefore be considered as the free-board region, where the crowding effect is considerably lower compared to the dense fluidized region below 30 cm. It should also be noted that in the free-board region, the average occupancy predicted by the simulations in all cases starts to differ from the experimental results.

5.4.2. EFFECT OF LIFT FORCE AND HYDRODYNAMIC TORQUE ON PARTICLE ORIENTATION

In Chapter 2, we have investigated the effects of single-particle shape induced lift force and hydrodynamic torque on the particle orientation [70]. We have shown that hydrodynamic torque has a major effect on the particle orientation and leads to a change of preferred particle orientation from vertical to more horizontal. Here we extend the analysis to multi-particle (MP) correlations and make a detailed comparison with experimental results. In detail, we will compare the simulation results of cases using the Sanjeevi et al. [5] multi-particle correlations considering: 1. drag force only (D), 2. drag force and shape induced lift force (D + L), 3. drag force and hydrodynamic torque (D+T) and 4.

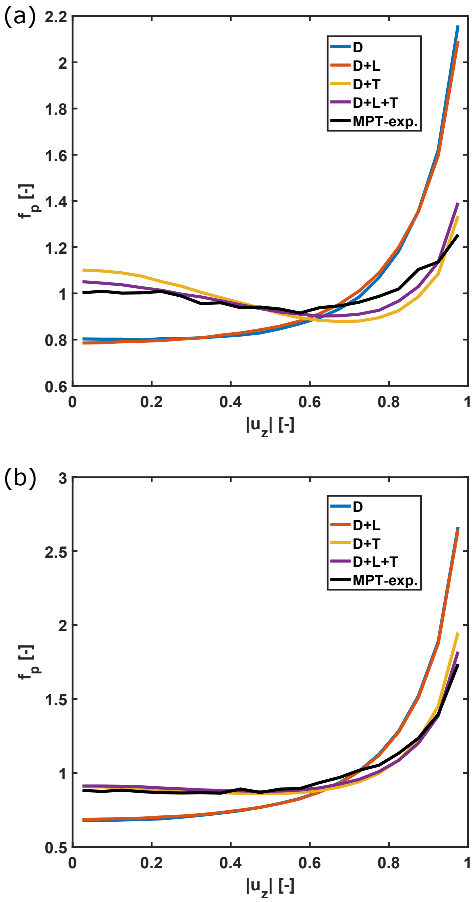

Figure 5.5: Preferred particle orientation at (a) $1.6U_{mf}$ and (b) $2U_{mf}$. Variation of $f_p(|u_z|)$ for simulations with differing hydrodynamic force conditions and from experimental results.

drag force with lift force and hydrodynamic torque (D+L+T), to the experimental MPT results. Figure 5.5 shows the time-average fraction of particles with a certain orientation to the z-axis.

It is clear that cases where hydrodynamic torque is not considered show a strong preference for particles to align with the fluid flow and that they are not at all representing what is observed in experimental results. Including hydrodynamic torque reduces the fraction of particles oriented vertically and leads to randomization of particle orientations but also to a considerable increase of particles that are oriented horizontally, perpendicular to the direction of the fluid flow. The simulations in which hydrodynamic torque is considered are almost perfectly matching the results obtained from the experiments. Note that including lift in addition to torque increases the agreement some more, but the effect is relatively small. Finally, as mentioned before, an increase of gas velocity leads to an increase of the fraction of particles oriented vertically while reducing the

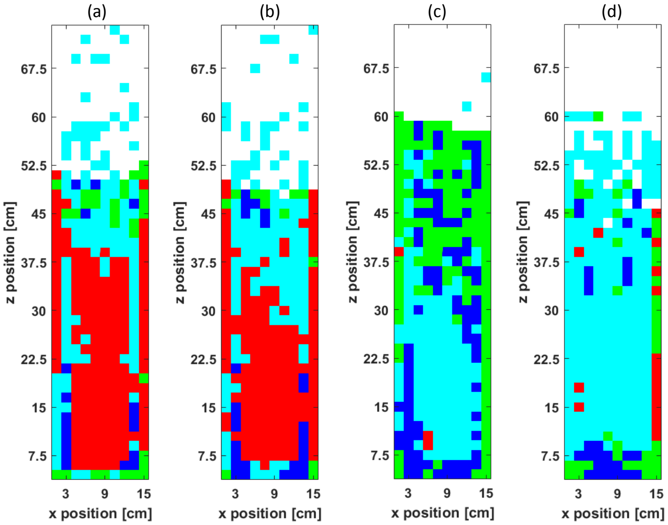

Figure 5.6: Preferred orientation of particles in the grid cells of the reactor for case with (a) drag force only (b) drag and lift force (c) drag and lift force and hydrodynamic torque, and (d) MPT experiments, at $1.6U_{\mathrm{mf}}$. Here the colour scheme is: blue squares (🟦) are x-aligned, green squares (🟩) are y-aligned, red squares (🟥) are z-aligned and cyan squares (🟦) are randomly orientated. White space represents empty cells.

fraction of particle oriented horizontally.

Figures 5.6 and 5.7 show the time-averaged preferred particle orientation in the z-x plane for a cross section in cutting through the center of the bed (as explained in the section 5.4.1) for cases with different multi-particle hydrodynamic forces considered and the ones obtained experimentally. It can be seen that including hydrodynamic torque leads to randomization of the particle orientation in the middle section of the bed but also to a considerable increase of horizontally oriented particles in the free-board region. Even though hydrodynamic torque has the biggest effect on particle orientation, Figures 5.2 and 5.3 show that actually cases where both lift force and hydrodynamic torque are considered have the best agreement with experimental results.

5.4.3. PARTICLE VELOCITY ALONG Z-AXIS

The particle velocity along the vertical direction (z-axis) is sampled at two bed heights, as indicated in Figure 5.4. The lower position in the bed ($z = 18.75$ cm) corresponds to dense fluidizing conditions, while the higher position ($z = 30.75$ cm) corresponds to the free-board region where the particle flow is getting more diluted and the agreement between simulation and experimental results in terms of average occupancy is still good. The time averaged z-velocities are presented along x-axis in the plane cutting through the center of the bed ($6\,\mathrm{cm} \leq y \leq 7.5\,\mathrm{cm}$). Particle velocities are weighted by the number of particles in the cell at each time step , i.e. they are a measure for the average solids flux.

Figure 5.8 shows the time averaged particle z-velocities at two positions in the bed

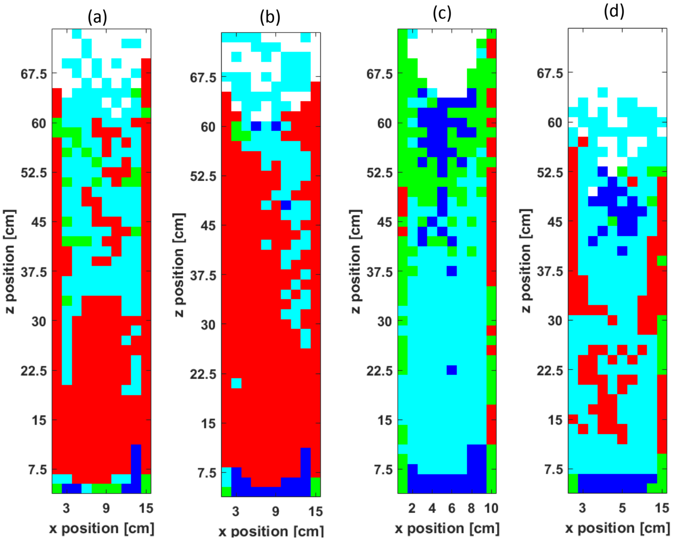

Figure 5.7: Preferred orientation of particles in the grid cells of the reactor for case with (a) drag force only (b) drag and lift force (c) drag and lift force and hydrodynamic torque, and (d) MPT experiments, at $2U_{mf}$. Here the colour scheme is: blue squares (🟦) are x-aligned, green squares (🟩) are y-aligned, red squares (🟥) are z-aligned and cyan squares (🟦) are randomly orientated. White space represents empty cells.

and at two inlet gas velocities. A considerable difference between SP and MP correlations can be seen in all cases. It is clear that single-particle correlations over-predict the particle z-velocities and that multi-particle correlations show much better agreement with the experimental results. At the higher position in the bed ($z = 30.75\,\mathrm{cm}$) and for the lower gas velocity of $1.6U_{mf}$, over-prediction of the vertical solids velocity can be seen for both SP and MP correlations. This can be caused by the more diluted particle flow at this position. As discussed in section 5.4.1, in the free-board region MP correlations can give less accurate predictions. With an increase of gas velocity to $2U_{mf}$, the particle flow gets denser at the higher position in the bed and again MP correlations show much better agreement with experimental results than SP correlations.

5.5. Conclusion

In this chapter, we applied CFD-DEM simulations to look into the effect and importance of multi-particle correlations for hydrodynamic forces and torque. Simulation results were compared to the results obtained using magnetic particle tracking (MPT) experiments. Multi-particle correlations considerably improved prediction of average particle orientation and its distribution throughout the fluidized bed, in dense fluidizing conditions. Usage of single-particle correlations leads to over-prediction of the number of particles that align vertically in the lower part of the fludized bed. On the other hand, multi-particle correlations over-predict the number of particles that orient horizontally in the free-board region. Comparing to experimental results, this over-prediction in the

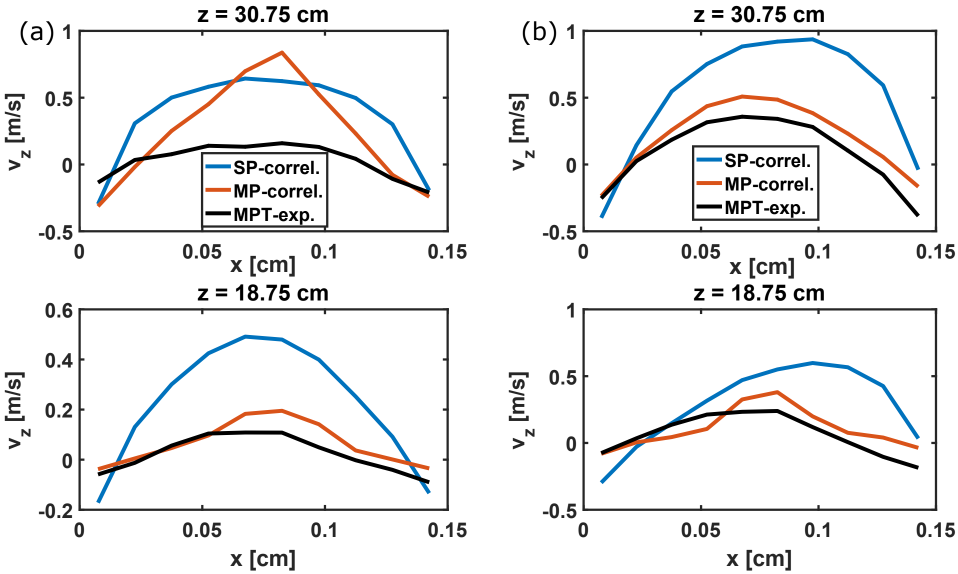

Figure 5.8: Comparison of the temporally-averaged vertical solids velocity v_z along the x-axis at two bed heights and at (a) $1.6\mathrm{U_{mf}}$ and (b) $2\mathrm{U_{mf}}$.

free-board region is encountered in simulations with single-particle correlations too, however to a smaller extent. Simulations with multi-particle correlations also show better agreement with experimental results in dense fluidizing conditions concerning the particle velocity in the vertical direction. Using single-particle correlations leads to considerable over-prediction of the particle velocities in all cases.

Even though single-particle correlations show better agreement with experimental results in the free-board region, during the fluidization process particles spend most of their time in dense fluidizing conditions and only small number of individual particles gets lifted in to the free-board region. This is why it is more important to get proper behavior of particles in the dense fluidizing conditions. We therefore expect that usage of multi-particle correlations will lead to considerable improvement in simulation of elongated particle fluidization.

6

SPHERICAL VERSUS ELONGATED PARTICLES - NUMERICAL INVESTIGATION OF MIXING CHARACTERISTICS IN A GAS FLUIDIZED BED

The possibility to offer good intermixing between particles is one of the main properties that make fluidized beds such an important industrial appliance. In this work, we use CFD-DEM simulations to compare mixing characteristics of spherical (AR-1) to elongated spherocylindrical particles (AR-4) of aspect ratio In simulation of AR-4 particles, single-particle and multi-particle correlations for hydrodynamic forces are tested. The results show that elongated particles have more vigorous intermixing and lower mixing times compared to spherical particles. Multi-particle correlations have a slight effect on particle mixing, and they increase the difference between AR-1 and AR-4 particles at higher gas velocities. Including hydrodynamic lift force and torque in the case of AR-4 particles leads to more vigorous mixing and lower mixing times.

Part of this chapter has been published in Chemical Engineering Science (2020) [127].

6.1. INTRODUCTION

In industry many processes rely on manipulation of solid granular materials suspended by a gas, such as gasification, drying, coating, food processing and gas phase polymerization. For this kind of application fluidized beds are irreplaceable equipment, offering high levels of contact between gas and solids together with high levels of intermixing between particles. The mechanism of particle mixing in fluidized bed is closely related to the bubble formation and motion [6, 125, 128].

Being such an important parameter for fluidization, the mixing characteristics of spherical particles, mostly A and B powders, have been subject of many numerical and experimental studies and are generally well understood [128–135]. Because many industrial processes use particles of non-spherical shape, recent years have witnessed an increase in development of numerical models for simulation of fluidized beds with non-spherical particles [7, 63, 136, 137]. Fluidization behavior of such particles is still not well understood, especially when it comes to fluidization in 3D fluidized beds. In our previous work we showed that elongated particles behave considerably different from spherical ones when suspended in gas flow [8, 70, 94] as they experience different particle-particle interactions together with additional hydrodynamic forces. Therefore findings that apply to spherical particles cannot be automatically assumed to be valid for elongated ones. So far, the only investigation that looked into mixing characteristics of non-spherical particles was done by Oschmann et al.[125]. Their work was the first that indicated a difference in mixing behavior between spherical particles and non-spherical particles of different aspect ratios. However, the exact cause of this different mixing behavior is not yet understood and needs more extensive research. Their work also did not take into account effects of lift force and hydrodynamic torque, both of which have proven to be important for accurately predicting the behavior of elongated particles in fluidized beds [70]. Recently, Sanjeevi and Padding (2020) [5] developed multi-particle correlations for drag and lift force and hydrodynamic torque for elongated particles of aspect ratio 4. These correlations take into account the effect of surrounding particles the so-called crowding effect on hydrodynamic forces and torque experienced by the particles. It is known that using multi-particle correlations leads to better predictions of the particles average orientation and average velocity in z-direction [118], however their effect on particle mixing is still not investigated.

In this work we, applied the CFD-DEM model, which was used and validated in previous works [7, 70], to compare mixing characteristics of spherical (AR-1) particles to elongated, spherocylindrical particles of aspect ratio 4 (AR-4) for different gas excess velocities. We will also show the importance of the effects of lift force and hydrodynamic torque on the mixing properties of elongated particles. We also investigate the effect of multi-particle correlations for hydrodynamic forces and torque and show the importance of the effects of lift force and hydrodynamic torque on the mixing properties of elongated (AR-4) particles.

6.2. NUMERICAL MODEL

For this study, we used a CFD-DEM algorithm based on open source CFDEM coupling [43]. This package couples two open source softwares, OpenFOAM which uses a CFD solver to solve the fluid equations and LIGGGHTS which solves particle equations using a discrete element method (DEM). These codes have been adapted so that they can deal with spherocylinders, without relying on a multi-sphere approach. More information about the model and it's validation can be found in previous works [7, 70].

6.2.1. HYDRODYNAMIC FORCES

The interaction between the fluid phase and solid particles in CFD-DEM is resolved trough closures for hydrodynamic forces. The main driving force for fluidization is the drag force and it is considered for both AR-1 and AR-4 particles, while lift force and hydrodynamic torque are considered only for AR-4 particles. For calculating hydrodynamic forces in case of AR-4 particles we applied two approaches: with single particle correlations and with multi-particle correlations. Correlations applied in different cases explored in this work are listed in Table 6.1.

	AR-1	AR-4	
		Single-particle	*Multi-particle*
Drag	Hölzer-Sommerfeld [120]	Hölzer-Sommerfeld [120]	Sanjeevi et al. [5]
Lift	-	Zastawny et al. [2]	Sanjeevi et al. [5]
Torque	-	Zastawny et al. [2]	Sanjeevi et al.[5]

Table 6.1: Correlations for hydrodynamic forces applied in this study.

Drag force. *Single-particle drag correlation* In the case of AR-1 particles and AR-4 particles with single-particle correlations, the drag force experienced by a particle is calculated using Di Felice's [58] modified drag force expression:

$$\mathbf{F}_D = \frac{1}{2} C_\mathrm{D} \rho_f \epsilon_f^{2-\chi} \frac{\pi}{4} d_p^2 \left|\mathbf{v}_f - \mathbf{v}_i\right| (\mathbf{v}_f - \mathbf{v}_i) \tag{6.1}$$

where $\mathbf{v}_f$ is the fluid velocity interpolated to the location of particle i, C_D is the drag force coefficient, d_p the volume-equivalent particle diameter, $\mathbf{v}_i$ is the velocity of particle i and χ is the Di Felice correction factor given by

$$\chi = 3.7 - 0.65 \exp\left[(-(1.5 - \log(\mathrm{Re}))^2/2\right] \tag{6.2}$$

where the particle Reynolds number Re is calculated as $\mathrm{Re} = \rho_f d_p \left|\mathbf{v}_f - \mathbf{v}_i\right| / \mu_f$ with ρ_f being the fluid density and μ_f the fluid viscosity. The Di Felice drag force expression was developed to take into account the effect of surrounding particle (crowding effect) on the drag force experienced by a particle. Even though it was originally developed for spherical particles, the Di Felice expression continued to be applied in simulations of elongated particles fluidization [7, 63, 65, 125, 126] because it was until recently the only option for approximating the crowding effect. Comparison between the effects of the Di

Felice approximation and a few other more recently developed models for approximating the crowding effect on drag force can be found in the work by Mahajan et al. (2018) [7].

Even though the Di Felice expression was applied, because the drag force coefficient is calculated using the single particle, Hölzer and Sommerfeld [120] correlation, simulations with AR-4 particles done using this approach are considered as single-particle cases. The Hölzer and Sommerfeld correlation can be applied to arbitrary shaped particles where the shape of the particle is taken into account through sphericity, and lengthwise and crosswise sphericity:

$$\mathrm{C_D} = \frac{8}{\mathrm{Re}}\frac{1}{\sqrt{\Phi_\parallel}} + \frac{16}{\mathrm{Re}}\frac{1}{\sqrt{\Phi}} + \frac{3}{\sqrt{\mathrm{Re}}}\frac{1}{\Phi^{3/4}} + 0.42 \times 10^{0.4(-\log\Phi)^{0.2}}\frac{1}{\Phi_\perp} \tag{6.3}$$

here the particle Reynolds number Re_p is calculated using the expression defined after the equation 2.12. The particle sphericity (Φ), the lengthwise sphericity ($\Phi_\parallel$), and the crosswise sphericity ($\Phi_\perp$) are calculated as:

$$\Phi = \frac{6V_p^{2/3}}{A_p}\pi^{1/3} \tag{6.4}$$

$$\Phi_\perp = \frac{A_e}{A_{p,\perp}} \text{ where } A_{p,\perp} = \pi d_p^2 + d_p L_{rod}\sin\theta \tag{6.5}$$

$$\Phi_\parallel = \frac{2A_e}{A_p - A_{p,\parallel}} \text{ where } A_{p,\parallel} = \pi d_p^2 + d_p L_{rod}\cos\theta \tag{6.6}$$

where V_p is the volume of the particle, A_p is the surface area of the particle, and A_e is the cross-sectional area of the volume equivalent sphere. For a sphere $\Phi = \Phi_\parallel = \Phi_\perp = 1$.

The multi-particle correlation defined by Sanjeevi and Padding [5] calculates the drag force experienced by a particle as:

$$\mathbf{F}_D = 3\pi\eta_f d_p \overline{F}_{D,\phi}(\mathbf{v}_f - \mathbf{v}_i) \tag{6.7}$$

where $\overline{F}_{D,\phi}$ is the average drag (normalised by the drag on an isolated volume equivalent sphere) based on the particle orientation with respect to the fluid flow (ϕ). Sanjeevi et al. showed that the average drag $\overline{F}_D$ for different ϕ follows a sine-square interpolation for individual particles as well as assemblies [3, 5], where the average drag $\overline{F}_D$ for any ϕ can be calculated as:

$$\overline{F}_{D,\phi} = \overline{F}_{D,\phi=0^\circ} + (\overline{F}_{D,\phi=90^\circ} - \overline{F}_{D,\phi=0^\circ})\sin^2\phi \tag{6.8}$$

$\overline{F}_{D,\phi=0^\circ}$ and $\overline{F}_{D,\phi=90^\circ}$ are a function of Re and ϕ:

$$\overline{F}_D(\mathrm{Re},\epsilon_s) = F_{d,isol}\cdot(1-\epsilon_s)^2 + F_{\epsilon_s} + F_{\mathrm{Re},\epsilon_s} \tag{6.9}$$

The corresponding terms are as follows:

$$F_{d,isol}(Re) = C_{d,isol}\frac{\mathrm{Re}}{24} \tag{6.10}$$

where $C_{d,isol}$ is calculated as proposed by Sanjeevi et al. [3]:

$$C_{d,isol} = \left(\frac{a_1}{\mathrm{Re}} + \frac{a_2}{\mathrm{Re}^{a_3}}\right)\exp(-a_4\mathrm{Re}) + a_5(1-\exp(a_4\mathrm{Re})) \tag{6.11}$$

where the coefficients $(a_1 ... a_5)$ for parallel $(\phi = 0^o)$ and perpendicular $(\phi = 90^o)$ orientation are given in Table 6.2.

$$F_{\epsilon_s}(\epsilon_s) = a\sqrt{\epsilon_s}(1-\epsilon_s)^2 + \frac{b\epsilon_s}{(1-\epsilon_s)^2} \tag{6.12}$$

$$F_{\mathrm{Re},\epsilon_s}(\mathrm{Re},\epsilon_s) = \mathrm{Re}^c {\epsilon_s}^d\left(e(1-\epsilon_s) + \frac{f{\epsilon_s}^3}{(1-\epsilon_s)}\right) + g\epsilon_s(1-\epsilon_s)^2\mathrm{Re} \tag{6.13}$$

The coefficients for Equations 6.12 and 6.13 for parallel and perpendicular orientation are also given in Table 6.2. Even though the multi-particle correlation takes into account the effect of surrounding particles on the drag force experienced by a particle, sub-grid inhomogeneities such as channeling, which are known to occur in beds of elongated particles at velocities around $\mathrm{U_{mf}}$, are not taken into account by this correlation.

	$\overline{F}_{\mathrm{D}}$			$C_{d,isol}$	
Coefficient	$\phi = 0°$	$\phi = 90°$		$\phi = 0°$	$\phi = 90°$
a	2	3	a_1	24.48	31.89
b	11.3	17.2	a_2	3.965	5.519
c	0.69	0.79	a_3	0.41	0.229
d	0.77	3	a_4	0.0005	0.0032
e	0.42	11.12	a_5	0.15	1.089
f	4.84	11.12			
g	0	0.57			

Table 6.2: Coefficients for drag force calculation as proposed by Sanjeevi et al. [3],[5].

In case of AR-4 particles, next to drag force, lift force and hydrodynamic torque are also considered. Their effect on the fluidization characteristics of AR-4 particles has been studied in chapter 2.

Lift force. *Single-particle lift correlation* The magnitude of the shape induced lift force F_L experienced by an isolated particle is expressed as

$$F_L = \frac{1}{2}C_L\rho_f\frac{\pi}{4}d_p^2\left|\mathbf{v}_f - \mathbf{v}_i\right|^2 \tag{6.14}$$

where C_L is the lift force coefficient. As the lift force is perpendicular to fluids relative velocity $\mathbf{v}'_{fi} = \mathbf{v}_f - \mathbf{v}_i$ and lies in the plane defined by the particle long axis orientation vector $\mathbf{u}_i$ and $\mathbf{v}'_{fi}$, the lift force magnitude F_L is multiplied by the lift force orientation vector $\hat{\mathbf{e}}_{L_0}$ which is given as

$$\hat{\mathbf{e}}_{L_0} = \frac{\mathbf{u}_i \cdot \mathbf{v}'_{fi}}{\left|\mathbf{u}_i \cdot \mathbf{v}'_{fi}\right|}\frac{(\mathbf{u}_i \times \mathbf{v}'_{fi}) \times \mathbf{v}'_{fi}}{\left\|(\mathbf{u}_i \times \mathbf{v}'_{fi}) \times \mathbf{v}'_{fi}\right\|} \tag{6.15}$$

The resultant lift force experienced by a particle is then expressed as $\mathbf{F}_L = F_L \hat{\mathbf{e}}_{L_0}$. The lift force coefficient is approximated using the correlation by Zastawny et al. [2]

$$\mathrm{C}_{L,\alpha} = (\frac{b_1}{\mathrm{Re}^{b_2}} + \frac{b_3}{\mathrm{Re}^{b_4}}) \sin(\alpha)^{b_5 + b_6 \mathrm{Re}^{b_7}} \cos(\alpha)^{b_8 + b_9 \mathrm{Re}^{b_{10}}} \tag{6.16}$$

Fitting coefficients used for the correlation can be found in Table A.1

Multi-particle lift correlation. Sanjeevi and Padding. [5] proposed a simplified calculation for shape induced lift force at different inclination angles ϕ, based on its relation to the normalized drag force. The average lift force $\overline{\mathrm{F}}_L$ (normalised by the drag on an isolated volume equivalent sphere) experienced in a multi-particle system at different ϕ is calculated as:

$$\overline{F}_{L,\phi} = (\overline{F}_{D,\phi=90^\circ} - \overline{F}_{D,\phi=0^\circ}) \sin\phi \cos\phi \tag{6.17}$$

The magnitude of multi-particle lift force is calculated as:

$$F_L = 3\pi \eta_f d_p \overline{F}_{L,\phi} |\mathbf{v}_f - \mathbf{v}_i| \tag{6.18}$$

Hydrodynamic torque. *Single-particle torque correlation.* The magnitude of the hydrodynamic torque on an isolated AR-4 particle is calculated as

$$T_P = \frac{1}{2} \mathrm{C_T} \rho_f \frac{\pi}{8} d_p^3 |\mathbf{v}_f - \mathbf{v}_i|^2 \tag{6.19}$$

where C_T is the torque coefficient. The hydrodynamic torque acts perpendicularly to the plane of particle relative velocity and particle orientation vector. Hence, the torque orientation vector $\hat{\mathbf{e}}_{T_0}$ is given by

$$\hat{\mathbf{e}}_{T_0} = \frac{\mathbf{v}'_{fi} \cdot \mathbf{u}_i}{\left|\mathbf{v}'_{fi} \cdot \mathbf{u}_i\right|} \frac{\mathbf{v}'_{fi} \times \mathbf{u}_i}{\left|\left|\mathbf{v}'_{fi} \times \mathbf{u}_i\right|\right|} \tag{6.20}$$

The resultant torque is then expressed as $\mathbf{T}_p = T_p \hat{\mathbf{e}}_{T_0}$. For approximating the torque coefficient we have also applied a correlation derived by Zastawny et al. [2]

$$C_{T,\alpha} = (\frac{c_1}{\mathrm{Re}^{c_2}} + \frac{c_3}{\mathrm{Re}^{c_4}}) \sin(\alpha)^{c_5 + c_6 \mathrm{Re}^{c_7}} \cos(\alpha)^{c_8^Z + c_9^Z \mathrm{Re}^{c_{10}^Z}} \tag{6.21}$$

The fitting coefficients used for calculating lift and torque coefficient have been derived by an in-house DNS simulations specifically for AR-4 spherocylindrical particles. More information about the DNS simulations can be found in [3, 32]. The coefficients used in this work are listed in Table A.1

Multi-particle torque correlation. The magnitude of the multi-particle torque proposed by Sanjeevi and Padding [5] is calculated as:

$$T_P = 2\pi \eta_f d_p^2 \overline{T}_{P,\phi} |\mathbf{v}_f - \mathbf{v}_i| \tag{6.22}$$

where $\overline{T}_{P,\phi}$ is the average hydrodynamic torque for a multi-particle system, calculated by:

Coefficients	$\mathrm{T}_{\mathrm{Re},\epsilon_\mathrm{s}}$
a	0.82
b	1.44
c	1.07
d	5.48
e	0.223

Table 6.3: Coefficients for torque calculation (Eq. 6.25) as proposed by Sanjeevi et al. [5]

$$\overline{T}_{P,\phi}(\mathrm{Re},\epsilon_\mathrm{s},\phi) = T_{P,\mathrm{mag}}(\mathrm{Re},\epsilon_\mathrm{s})\sin\phi\cos\phi \tag{6.23}$$

with

$$T_{P,\mathrm{mag}}(\mathrm{Re},\epsilon_\mathrm{s}) = T_{p,\mathrm{isol}}(\mathrm{Re})\cdot(1-\epsilon_\mathrm{s})^2 + T_{\mathrm{Re},\epsilon_\mathrm{s}}(\mathrm{Re},\epsilon_\mathrm{s}) \tag{6.24}$$

$$T_{\mathrm{Re},\epsilon_\mathrm{s}}(\mathrm{Re},\epsilon_\mathrm{s}) = \mathrm{Re}^a{\epsilon_\mathrm{s}}^b\left(c(1-\epsilon_\mathrm{s}) + \frac{d{\epsilon_\mathrm{s}}^3}{(1-\epsilon_\mathrm{s})}\right) + e\epsilon_\mathrm{s}(1-\epsilon_\mathrm{s})^2\mathrm{Re} \tag{6.25}$$

Coefficients for equation 6.25 are given in Table 6.3.

6.3. SIMULATION PARAMETERS

In this study we used a square fluidized bed which is the same as used in previous chapters 2,3 and 5. Column dimensions and main CFD-DEM simulation parameters are presented in Table 6.4. The parameters for particle properties are determined experimentally by Mahajan et al. (2018) [95] for particles made of alumide, a 3D printing material consisting of a mixture of nylon and aluminum dust. In this work we compare the fluidization mixing characteristics of spherical AR-1 particles to elongated, spherocylindrical AR-4 particles, using single-particle (SP) and multi-particle correlations (MP) (Table 6.1). In this work we compare the fluidization mixing characteristics of spherical AR-1 particles to elongated, spherocylindrical AR-4 particles. The considered particles are volume equivalent to each other as this allows us to compare beds of the same mass and same number of particles which also have relatively similar minimum fluidization velocity. The minimum fluidization velocities were determined experimentally [8] and particle properties are listed in Table 6.5.

In the initial bed, particles are separated by color in two layers, each containing the same number of particles, as shown in Fig. 6.1. In both layers the particles have identical properties, so the color distinction was made solely for tracking purposes. Horizontal or lateral mixing can be of interest in wide fluidized beds [125, 138] However this work refers to vertical mixing due to its higher relevance for tall beds.

Generally, in CFD-DEM simulations of spherical particles the recommended grid size is between $1.6d_p$ and $5d_p$. In this work we applied a grid size of $2.83d_p$ which allows us to satisfy standard practice for spherical particles and also have a cell size larger than the length of the AR-4 particle [70].

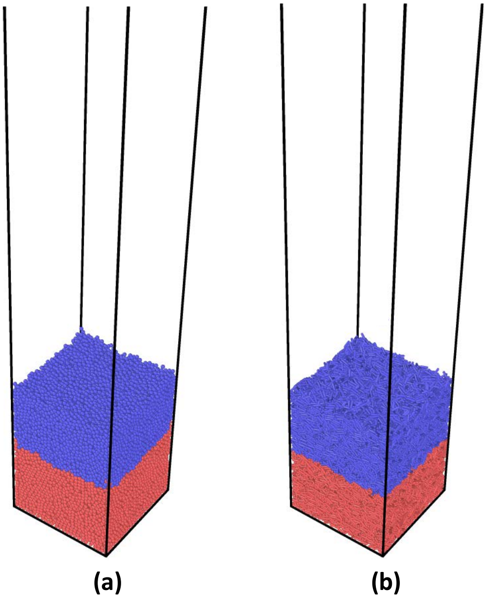

Figure 6.1: Initial beds for (a) AR-1 and (b) AR-4 particles.

CFD parameters

Parameter	Symbol	Value
Reactor base	L_x, L_y	0.15 m, 0.15 m
Reactor height	H_z	1.05 m
Number of grid cells	n_x^g, n_y^g, n_z^g	10 × 10 × 70
Grid cell dimensions	$c_x = c_y = c_z$	0.015 m
Time step	t_{CFD}	$1 \text{ x } 10^{-4}$ s
Fluid density	ρ_f	1.2 kg/m^3
Fluid viscosity	η_f	$1.568 \cdot 10^{-5}$ Pa · s

DEM parameters

Parameter	Symbol	Value
Time step	t_{DEM}	1×10^{-5} s
Coefficient of friction	μ	0.46
Cofficient of rolling friction	μ_r	0.46
Coefficient of restitution	e	0.43

Table 6.4: Relevant parameters for the CFD-DEM algorithm.

Particles

Parameter	AR-1	AR-4
Number of particles	32500	32500
Particle length [L]	-	12 mm
Particle diameter [2R]	5.3 mm	3 mm
Particle density	1442 kg/m^3	1442 kg/m^3
Minimum fluidization velocity [U_{mf}]	1.58 m/s	1.7 m/s

Table 6.5: Particle properties.

6.4. MIXING ENTROPY

Literature offers a number of methods to quantify the degree of particle mixing and they all have their advantages and disadvantages [139]. In fluidized bed investigations two approaches are most popular in recent research: the Lacy mixing index and mixing entropy. For this investigation we decided to focus on mixing entropy as it offers slightly smoother curves and the only parameter that needs to be considered carefully is the choice of the grid size used for measuring the particle fractions [139].
Calculating the mixing index, the domain is divided into grid cells indexed by triplets of integers (*i,j,k*). For each cell, the local mixing entropy is calculated using:

$$S(i,j,k) = -x_1(i,j,k)\ln(x_1(i,j,k)) - x_2(i,j,k)\ln(x_2(i,j,k)) \tag{6.26}$$

where $x_1(i,j,k)$ and $x_2(i,j,k)$ are number fractions of the colored particles in the cell under investigation.

Local mixing entropies are summed in order to obtain the total normalized mixing entropy (S_{tot}) for each time during the simulation.

$$S_{tot} = \frac{1}{S_0}\sum_{i,j,k} S(i,j,k)\cdot\frac{N_{cell}(i,j,k)}{N} \tag{6.27}$$

where S_0 is the maximum entropy of a randomly mixed system, which depends on the ratio of the number of the two types of particles in the system. For the 1:1 ratio used here, we have $S_0 = -\ln 1/2 = \ln 2$. In Eq. 6.27, we weigh each local mixing entropy with the number of particles $N_{cell}(i,j,k)$ in cell (*i,j,k*) to properly average the total mixing entropy.

When the size of the grid cell used for measuring the fractions is too small, the measurement of the mixing entropy is hampered by statistical noise. Conversely, when the size of the grid cell is too large, the spatial distribution of the particles is ignored. For the dimensions of fluidized bed considered in this work, dividing the domain in coarse grid of $5 \times 5 \times 35$ cells proved to be optimal for accurately determining the mixing entropy.

Mixing time. The mixing entropy gives valuable information on how mixing between particles progresses over time. This also enables us to estimate the mixing time for each case. The normalized mixing entropy varies between values of 0 and 1 for completely separated and perfectly mixed systems, respectively. Because in practice perfect mixing is never reached, in this work we use a value of 0.95 for the mixing entropy to define a sufficiently mixed system. The same approach was also applied by Deen et al. [134]. The mixing time $t_{95\%}$ is defined as the time at which the mixing entropy reaches a value of 0.95, as shown by a horizontal dashed line in Fig. 6.2.

6.5. RESULTS

In this section we present results on particle mixing in terms of mixing entropy and mixing time. We compare mixing characteristics of AR-1 to AR-4 particles at 6 different gas inlet velocities (1.6U$_{\mathrm{mf}}$, 1.7U$_{\mathrm{mf}}$, 2U$_{\mathrm{mf}}$, 2.3U$_{\mathrm{mf}}$, 2.6U$_{\mathrm{mf}}$ and 2.9U$_{\mathrm{mf}}$). For AR-4 particles we look into the effect of single-particle (SP) and multi-particle (MP) correlations, as well as considering hydrodynamic lift force and torque at 4 gas inlet velocities (1.6U$_{\mathrm{mf}}$, 1.7U$_{\mathrm{mf}}$, 2U$_{\mathrm{mf}}$ and 2.9U$_{\mathrm{mf}}$). All simulations were run for 20 seconds which for this size of fluidized bed is enough to reach statistical steady-state [70].

6.5.1. PARTICLE MIXING

Figure 6.2 shows mixing entropies as a function of time for AR-1 particles and AR-4 particles with single-particle and multi-particle correlations, under the influence of different gas velocities. It can be seen that varying the gas velocity between 1.6U$_{\mathrm{mf}}$ and 2U$_{\mathrm{mf}}$ leads to a considerable change in mixing entropy. This is particularly the case when changing from 1.6U$_{\mathrm{mf}}$ to 1.7U$_{\mathrm{mf}}$. However with an increase of gas velocity above 2U$_{\mathrm{mf}}$ no additional effect on the evolution of the mixing entropy can be noticed anymore. This can be observed for all considered cases. By comparing the mixing entropy curves for AR-4 particles, it can be seen that using single-particle or multi -particle correlations for hydrodynamic forces does not have a considerable effect on particle mixing. Hovewer, the difference in mixing entropy between AR-1 and AR-4 particles is more evident.

We now make a more quantitative comparison of mixing entropies for AR-1 and AR-4 particles for the two lower gas velocities 1.6U$_{\mathrm{mf}}$ and 1.7U$_{\mathrm{mf}}$ and the highest gas velocity 2.9U$_{\mathrm{mf}}$, as shown in Fig 6.3. Solid lines represent AR-4 particles while dashed lines represent AR-1 particles. Different gas velocities are distinguished by color.

From Fig. 6.3 clear differences between AR-1 and AR-4 particles can be observed for 1.6 and 1.7U$_{\mathrm{mf}}$ where AR-4 particles show considerably higher mixing entropy values and therefore more intensive mixing. This behavior was already observed by Oschmaan et al. [125]. However, at the highest considered gas velocity of 2.9U$_{\mathrm{mf}}$ the difference between mixing of the two types of particles is becoming negligible.

Condensing the mixing entropy curves into one value as mixing time ($t_{95\%}$), as explained in section 6.4, gives more insight in the comparison between AR-1 and AR-4 particles. Figure 6.4 shows the time necessary for a fluidized bed to reach a sufficiently mixed state, with a normalized mixing entropy value of 0.95, as a function of gas inlet velocity. Here the difference between AR-1 and AR-4 particles becomes even clearer. At higher gas velocities it can be noticed that even though differences in the mixing time between the two types of particles is getting lower, AR-4 particles continue to show lower mixing times. The effect of gas velocity on the mixing time is considerably higher for for AR-1 particles than for AR-4 particles in the range between 1.6U$_{\mathrm{mf}}$ and 2U$_{\mathrm{mf}}$. Choosing between single-particle or multi-particle correlations for AR-4 particle has only a slight effect on the mixing time. However, it can be noticed that MP correlations increase

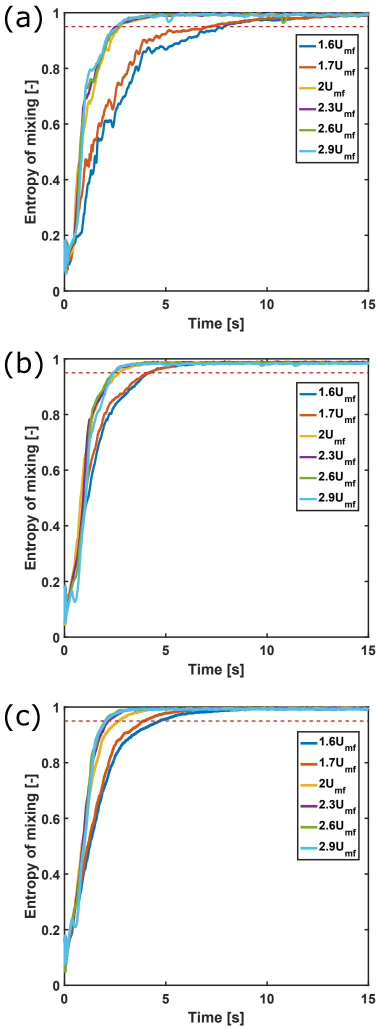

Figure 6.2: Mixing entropy as function of time for (a) AR-1 and (b) AR-4 particles.

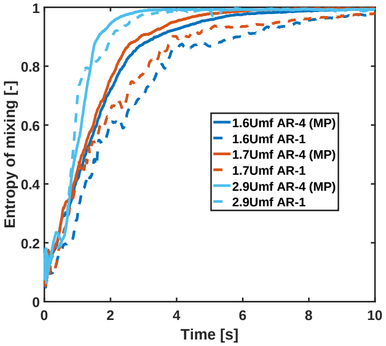

Figure 6.3: Comparison of mixing entropy as function of time for AR-1 and AR-1 particles at $1.6U_{mf}$, $1.7U_{mf}$ and $2.9U_{mf}$.

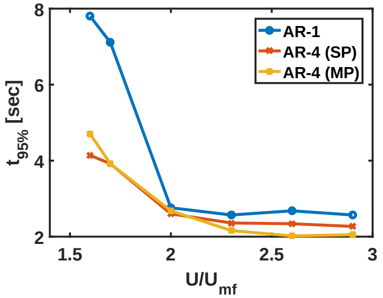

Figure 6.4: Mixing time as function of inlet gas velocity for AR-1 and AR-4 particles.

the difference in mixing time between AR-1 and AR-4 particle at higher gas velocities ($> 2U_{mf}$)

The previous work by Oschmann et al. [125] already reported less intensive mixing for spherical particles and for particles of lower aspect ratio. However the physical reason for this difference is still not clear. Figures 6.5 and 6.6 show visualization of fluidization of AR-1 and AR-4 particles at the lowest ($1.6U_{mf}$) and highest ($2.9U_{mf}$) gas velocities at different time instances. From Fig. 6.5 it is already visually clear that AR-1 particles show considerably less intensive mixing after a given amount of time. It seems that for the same gas velocity (U/U_{mf}), AR-4 particles have a higher bed expansion with more vigorous mixing, while AR-1 particles show distinct layers of the same particle colors. The reason for this can be that large (Geldart D type) AR-4 particles show more intensive turbulent fluidization behavior than volume equivalent AR-1 particles for the same gas velocity [94]. In our previous experimental investigation [94], we have shown that while AR-1 particles remain in a constant slugging regime, AR-4 particles show more turbulent behavior and periodically switch between slugging and turbulent fluidization.

As the bubbles are main carriers responsible for particle mixing in fluidized beds and the main mixing occurs in the bubble wake [6, 128], it is expected that fluidized beds with flat nose, raining slugs, that are characteristic for large Geldart D particles [6], cannot

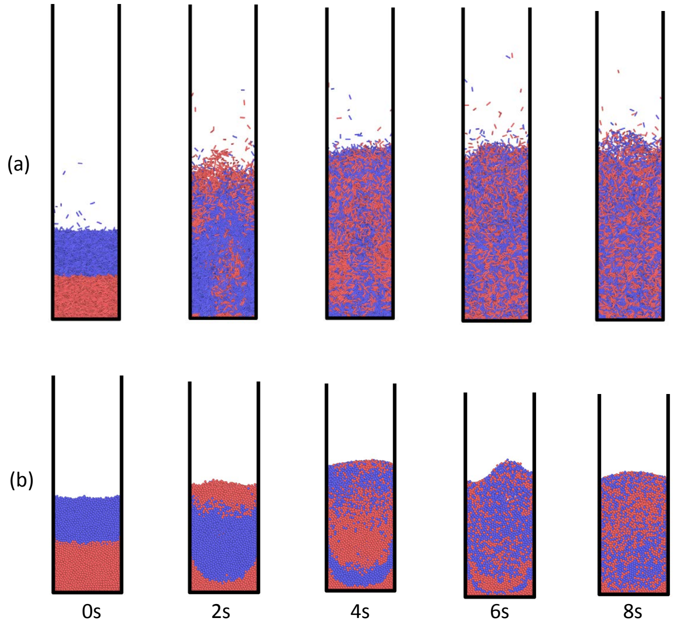

Figure 6.5: Visualization of fluidization at different time instants for (a) AR-4 and (b) AR-1 particles at $1.6U_{mf}$.

lead to as effective particle mixing as bubbling or turbulent fluidized beds.

From Fig. 6.6 it can be observed that at the highest gas velocity of 2.9Umf, AR-1 particles are also in a much more turbulent fluidizing regime, more similar to AR-4 particles. Figure 6.7 gives more insight in the void fraction distribution for the lower part of the bed ($z < 0.3$ m), where for all gas velocities we expect to be in the dense part of the fluidized bed. As void fractions between 0.4 and 0.5 respond to densely packed beds, and between 0.9 and 1.0 to cells with barely any particles in them, from figure 6.7 it can be seen that AR-1 particles generally show a much more binary distribution of void fractions (i.e. either very dense or very dilute) compared to AR-4 particles which show a much wider distributions in the middle range of void fractions. At the low gas velocity of $1.6U_{mf}$, AR-1 particles are still densely packed, with individual bubbles passing trough the bed and carrying out the mixing. While for AR-4 particles, even at such low gas velocities, the particles are more suspended in the gas flow, which can lead to faster mixing. This is more visually evident from the snapshots in figure 6.8. It can be seen that in the case of AR-1 particles, bubbles are clearly formed and the boundary between densely packed particles and gas bubbles is clearly visible. In the case of AR-4 particles, no clear bubbles are formed and particles are generally more suspended in the gas flow.

From figure 6.7 it can be seen that with the increase of gas velocity, there is an increase in the intermediate range of void fractions for AR-1 particles, however it still remains lower than in the case of AR-4 particles. AR-1 particles also show a higher peak at void fractions in the range 0.9-1.0, which still suggests that clear bubbles (or slugs) are passing through the bed. With the increase of gas velocity, the distribution of void frac-

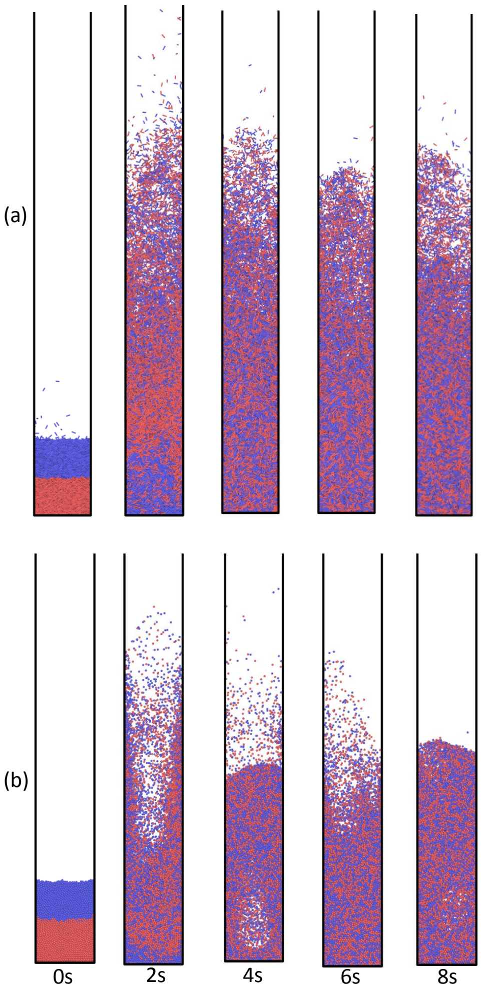

Figure 6.6: Visualization of fluidization at different time instants for (a) AR-4 and (b) AR-1 particles $2.9U_{mf}$.

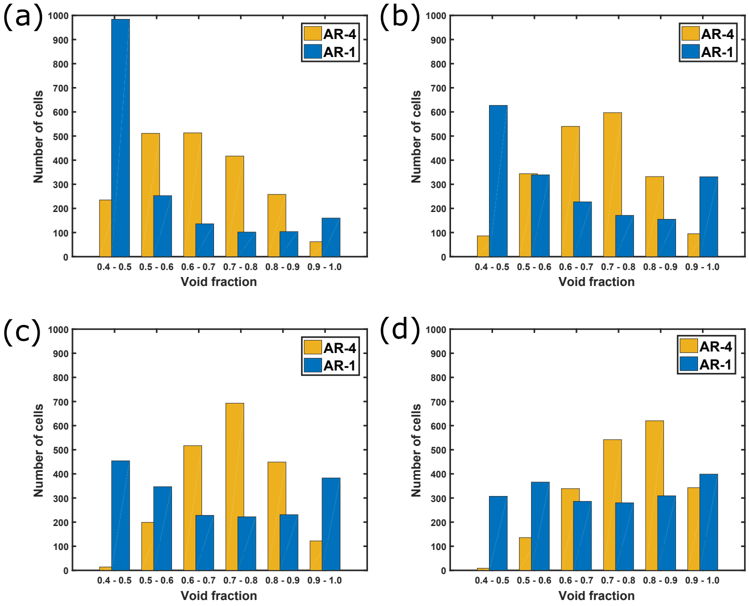

Figure 6.7: Histogram of void fractions for cells below z = 0.3 m (total of 2000 cells) for AR-1 and AR-4 (MP) particles at (a) 1.6U_{mf}, (b) 2U_{mf}, (c) 2.3U_{mf} and (d) 2.9U_{mf}.

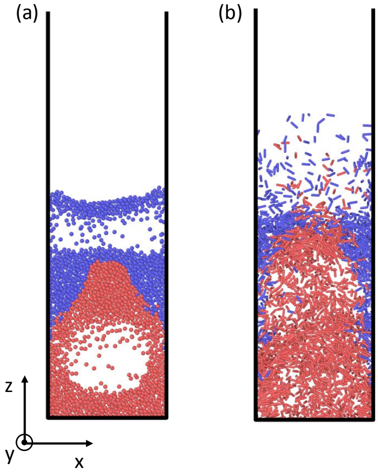

Figure 6.8: Snapshots of bubble formations for (a) AR-1 and (b) AR-4 (MP) particles at 1.7U_{mf} in the middle intersection of the bed (0.07 m ≤ y ≤ 0.08 m).

tions for AR-4 particles moves to the values corresponding to more dilute cells. Overall, these observations can explain the faster mixing times we observe in the case of AR-4 particles.

In chapter 4 we already started to see indications of transition to a turbulent fluidization regime for spherical particles at a gas velocity of $1.9U_{mf}$, which can explain the large drop in mixing time for AR-1 particles at $2U_{mf}$. This is consistent with our observation that above $2U_{mf}$ we see negligible difference between AR-1 and AR-4 particles, as both are operating in the turbulent fluidizing regime.

6.5.2. EFFECT OF HYDRODYNAMIC LIFT FORCE AND TORQUE ON MIXING CHARACTERISTICS OF ELONGATED PARTICLES

So far, most numerical works have neglected the effect of hydrodynamic lift and torque on fluidizaton of non-spherical particles. However, in case of elongated particles these forces have considerable effect on the average particle orientation and velocity distribution [70]. In this section we investigate the effect of considering lift and torque on mixing behavior of AR-4 particles. Figure 6.9 compares the mixing entropy and the mixing times for cases with only multi-particle drag force considered to cases where all hydrodynamic forces (using multi-particle correlations) are considered, for different gas velocities.

From Fig. 6.9 (a) it can be observed that cases with all hydrodynamic forces considered (full lines in Fig. 6.9) show higher mixing entropies than cases where only the drag force is considered (dashed lines in Fig. 6.9). This difference is diminishing with increasing gas velocity.

6

Similar behavior can be seen in the mixing time (Fig. 6.9 (b)) where for $1.6U_{mf}$, $1.7U_{mf}$ and $2U_{mf}$ simulations with lift and torque show lower mixing times. At the highest velocity of $2.9U_{mf}$ both cases have almost identical mixing times. The fact that after $2U_{mf}$ we do not see any effect of varying gas velocity (Fig. 6.3 and 6.4) or hydrodynamic forces on mixing properties indicates that we have reached a terminal mixing time and that for the considered properties of the fluidized bed (column and particle properties) it is not possible to achieve faster mixing. From the presented results it can be assumed that the terminal mixing times for AR-1 and AR-4 particles in the fluidzed bed considered in this work are around 2.6 and 2.3 seconds, respectively.

The effect of including lift and torque on mixing time can be attributed mainly to the lift force. Including hydrodynamic lift force leads to an increase in average particle velocity in the vertical z-direction [70]. As can be seen from the previous section 6.5.1, increasing gas velocity leads to faster and more intensive mixing.

6.6. CONCLUSION

In this chapter, we applied CFD-DEM simulations to compare mixing behavior of spherical (AR-1) particles to elongated spherocylinders (AR-4) in a fluidized bed and to investigate the effect of novel multi-particle correlations for hydrodynamic forces and torque [5] compared to widely used single-particle correlations. Spherical (AR-1) particles show less vigorous mixing than AR-4 particles and have higher mixing times. The largest difference can be seen for gas velocities up to $2U_{mf}$. At higher gas velocities, even though AR-1 particles still show longer mixing times, differences can be considered negligible.

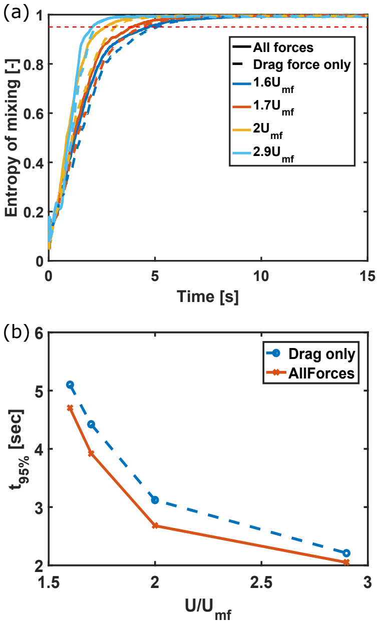

Figure 6.9: Effects of considering hydrodynamic lift and torque on (a) mixing entropy and (b) mixing time for AR-4 particles

This indicates that between $2U_{mf}$ and $2.3U_{mf}$ the fluidized bed already reaches a terminal mixing velocity and it is not possible to achieve faster mixing times for the given fluidized bed properties. More vigorous mixing for AR-4 particles can be explained by the more turbulent fluidization. These observations are characteristic of tall and narrow beds with coarse particles. Different conclusions are possible for shallower beds with lower bed height to column diameter ratios.

Applying multi-particle correlations for hydrodynamic forces and torque does not have a large effect on particle mixing times. It can be noted that the mixing times for cases with multi-particle correlations at higher gas velocities ($> 2.3U_{mf}$) have slightly lower mixing times compared to the cases with single particle correlations, however this effects can be seen as marginal.

Including hydrodynamic lift and torque has an effect on mixing properties of AR-4 particles and leads to somewhat faster mixing times. The main cause for faster mixing times can be seen in the effect of lift force which increases the particle average velocity in the vertical direction.

7

CONCLUSION

This thesis dealt with the specifics of elongated particles in fluidizing conditions including a comparison with fluidization of more usual spherical particles. This was done using a numerical approach, with CFD-DEM simulations, and an experimental approach, using magnetic particle tracking (MPT) and X-ray tomography (XRT). The main findings of this thesis are listed bellow:

- **Considering shape induced lift force and hydrodynamic torque is necessary for predictive simulation of elongated particle fluidization** In Chapter 2 we used CFD-DEM simulations to look at individual and joint effects of lift force and hydrodynamic torque on fluidization of elongated particles. Their most notable effect was seen in the particle velocity in the vertical direction and in the particle orientation. Including shape induced *lift force* in simulations led to an increase of the average vertical particle velocity, while it had a negligible effect on the average particle orientation. Considering *hydrodynamic torque* did not have a notable effect on the average particle velocity, however it had a strong effect on the particle preferred orientation. Including hydrodynamic torque changed the particle preferred orientation from more vertical to more horizontal, together with an increase of random particle orientation. In Chapter 6 we compared the average particle orientations from CFD-DEM simulations, with varying hydrodynamic forces and torque, to MPT experimental results. We have shown that it is of crucial importance to consider hydrodynamic torque in order to properly predict average particle orientations during fuidization of elongated particles. We can definitively say that considering both shape induced lift force and hydrodynamic torque is necessary to predictively simulate fluidization of elongated particles.

- **When fluidized, elongated particles mix faster than spherical particles.** In Chapter 6 we performed numerical investigation using CFD-DEM simulations of mixing characteristics of spherical and elongated particles. Looking at mixing entropies and mixing times for spherical and elongated particles at different gas velocities, we showed that elongated particles mix faster than spherical ones. Elongated particles showed faster mixing times at all gas velocities and at $1.6\mathrm{U}_{\mathrm{mf}}$ it was almost twice faster. At around $2\mathrm{U}_{\mathrm{mf}}$ both types of particles reached terminal mixing times and with further increase of gas velocity the difference was small and relatively constant, with elongated particles still showing slightly shorter mixing times. Including shape induced lift force and hydrodynamic torque in simulations of elongated particles, led to a decrease of mixing time. The faster mixing times observed in fluidization of elongated particles can be explained by the presence of more turbulent fluidization, discussed in Chapter 4.

- **Using multi-particle correlations for hydrodynamic forces and torque improves simulations of elongated particle fluidization.** In Chapter 6 we applied the newly developed multi-particle correlations for drag force, lift force and hydrodynamic torque and compared them to simulations with single particle correlations (supplemented with multi-particle corrections for spheres, as used in the literature so far). Comparing simulation results to the results from MPT experiments from Chapter 3 we showed that multi-particle correlations improved the prediction of particle orientation and particle velocity in z-direction, for dense regions of the bed. In the free-board region, simulations with single-particle correlations showed better agreement with experimental results. As a much smaller number of particles is affected by conditions in the free-board region, and predicting the correct behavior of particles in dense fluidizing conditions is therefore far more important, we argue that using multi-particle correlations improves simulations of elongated particle fluidization.

- **The amount of alignment and rotation of elongated particles depends on the aspect ratio.** In Chapter 3 we used magnetic particle tracking (MPT) experiments to compare fluidization of elongated particles with aspect ratios of 4 and 6. We found that AR-6 particles have a higher tendency to align with the fluid flow, which was most notable in the wall regions. The AR-6 particles also showed higher magnitudes of rotational velocity.

- **Elongated particles behave considerably different from spheres in fluidizaing conditions. Models and correlations developed for fluidization of spherical particles can not be translated to fluidization of elongated particles.** In Chapters 3 and 4 we used two different experimental techniques (MPT and XRT, respectively) to compare fluidization behavior between spherical and elongated particles (of equivalent volume). We found clear differences when looking at:
  - *Particle velocity distribution.* Using the MPT technique, we showed that spherical particles predominantly rise in the middle of the bed and descend next to the walls at all gas velocities investigated. Elongated particles showed completely different behavior and they display a separation in two counter-rotating vortices, in which the bottom vortex rises next to the walls and descends in the middle of the bed.
  - *Particle rotational velocity.* Spherical particles show the highest rotational velocities in the bulk region and near the walls, while elongated particles have

the highest rotational velocities in the free-board region.

- *Bubble and slugging properties.* Using XRT in Chapter 4 we showed that a fluidized bed of elongated particles has a considerably larger distribution of small and medium size bubbles compared to a bed of spherical particles. Elongated particles also showed higher average bubble velocities. In case of spherical particles, slugs appear with regular time intervals, unlike for elongated particles, which demonstrate a wide distribution of waiting times between slugs. The fluidized bed of spherical particles also shows a clear dominant slug frequency of 1 Hz, while elongated particles had a wider spread of frequencies, up to 2 Hz, without a clear distinct peak. All this indicates that elongated particles show more turbulent fluidization compared to spherical particles and that during fluidization they periodically switch between slugging and more turbulent fluidization.

7.1. RECOMMENDATIONS FOR FUTURE WORK

With this work we have deepened the understanding of elongated particles fluidization and presented the tools necessary for predictive modeling of their fluidization. Having addressed the main points in fluidization of elongated particles, this work can be the foundation for further development of models that can simulate fluidization with elongated particles encountered in real industrial conditions. First steps to do so would be:

- In industrial conditions, elongated biomass particles are usually fluidized in mixtures with inert materials which have particles of much smaller dimensions and more-or-less spherical shape. Now that we understand fluidization of elongated and spherical particles individually, the next step would be to see how their fluidization behavior changes in industrial mixtures. To do this, it is necessary to perform experimental investigations, where a good starting point would be PIV-DIA and particle tracking experiments.

- In order to perform CFD-DEM simulations of fluidization of industrial mixtures, it is necessary to develop hydrodynamic force and torque correlations for such mixtures. This will be challenging because the size ratios and mixture compositions add yet more parameters to the already long list of relevant parameters.

- Developing correlations that include near wall effects for dense and dilute flows of elongated particles could improve simulation results.

- In order to better understand the phenomenon of channeling, which is characteristic of elongated particles before they start to fluidize, it would be interesting to perform investigation of the force chains that appear in a bed of elongated particles for gas velocities below U_{mf}.

- In this work we performed XRT investigation of coarse elongated particles, where the ratio of column diameter to particle length was low. Performing a similar investigation in a bed with larger column diameter to particle length ratio may lead to different conclusions.

A

LIFT AND TORQUE COEFFICIENTS

In this study we explored the effect of varying lift and torque expressions on the dynamics of fluidized non-spherical particles. These expressions were derived for a single stationary particle in a particle flow at varying angles of incidence and Reynolds number using direct numerical simulations (DNS). Here the angle of incidence is defined as the angle between the direction of the fluid flow and the principal or longest axis of the non-spherical particle. For instance, in [3], the flow is modelled via the D3Q19 multi-relaxation time (MRT) lattice Boltzmann method (LBM).

The lift and torque correlation functions from the DNS investigations of [3] and [2] used in this study are presented in Table 2.1. Each function is comprised of a number of coefficients that have been obtained by fitting the correlation functions in Table 2.1 to data from direct numerical simulations. In the study of Zastawny *et al.* [2], these coefficients were calculated for ellipsoids, disc-shaped particles and fibres with an aspect ratio of 5. However these parameters are not applicable for the spherocylinders used in this study, which have an aspect ratio of 4. Therefore we use coefficients for L_{Zast} and T_{Zast} that have been fitted using in-house DNS simulations. For further information on the DNS simulations we refer the reader to [32] and [3]. The coefficients for the Zastawny lift and torque functions are presented in Table A.1 while the coefficients for the Sanjeevi lift and torque functions are given in Table A.2.

Lift		**Torque**	
Coefficient	Value	Coefficient	Value
b_1^Z	1.884	c_1^Z	-2.283
b_2^Z	0.1324	c_2^Z	-0.01145
b_3^Z	0.001668	c_3^Z	4.09
b_4^Z	-0.8159	c_4^Z	-0.01395
b_5^Z	0.8562	c_5^Z	0.3406
b_6^Z	0.003624	c_6^Z	0.3609
b_7^Z	0.6598	c_7^Z	0.1355
b_8^Z	-0.2621	c_8^Z	0.2356
b_9^Z	0.8021	c_9^Z	0.3612
b_{10}^Z	0.04384	c_{10}^Z	0.1358

Table A.1: Coefficients for the lift and torque correlations of Zastawny *et al.* [2] fitted for spherocylinder particles with aspect ratio of 4 using in-house DNS simulations.

Lift		**Torque**	
Coefficient	Value	Coefficient	Value
b_1^S	6.718	c_1^S	5.079
b_2^S	0.069	c_2^S	0.342
b_3^S	-0.378	c_3^S	0.197
b_4^S	2.666	c_4^S	-0.161
b_5^S	0.314	c_5^S	0
b_6^S	0.046	c_6^S	0
b_7^S	0.345	c_7^S	0
b_8^S	3.50×10^{-6}	c_8^S	0
b_9^S	1.194		

Table A.2: Coefficients for the lift and torque correlations of Sanjeevi *et al.* [3] for a spherocylinder particle with aspect ratio of 4.

B

SLUGGING OF SPHERICAL PARTICLES - AUDIO SIGNAL ANALYSIS

Supplementary material to Chapter 4

B.1. AUDIO SIGNAL ANALYSIS

B.1.1. INTRODUCTION AND METHOD EXPLANATION

During fluidization, the movement of solid particles causes acoustic emissions due to particle friction, collision and fluid turbulence [140–142]. Fluidized beds operating in different regimes will cause different kinds of acoustic emissions. This property can be used to categorize and analyze fluidization behavior. For large Geldart D particles that were used in this investigation, slugs can be easily distinguished by the sound emitted by a large number of particles falling down in the bed after slug breakage.

We used a simple web camera to film the fluidized bed while operating at the same gas excess velocities as for the X-ray measurements. Measurements were done for 5 minutes and the audio signal was extracted from the webcam video. An example audio file can be found here: AR1-2059lmin.wav. The process of identifying slugs from the audio signal is shown in Fig. B.1. In the original audio signal (Fig. B.1 (a)), slugs can already be noticed easily as high peaks in the time-dependent signal intensity (Fig. B.1 (b)). Each peak starts with a gradual increase in signal intensity due to frictional motion of particles with respect to the column walls, occurring when the slug is going up. The peak in signal intensity ends a with sharp decline as particles fall down after the slug breaks. A smoothing filter (moving average over 0.02 seconds) is applied to the intensity signal to get rid of high-frequency noise and define slugs more clearly (Fig. B.1 (c)). Finally, on the filtered signal a threshold is applied to single out slugs, in a similar way as was done for

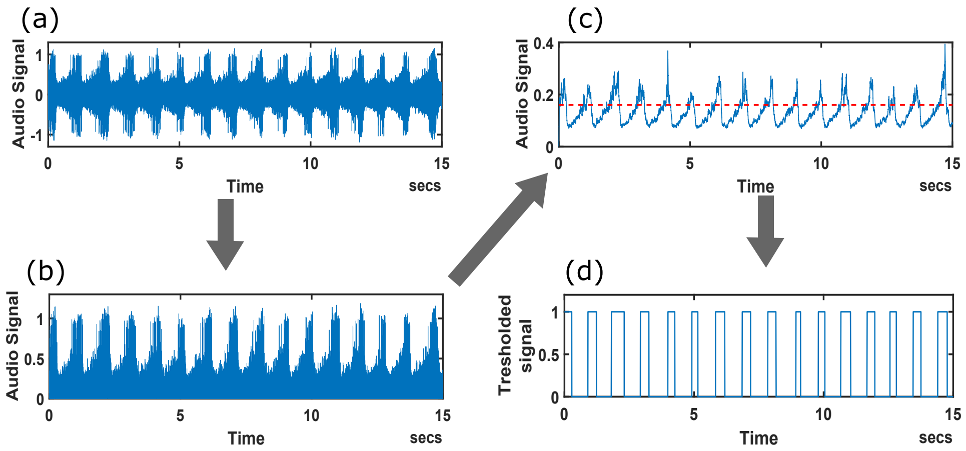

Figure B.1: Example of analyzing audio signal for AR-1 particles at $U - U_{mf} = 0.65$; (a) Original audio signal, (b) Intensity of original signal, (c) Intensity after applying low pass filter, (d) Filtered signal after applying threshold.

the waiting time and frequency analysis in the X-ray investigation described in Chapter 4. However, unlike for the data obtained with X-ray measurements, the choice of the threshold value can not be constant for all gas excess velocities because intensity of the audio signal rises with increase in gas velocity.

B.1.2. Results

The waiting time distribution is calculated from the distance between the centers of consecutive peaks in the thresholded audio signal (Fig. B.1 (c) and (d)). Figure B.2 shows the waiting time distributions for AR-1 particles for different gas excess velocities. It is interesting to note that the waiting time distributions obtained from the audio signal show good agreement with the distributions obtained from the X-ray measurements. The main peak appears at a value of around 1 s and at low gas excess velocities the main peak is followed by smaller peaks at 2, 3 and 4 s. Increasing the gas excess velocity leads to widening of the main peak and the longer waiting time peaks disappear.

We note that analysis of the audio signal was only possible for AR-1 particles. In the case of AR-4 particle fluidization, the back ground noise was too high and it was not possible to discern individual slugs. This can be interpreted as another difference in fluidization behavior between AR-1 and AR-4 particles. During fluidization of AR-4 particles, more individual particles are lifted, and they are lifted higher in the column. These particles hit the column walls more frequently than in the case of AR-1 particles. Together with the more turbulent fluidization discussed in Chapter 4, this generates additional noise that makes detection of slugs in the audio signal very difficult for AR-4 particles.

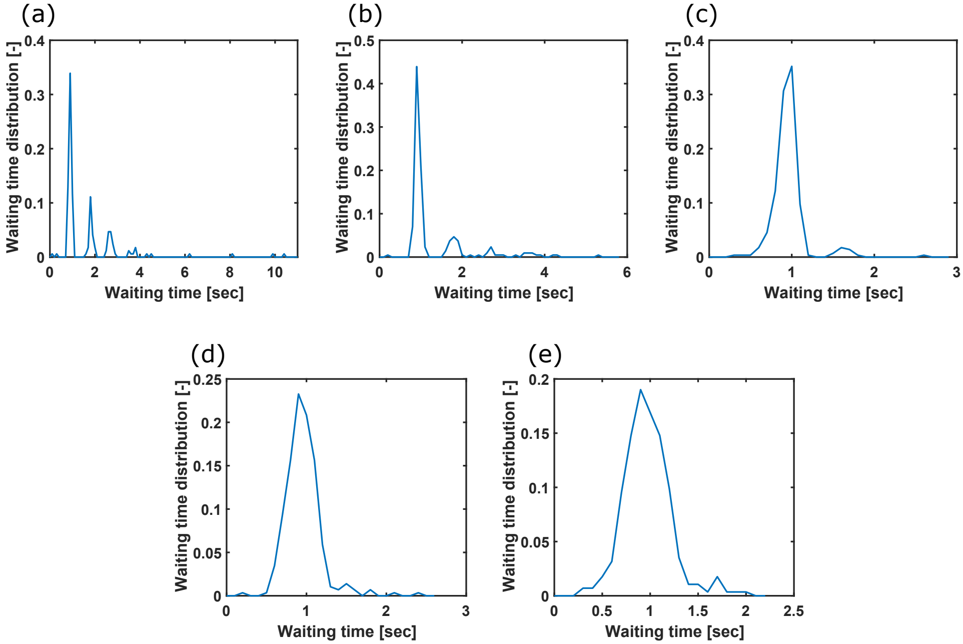

Figure B.2: Waiting time distributions for AR-1 particles at excess gas velocities $U - U_{mf}$ of: (a) 0.4, (b) 0.65, (c) 0.9, (d) 1.15 and (e) 1.4 m/s.

B.1.3. CONCLUSION

We showed that it is possible to obtain rudimentary information on the fluidization characteristic with just an ordinary web camera and that the quality of the obtained slug waiting time distributions is comparable with the ones obtained with the much more expensive and demanding X-ray setup. Even though we were not able to identify slugs from the audio signal in the case of AR-4 particles, we still leave it as an open option with more advanced microphone equipment.

REFERENCES

[1] A. Stukowski, *Visualization and analysis of atomistic simulation data with OVITO, the Open Visualization Tool,* Modelling and Simulation in Materials Science and Engineering **18**, 015012 (2010).

[2] M. Zastawny, G. Mallouppas, F. Zhao, and B. van Wachem, *Derivation of drag and lift force and torque coefficients for non-spherical particles in flows,* International Journal of Multiphase Flow **39**, 227 (2012).

[3] S. K. P. Sanjeevi, J. A. M. Kuipers, and J. T. Padding, *Drag, lift and torque correlations for non-spherical particles from stokes limit to high reynolds numbers,* Journal of Fluid Mechanics (2018).

[4] C. E. Agu, C. Pfeifer, M. Eikeland, L.-A. Tokheim, and B. M. E. Moldestad, *Models for predicting average bubble diameter and volumetric bubble flux in deep fluidized beds,* Industrial & Engineering Chemistry Research **57**, 2658 (2018).

[5] S. K. P. Sanjeevi and J. T. Padding, *Hydrodynamic forces on monodisperse assemblies of axisymmetric elongated particles: Orientation and voidage effects,* AIChE Journal **66** (2020), 10.1002/aic.16951.

[6] O. L. D. Kunii, *Fluidization Engineering* (Elsevier Science, 2013).

[7] V. V. Mahajan, T. M. J. Nijssen, J. A. M. Kuipers, and J. T. Padding, *Non-spherical particles in a pseudo-2d fluidised bed: Modelling study,* Chemical Engineering Science **192**, 1105 (2018).

[8] I. Mema, V. V. Mahajan, B. W. Fitzgerald, and J. T. Padding, *Effect of lift force and hydrodynamic torque on fluidisation of non-spherical particles,* Chemical Engineering Science **195**, 642 (2019).

[9] J. Werther, *Fluidized-bed reactors,* in *Ullmann's Encyclopedia of Industrial Chemistry* (Wiley-VCH Verlag, 2000) pp. 320–366.

[10] R. Warnecke, *Gasification of biomass: comparison of fixed bed and fluidized bed gasifier,* Biomass and Bioenergy **18**, 489 (2000).

[11] J. R. Grace, A. Avidan, and T. Knowlton, *Circulating Fluidized Beds* (Hoerner Fluid Dynamics, 1997).

[12] S. R. Son and S. D. Kim, *Chemical-looping combustion with nio and* fe_2o_3 *in a thermobalance and circulating fluidized bed reactor with double loops,* Industrial & Engineering Chemistry Research **45**, 2689 (2006).

[13] T. Mattisson, M. Keller, C. Linderholm, P. Moldenhauer, M. Rydén, H. Leion, and A. Lyngfelt, *Chemical-looping technologies using circulating fluidized bed systems: Status of development,* Fuel Processing Technology **172**, 1 (2018).

[14] P. T. Williams and E. A. Williams, *Fluidised bed pyrolysis of low density polyethylene to produce petrochemical feedstock,* Journal of Analytical and Applied Pyrolysis **51**, 107 (1999).

[15] Y. Xue, A. Kelkar, and X. Bai, *Catalytic co-pyrolysis of biomass and polyethylene in a tandem micropyrolyzer,* Fuel **166**, 227 (2016).

[16] M. B. Nikoo and N. Mahinpey, *Simulation of biomass gasification in fluidized bed reactor using ASPEN PLUS,* Biomass and Bioenergy **32**, 1245 (2008).

[17] G. Chen, J. Liu, J. Yao, Y. Qi, and B. Yan, *Biodiesel production from waste cooking oil in a magnetically fluidized bed reactor using whole-cell biocatalysts,* Energy Conversion and Management **138**, 556 (2017).

[18] P. McKendry, *Energy production from biomass (part 3): gasification technologies,* Bioresource Technology **83**, 55 (2002).

[19] A. Bridgwater, *Renewable fuels and chemicals by thermal processing of biomass,* Chemical Engineering Journal **91**, 87 (2003).

[20] T. Bridgwater, *Biomass for energy,* Journal of the Science of Food and Agriculture **86**, 1755 (2006).

[21] Z. A. B. Z. Alauddin, P. Lahijani, M. Mohammadi, and A. R. Mohamed, *Gasification of lignocellulosic biomass in fluidized beds for renewable energy development: A review,* Renewable and Sustainable Energy Reviews **14**, 2852 (2010).

[22] W. Cai, R. Liu, Y. He, M. Chai, and J. Cai, *Bio-oil production from fast pyrolysis of rice husk in a commercial-scale plant with a downdraft circulating fluidized bed reactor,* Fuel Processing Technology **171**, 308 (2018).

[23] K. Woytiuk, W. Campbell, R. Gerspacher, R. Evitts, and A. Phoenix, *The effect of torrefaction on syngas quality metrics from fluidized bed gasification of src willow,* Renewable Energy **101**, 409 (2017).

[24] H. Kruggel-Emden and K. Vollmari, *Flow-regime transitions in fluidized beds of non-spherical particles,* Particuology **29**, 1 (2016).

[25] M. Gil, E. Teruel, and I. Arauzo, *Analysis of standard sieving method for milled biomass through image processing. effects of particle shape and size for poplar and corn stover,* Fuel **116**, 328 (2014).

[26] Mahajan, Vinay V., Nijssen, Tim M.J., Fitzgerald, Barry W., Hofman, Jeroen, Kuipers, Hans, and Padding, Johan T., *Fluidization of spherocylindrical particles,* EPJ Web Conf. **140**, 06019 (2017).

[27] N. Vorobiev, A. Becker, H. Kruggel-Emden, A. Panahi, Y. A. Levendis, and M. Schiemann, *Particle shape and stefan flow effects on the burning rate of torrefied biomass,* Fuel **210**, 107 (2017).

[28] S. Tran-Cong, M. Gay, and E. E. Michaelides, *Drag coefficients of irregularly shaped particles,* Powder Technology **139**, 21 (2004).

[29] E. Loth, *Drag of non-spherical solid particles of regular and irregular shape,* Powder Technology **182**, 342 (2008).

[30] A. Hölzer and M. Sommerfeld, *New simple correlation formula for the drag coefficient of non-spherical particles,* Powder Technology **184**, 361 (2008).

[31] A. Hölzer and M. Sommerfeld, *Lattice boltzmann simulations to determine drag, lift and torque acting on non-spherical particles,* Computers and Fluids **38**, 572 (2009).

[32] S. K. P. Sanjeevi and J. T. Padding, *On the orientational dependence of drag experienced by spheroids,* Journal of Fluid Mechanics **820** (2017).

[33] A. Richter and P. A. Nikrityuk, *New correlations for heat and fluid flow past ellipsoidal and cubic particles at different angles of attack,* Powder Technology **249**, 463 (2013).

[34] R. Ouchene, M. Khalij, A. TaniÈre, and B. Arcen, *Drag, lift and torque coefficients for ellipsoidal particles: From low to moderate particle reynolds numbers,* Computers and Fluids **113**, 53 (2015).

[35] R. Ouchene, M. Khalij, B. Arcen, and A. TaniÈre, *A new set of correlations of drag, lift and torque coefficients for non-spherical particles and large reynolds numbers,* Powder Technology **303**, 33 (2016).

[36] M. Mandø and L. Rosendahl, *On the motion of non-spherical particles at high reynolds number,* Powder Technology **202**, 1 (2010).

[37] Y. Tsuji, T. Kawaguchi, and T. Tanaka, *Discrete particle simulation of two-dimensional fluidized bed,* Powder Technology **77**, 79 (1993).

[38] H. Zhu, Z. Zhou, R. Yang, and A. Yu, *Discrete particle simulation of particulate systems: Theoretical developments,* Chemical Engineering Science **62**, 3378 (2007).

[39] N. Deen, M. V. S. Annaland, M. V. der Hoef, and J. Kuipers, *Review of discrete particle modeling of fluidized beds,* Chem. Eng. Sci. **62**, 28 (2007).

[40] H. Zhu, Z. Zhou, R. Yang, and A. Yu, *Discrete particle simulation of particulate systems: A review of major applications and findings,* Chemical Engineering Science **63**, 5728 (2008).

[41] J. Zhao and T. Shan, *Coupled CFD-DEM simulation of fluid-particle interaction in geomechanics,* Powder Technology **239**, 248 (2013).

[42] V. Salikov, S. Antonyuk, S. Heinrich, V. S. Sutkar, N. G. Deen, and J. Kuipers, *Characterization and CFD-DEM modelling of a prismatic spouted bed,* Powder Technology **270, Part B**, 622 (2015).

[43] C. Kloss, C. Goniva, A. Hager, S. Amberger, and S. Pirker, *Models, algorithms and validation for Open Source DEM and CFD-DEM,* Progress in Computational Fluid Dynamics **12**, 140 (2012).

[44] P. Cundall and O. Strack, *A discrete numerical model for granular assemblies,* Geotechnique **21**, 47 (1979).

[45] E. Aharonov and D. Sparks, *Rigidity phase transition in granular packings,* Phys. Rev. E **60**, 6890 (1999).

[46] E. Aharonov and D. Sparks, *Shear profiles and localization in simulations of granular materials,* Phys. Rev. E **65**, 051302 (2002).

[47] B. W. Fitzgerald, I. Clancy, and D. Corcoran, *Bridging percolation and particle dynamics models of the granular rigidity transition,* Physica A: Statistical Mechanics and its Applications **410**, 582 (2014).

[48] C. Vega and S. Lago, *A fast algorithm to evaluate the shortest distance between rods,* Computers and Chemistry **18**, 55 (1994).

[49] L. Pournin, M. Weber, M. Tsukahara, J.-A. Ferrez, M. Ramaioli, and T. M. Liebling, *Three-dimensional distinct element simulation of spherocylinder crystallization,* Granular Matter **7**, 119 (2005).

[50] E. Azéma and F. Radjaï, *Force chains and contact network topology in sheared packings of elongated particles,* Phys. Rev. E **85**, 031303 (2012).

[51] T. Marschall and S. Teitel, *Compression-driven jamming of athermal frictionless spherocylinders in two dimensions,* Phys. Rev. E **97**, 012905 (2018).

[52] R. Kumar, A. Sarkar, W. Ketterhagen, B. Hancock, J. Curtis, and C. Wassgren, *Influence of normal contact force model on simulations of spherocylindrical particles,* AIChE Journal **64**, 1986 (2018).

[53] M. Haustein, A. Gladkyy, and R. Schwarze, *Discrete element modeling of deformable particles in yade,* SoftwareX **6**, 118 (2017).

[54] B. Xu and A. Yu, *Numerical simulation of the gas-solid flow in a fluidized bed by combining discrete particle method with computational fluid dynamics,* Chemical Engineering Science **52**, 2785 (1997).

[55] L. Rosendahl, *Using a multi-parameter particle shape description to predict the motion of non-spherical particle shapes in swirling flow,* Appl. Math. Modelling **24**, 11 (2000).

[56] A. Haider and O. Levenspiel, *Drag coefficient and terminal velocity of spherical and nonspherical particles,* Powder Technology **58**, 63 (1989).

[57] G. H. Ganser, *A rational approach to drag prediction of spherical and nonspherical particles,* Powder Technology **77**, 143 (1993).

[58] R. D. Felice, *The voidage function for fluid-particle interaction systems,* International Journal of Multiphase Flow **20**, 153 (1994).

[59] L. Rong, K. Dong, and A. Yu, *Lattice-boltzmann simulation of fluid flow through packed beds of uniform spheres: Effect of porosity,* Chemical Engineering Science **99**, 44 (2013).

[60] I. Mema, V. V. Mahajan, B. W. Fitzgerald, H. Kuipers, and J. T. Padding, *Effect of lift force on dense gas-fluidized beds of non-spherical particles,* in *Proceedings of 12th International Conference on CFD in Oil and Gas, Metallurgical and Process Industries* (2017).

[61] Z. Peng, E. Doroodchi, C. Luo, and B. Moghtaderi, *Influence of void fraction calculation on fidelity of CFD-DEM simulation of gas-solid bubbling fluidized beds,* AIChE Journal **60**, 2000 (2014).

[62] J. Hilton, L. Mason, and P. Cleary, *Dynamics of gas-solid fluidised beds with non-spherical particle geometry,* Chemical Engineering Science **65**, 1584 (2010).

[63] K. Vollmari, R. Jasevičius, and H. Kruggel-Emden, *Experimental and numerical study of fluidization and pressure drop of spherical and non-spherical particles in a model scale fluidized bed,* Powder Technology **291**, 506 (2016).

[64] J. Gan, Z. Zhou, and A. Yu, *Particle scale study of heat transfer in packed and fluidized beds of ellipsoidal particles,* Chemical Engineering Science **144**, 201 (2016).

[65] H. Ma and Y. Zhao, *Cfd-dem investigation of the fluidization of binary mixtures containing rod-like particles and spherical particles in a fluidized bed,* Powder Technology , (2018).

[66] H. Ma and Y. Zhao, *Investigating the fluidization of disk-like particles in a fluidized bed using cfd-dem simulation,* Advanced Powder Technology (2018), https://doi.org/10.1016/j.apt.2018.06.017.

[67] K. A. Buist, A. C. van der Gaag, N. G. Deen, and J. A. M. Kuipers, *Improved magnetic particle tracking technique in dense gas fluidized beds,* AIChE J. **60**, 3133 (2014).

[68] K. A. Buist, P. Jayaprakash, J. Kuipers, N. G. Deen, and J. T. Padding, *Magnetic particle tracking for nonspherical particles in a cylindrical fluidized bed,* AIChE Journal **63**, 5335 (2017).

[69] A. Köhler, A. Rasch, D. Pallarès, and F. Johnsson, *Experimental characterization of axial fuel mixing in fluidized beds by magnetic particle tracking,* Powder Technology **316**, 492 (2017).

[70] I. Mema, K. A. Buist, J. Kuipers, and J. T. Padding, *Fluidization of spherical versus elongated particles - experimental investigation using magnetic particle tracking,* AIChE Journal (2019), 10.1002/aic.16895.

[71] L. Seelen, J. T. Padding, and J. A. M. Kuipers, *A granular discrete element method for arbitrary convex particle shapes: Method and packing generation,* Chemical Engineering Science **189**, 84 (2018).

[72] T. Oschmann, K. Vollmari, H. Kruggel-Emden, and S. Wirtz, *Numerical investigation of the mixing of non-spherical particles in fluidized beds and during pneumatic conveying,* Procedia Engineering **102**, 976 (2015).

[73] J. Cai, Q. Li, and Z. Yuan, *Orientation of cylindrical particles in gas–solid circulating fluidized bed,* Particuology **10**, 89 (2012).

[74] A. Zarghami and J. T. Padding, *Drag, lift and torque acting on a two-dimensional non-spherical particle near a wall,* Advanced Powder Technology **29**, 1507 (2018).

[75] J. F. de Jong, S. O. Odu, M. S. van Buijtenen, N. G. Deen, M. van Sint Annaland, and J. A. M. Kuipers, *Development and validation of a novel digital image analysis method for fluidized bed particle image velocimetry,* Powder Technology **230**, 193 (2012).

[76] L. Boer, K. A. Buist, N. G. Deen, J. T. Padding, and J. A. M. Kuipers, *Experimental study on orientation and de-mixing phenomena of elongated particles in gas-fluidized beds,* Powder Technology **329**, 332 (2018).

[77] T. Grassler and K. E. Wirth, *X-ray computer tomography — potential and limitation for the measurement of local solids distribution in circulating fluidized beds,* Chemical Engineering Journal **77**, 65 (2000).

[78] R. F. Mudde, *Time-resolved x-ray tomography of a fluidized bed,* Powder Technology **199**, 55 (2010).

[79] X. Yang, J. R. van Ommen, J. Schoormans, and R. F. Mudde, *A hybrid tomographic reconstruction algorithm for high speed x-ray tomography,* Computer Physics Communications **196**, 27 (2015).

[80] V. Verma, J. T. Padding, N. G. Deen, J. A. M. Kuipers, F. Barthel, M. Bieberle, M. Wagner, and U. Hampel, *Bubble dynamics in a 3-d gas-solid fluidized bed using ultrafast electron beam x-ray tomography and two-fluid model,* AIChE Journal **60**, 1632 (2014).

[81] X. Chen, W. Zhong, and T. J. Heindel, *Using stereo XPTV to determine cylindrical particle distribution and velocity in a binary fluidized bed,* AIChE Journal (2018), 10.1002/aic.16485.

[82] X. Chen, W. Zhong, and T. J. Heindel, *Orientation of cylindrical particles in a fluidized bed based on stereo x-ray particle tracking velocimetry (XPTV),* Chemical Engineering Science **203**, 104 (2019).

[83] F. Guillard, B. Marks, and I. Einav, *Dynamic x-ray radiography reveals particle size and shape orientation fields during granular flow,* Scientific Reports **7** (2017), 10.1038/s41598-017-08573-y.

[84] J. Baker, F. Guillard, B. Marks, and I. Einav, *X-ray rheography uncovers planar granular flows despite non-planar walls,* Nature Communications **9** (2018), 10.1038/s41467-018-07628-6.

[85] D. J. Parker, T. W. Leadbeater, X. Fan, M. N. Hausard, A. Ingram, and Z. Yang, *Positron imaging techniques for process engineering: recent developments at birmingham,* Measurement Science and Technology **19**, 094004 (2008).

[86] J. M. Link, N. G. Deen, J. A. M. Kuipers, X. Fan, A. Ingram, D. J. Parker, J. Wood, and J. P. K. Seville, *PEPT and discrete particle simulation study of spout-fluid bed regimes,* AIChE Journal **54**, 1189 (2008).

[87] Z. Yang, X. Fan, S. Bakalis, D. J. Parker, and P. J. Fryer, *A method for characterising solids translational and rotational motions using multiple-positron emission particle tracking (multiple-PEPT),* International Journal of Multiphase Flow **34**, 1152 (2008).

[88] L. Yang, J. T. Padding, K. A. Buist, and J. A. M. Kuipers, *Three-dimensional fluidized beds with rough spheres: Validation of a two fluid model by magnetic particle tracking and discrete particle simulations,* Chemical Engineering Science **174**, 238 (2017).

[89] H. Richert, O. Kosch, and P. Grnert, *Magnetic monitoring as a diagnostic method for investigating motility in the human digestive system,* in *Magnetism in Medicine* (Wiley-VCH Verlag GmbH & Co. KGaA) pp. 481–498.

[90] G. Mohs, O. Gryczka, S. Heinrich, and L. Mörl, *Magnetic monitoring of a single particle in a prismatic spouted bed,* Chemical Engineering Science **64**, 4811 (2009).

[91] X. Tao, X. Tu, and H. Wu, *A new development in magnetic particle tracking technology and its application in a sheared dense granular flow,* Review of Scientific Instruments **90**, 065116 (2019).

[92] K. A. Buist, T. W. van Erdewijk, N. G. Deen, and J. A. M. Kuipers, *Determination and comparison of rotational velocity in a pseudo 2-d fluidized bed using magnetic particle tracking and discrete particle modeling,* AIChE Journal **61**, 3198 (2015).

[93] J. A. Laverman, X. Fan, A. Ingram, M. van Sint Annaland, D. J. Parker, J. P. K. Seville, and J. A. M. Kuipers, *Experimental study on the influence of bed material on the scaling of solids circulation patterns in 3d bubbling gas–solid fluidized beds of glass and polyethylene using positron emission particle tracking,* Powder Technology **224**, 297 (2012).

[94] I. Mema, E. C. Wagner, J. R. van Ommen, and J. T. Padding, *Fluidization of spherical versus elongated particles - experimental investigation using x-ray tomography,* Chemical Engineering Journal , 125203 (2020).

[95] V. V. Mahajan, J. T. Padding, T. M. J. Nijssen, K. A. Buist, and J. A. M. Kuipers, *Non-spherical particles in a pseudo-2d fluidized bed: Experimental study,* AIChE Journal **64**, 1573 (2018).

[96] M. Stein, Y. Ding, J. Seville, and D. Parker, *Solids motion in bubbling gas fluidised beds,* Chemical Engineering Science **55**, 5291 (2000).

[97] X. Fan, D. J. Parker, Z. Yang, J. P. Seville, and J. Baeyens, *The effect of bed materials on the solid/bubble motion in a fluidised bed,* Chemical Engineering Science **63**, 943 (2008).

[98] Y. Makkawi and P. Wright, *Fluidization regimes in a conventional fluidized bed characterized by means of electrical capacitance tomography,* Chemical Engineering Science **57**, 2411 (2002).

[99] C. Rautenbach, R. Mudde, X. Yang, M. Melaaen, and B. Halvorsen, *A comparative study between electrical capacitance tomography and time-resolved x-ray tomography,* Flow Measurement and Instrumentation **30**, 34 (2013).

[100] M. Zhang and M. Soleimani, *Simultaneous reconstruction of permittivity and conductivity using multi-frequency admittance measurement in electrical capacitance tomography,* Measurement Science and Technology **27**, 025405 (2016).

[101] T. Kai, M. Misawa, T. Takahashi, I. Tiseanu, N. Ichikawa, and N. Takada, *Application of fast x-ray CT scanner to visualization of bubbles in fluidized bed.* JOURNAL OF CHEMICAL ENGINEERING OF JAPAN **33**, 906 (2000).

[102] O. L. D. Kunii, *Fluidization Engineering* (Elsevier Science, 2013).

[103] J. Baeyens and D. Geldart, *An investigation into slugging fluidized beds,* Chemical Engineering Science **29**, 255 (1974).

[104] W. J. Thiel and O. E. Potter, *Slugging in fluidized beds,* Industrial & Engineering Chemistry Fundamentals **16**, 242 (1977).

[105] S. Satija and L.-S. Fan, *Characteristics of slugging regime and transition to turbulent regime for fluidized beds of large coarse particles,* AIChE Journal **31**, 1554 (1985).

[106] R. D. Felice, S. Rapagnà, and P. Foscolo, *Dynamic similarity rules: Validity check for bubbling and slugging fluidized beds,* Powder Technology **71**, 281 (1992).

[107] W. Kong, T. Tan, J. Baeyens, G. Flamant, and H. Zhang, *Bubbling and slugging of geldart group a powders in small diameter columns,* Industrial & Engineering Chemistry Research **56**, 4136 (2017).

[108] W. Kong, J. Baeyens, G. Flamant, T. Tan, and H. Zhang, *Solids flow in a "particle-in-tube" concentrated solar heat absorber,* Industrial & Engineering Chemistry Research **58**, 4598 (2018).

[109] F. Sabatier, R. Ansart, H. Zhang, J. Baeyens, and O. Simonin, *Experiments support simulations by the NEPTUNE_CFD code in an upflow bubbling fluidized bed reactor,* Chemical Engineering Journal **385**, 123568 (2020).

[110] C. E. Agu, L.-A. Tokheim, M. Eikeland, and B. M. Moldestad, *Improved models for predicting bubble velocity, bubble frequency and bed expansion in a bubbling fluidized bed,* Chemical Engineering Research and Design **141**, 361 (2019).

[111] C. M. Venier, A. R. Urrutia, J. P. Capossio, J. Baeyens, and G. Mazza, *Comparing ANSYS fluent® and OpenFOAM® simulations of geldart a, b and d bubbling fluidized bed hydrodynamics,* International Journal of Numerical Methods for Heat & Fluid Flow **30**, 93 (2019).

[112] S. Maurer, D. Gschwend, E. C. Wagner, T. J. Schildhauer, J. R. van Ommen, S. M. Biollaz, and R. F. Mudde, *Correlating bubble size and velocity distribution in bubbling fluidized bed based on x-ray tomography,* Chemical Engineering Journal **298**, 17 (2016).

[113] J. Ma, J. R. van Ommen, D. Liu, R. F. Mudde, X. Chen, E. C. Wagner, and C. Liang, *Fluidization dynamics of cohesive geldart b particles. part i: X-ray tomography analysis,* Chemical Engineering Journal **359**, 1024 (2019).

[114] S. Jahangir, E. C. Wagner, R. F. Mudde, and C. Poelma, *Void fraction measurements in partial cavitation regimes by x-ray computed tomography,* International Journal of Multiphase Flow **120**, 103085 (2019).

[115] S. Maurer, E. C. Wagner, J. R. van Ommen, T. J. Schildhauer, S. L. Teske, S. M. Biollaz, A. Wokaun, and R. F. Mudde, *Influence of vertical internals on a bubbling fluidized bed characterized by x-ray tomography,* International Journal of Multiphase Flow **75**, 237 (2015).

[116] B. Du, L.-S. Fan, F. Wei, and W. Warsito, *Gas and solids mixing in a turbulent fluidized bed,* AIChE Journal **48**, 1896 (2002).

[117] N. Ellis, L. Briens, J. Grace, H. Bi, and C. Lim, *Characterization of dynamic behaviour in gas–solid turbulent fluidized bed using chaos and wavelet analyses,* Chemical Engineering Journal **96**, 105 (2003).

[118] I. Mema and J. Padding, *Fluidization of elongated particles - effect of multi-particle correlations for drag, lift and torque in CFD-DEM,* (2020), 10.22541/au.159234121.14221968.

[119] W. R. Goossens, *Review of the empirical correlations for the drag coefficient of rigid spheres,* Powder Technology **352**, 350 (2019).

[120] A. Hölzer and M. Sommerfeld, *New simple correlation formula for the drag coefficient of non-spherical particles,* Powder Technology **184**, 361 (2008).

[121] S. Tenneti, R. Garg, and S. Subramaniam, *Drag law for monodisperse gas–solid systems using particle-resolved direct numerical simulation of flow past fixed assemblies of spheres,* International Journal of Multiphase Flow **37**, 1072 (2011).

[122] Y. Y. Tang, E. A. J. F. F. Peters, J. A. M. H. Kuipers, S. H. L. S. Kriebitzsch, and M. A. M. van der Hoef, *A new drag correlation from fully resolved simulations of flow past monodisperse static arrays of spheres,* AIChE Journal **61**, 688 (2014).

[123] X. Li, M. Jiang, Z. Huang, and Q. Zhou, *Effect of particle orientation on the drag force in random arrays of prolate ellipsoids in low-reynolds-number flows,* AIChE Journal **65** (2019), 10.1002/aic.16621.

[124] L. He and D. Tafti, *Variation of drag, lift and torque in a suspension of ellipsoidal particles,* Powder Technology **335**, 409 (2018).

[125] T. Oschmann, J. Hold, and H. Kruggel-Emden, *Numerical investigation of mixing and orientation of non-spherical particles in a model type fluidized bed,* Powder Technology **258**, 304 (2014).

[126] S. Shrestha, S. Kuang, A. Yu, and Z. Zhou, *Orientation of spheroidal particles in single jet bubbling fluidized beds,* Powder Technology **361**, 363 (2020).

[127] I. Mema and J. T. Padding, *Spherical versus elongated particles – numerical investigation of mixing characteristics in a gas fluidized bed,* Chemical Engineering Science: X **8**, 100079 (2020).

[128] P. Rowe and A. Nienow, *Particle mixing and segregation in gas fluidised beds. a review,* Powder Technology **15**, 141 (1976).

[129] W. J. Thiel and O. E. Potter, *The mixing of solids in slugging gas fluidized beds,* AIChE Journal **24**, 561 (1978).

[130] Y. F. Shi and L. T. Fan, *Lateral mixing of solids in batch gas-solids fluidized beds,* Industrial & Engineering Chemistry Process Design and Development **23**, 337 (1984).

[131] J. Peeler and J. Huang, *Segregation of wide size range particle mixtures in fluidized beds,* Chemical Engineering Science **44**, 1113 (1989).

[132] L. Shen, M. Zhang, and Y. Xu, *Solids mixing in fluidized beds,* Powder Technology **84**, 207 (1995).

[133] M. Rhodes, X. Wang, M. Nguyen, P. Stewart, and K. Liffman, *Study of mixing in gas-fluidized beds using a DEM model,* Chemical Engineering Science **56**, 2859 (2001).

[134] N. G. Deen, G. Willem, G. Sander, and J. A. M. Kuipers, *Numerical analysis of solids mixing in pressurized fluidized beds,* Industrial & Engineering Chemistry Research **49**, 5246 (2010).

[135] M. Banaei, N. Deen, M. van Sint Annaland, and J. Kuipers, *Particle mixing rates using the two-fluid model,* Particuology **36**, 13 (2018).

[136] G. Lu, J. Third, and C. Müller, *Discrete element models for non-spherical particle systems: From theoretical developments to applications,* Chemical Engineering Science **127**, 425 (2015).

[137] W. Zhong, A. Yu, X. Liu, Z. Tong, and H. Zhang, *DEM/CFD-DEM modelling of non-spherical particulate systems: Theoretical developments and applications,* Powder Technology **302**, 108 (2016).

[138] O. Oke, B. van Wachem, and L. Mazzei, *Lateral solid mixing in gas-fluidized beds: CFD and DEM studies,* Chemical Engineering Research and Design **114**, 148 (2016).

[139] Y. Wen, M. Liu, B. Liu, and Y. Shao, *Comparative study on the characterization method of particle mixing index using DEM method,* Procedia Engineering **102**, 1630 (2015).

[140] N. Salehi-Nik, R. Sotudeh-Gharebagh, N. Mostoufi, R. Zarghami, and M. Mahjoob, *Determination of hydrodynamic behavior of gas–solid fluidized beds using statistical analysis of acoustic emissions,* International Journal of Multiphase Flow **35**, 1011 (2009).

[141] H. Tsujimoto, T. Yokoyama, C. Huang, and I. Sekiguchi, *Monitoring particle fluidization in a fluidized bed granulator with an acoustic emission sensor,* Powder Technology **113**, 88 (2000).

[142] J. Wang, C. Ren, Y. Yang, and L. Hou, *Characterization of particle fluidization pattern in a gas solid fluidized bed based on acoustic emission (AE) measurement,* Industrial & Engineering Chemistry Research **48**, 8508 (2009).

ACKNOWLEDGEMENTS

CURRICULUM VITÆ

Ivan Mema was born on November 8th, 1989 in Vršac, Serbia. He obtained BSc (2012) and MSc (2013) degrees in the field of chemical engineering at the Faculty of Technology and Metallurgy at Belgrade University. For excellent success during his studies and graduation he was awarded faculty prizes in 2011 and 2012. During his internship in 2012 at Universidade Estadual de Campinas (Unicamp) in Campinas, Brazil, he worked on a study of heterogeneous catalytic reactions.

After completing his studies, Ivan worked as a process and development engineer in "Prva Iskra" -Namenska a.d. in Belgrade, Serbia, where he worked on the production of high explosives.

In December 2015, Ivan began his doctoral research in the Multiphase Reactor Group, Chemical Engineering and Chemistry Department at Technical University Eindhoven under the guidance of Prof. Hans Kuipers and Prof. Johan Padding on the topic of fluidization of elongated particles. From July 2017, he continued his PhD at the department of Process and Energy, Faculty of Mechanical, Maritime and Materials Engineering, Technical University Delft, under the guidance of Prof. Johan Padding. The results of his research are presented in this dissertation.

LIST OF PUBLICATIONS

JOURNAL PUBLICATIONS

6. **I. Mema** and J. T. Padding, *Fluidization of elongated particles - effect of multi-particle correlations (drag, lift and torque) in CFD-DEM simulations*, AIChE Journal , (2020) (In Production).

5. **I. Mema** and J. T. Padding, *Spherical versus elongated particles - numerical investigation of mixing characteristics in a gas fluidized bed*, Chemical Engineering Science: X **8**, (2020).

4. **I. Mema**, E. C. Wagner, J. R. van Ommen and J. T. Padding, *Fluidization of spherical versus elongated particles - experimental investigation using X-ray tomography*, Chemical Engineering Journal **397**, (2020).

3. **I. Mema**,K. A. Buist, J. A. M. Kuipers and J. T. Padding, *Fluidization of spherical versus elongated particles: Experimental investigation using magnetic particle tracking*, AIChE Journal **66**, (2019).

2. B. W. Fitzgerald, A. Zarghami, V. V. Mahajan, S. K. P. Sanjeevi **I. Mema**, V. Verma, Y. M. F. El Hasadi and J. T. Padding *Multiscale Simulation of Elongated Particles in Fluidised Beds*, Chemical Engineering Science: X **2**, (2019).

1. **I. Mema**, V. V. Mahajan, B. W. Fitzgerald and J. T. Padding, *Effect of lift force and hydrodynamic torque on fluidization of non-spherical particles*, Chemical Engineering Science **195**, 642-656 (2019).

CONFERENCE PROCEEDINGS AND PRESENTATIONS

6. **I. Mema**, E. C. Wagner, J. R. van Ommen and J. T. Padding, *Fluidization behavior of elongated particles - X-ray tomography experiments*, Fluidization XVI, Guilin, China (2019).

5. **I. Mema**,K. A. Buist, J. A. M. Kuipers and J. T. Padding, *Effect Of Lift And Hydrodynamic Torque On Fluidization Of Non-Spherical Particles: Experimental Validation*, Physics@Veldhoven, Veldhoven, The Netherlands (2019).

4. **I. Mema**,K. A. Buist, J. A. M. Kuipers and J. T. Padding, *Effect Of Lift And Hydrodynamic Torque On Fluidization Of Non-Spherical Particles: Experimental Validation*, CFD-CPT, Melbourne, Australia (2018).

3. **I. Mema**, V. V. Mahajan, B. W. Fitzgerald and J. T. Padding, *Effect of lift force and hydrodynamic torque on fluidization of non-spherical particles*, APS march meeting, Los Angeles, USA (2018).

2. **I. Mema**, V. V. Mahajan, B. W. Fitzgerald, J. A. M. Kuipers and J. T. Padding, *Effect of lift force on dense gas-fluidised beds of non-spherical particles*, AERC, Copenhagen, Denmark (2017).

1. **I. Mema**, V. V. Mahajan, B. W. Fitzgerald, J. A. M. Kuipers and J. T. Padding, *Effect of lift force and hydrodynamic torque on fluidization of non-spherical particles*, CFD2017, Trondheim, Norway (2017).